External Discharge Plasma Thruster

KARADAG BURAK

Doctor of Philosophy

Department of Space and Astronautical Science
School of Physical Sciences
SOKENDAI (The Graduate University for Advanced Studies)

External Discharge Plasma Thruster

by

KARADAG Burak

Doctor of Philosophy
March 2018

Department of Space and Astronautical Science
School of Physical Sciences
The Graduate University for Advanced Studies
(SOKENDAI)
Institute of Space and Astronautical Science (ISAS/JAXA)

Advisor:
Assoc. Prof. Dr. Ikkoh FUNAKI, SOKENDAI, ISAS/JAXA
Co-Advisor:
Dr. Shinatora CHO, JAXA

Abstract

Hall thruster is a plasma based propulsion system used for spacecraft attitude and orbit control. Hall thrusters have high thrust density/efficiency, reliable/robust operation, simple design and extensive space flight heritage. These main features make them attractive for small/micro/nano satellite applications. However, it is quite a challenge to design low power Hall thrusters with long lifetime and high efficiency because of large surface area to volume ratio and physical limits to the magnetic circuit miniaturization. As a potential solution to this problem, this dissertation introduces the external discharge plasma thruster (XPT), which produces, and sustains a plasma discharge completely outside of a non-anodic cavity. Thrust, discharge current oscillation, ion beam current, anode temperature and plasma property measurements were conducted to characterize the manufactured prototype thruster for the proof of concept. The thrust performance, propellant ionization and thruster erosion were discussed. Thrust generated by the XPT was on par with conventional Hall thrusters (SPT/TAL) at the same power level (~11 mN at 250W with 25% anode efficiency), and discharge current had SPT-level stability (Δ<0.2). Faraday probe measurements revealed that ion beams are finely collimated, and plumes have Gaussian distributions. Mass utilization efficiencies, beam utilization efficiencies and plume divergence efficiencies ranged from 28 to 62%, 78 to 99 %, and 40 to 48% respectively. Plasma densities and electron temperatures were found to reach $5x10^{18}$ m^{-3} ($\partial n_e/n_e$ = ±52%) and 15 eV ($\partial T_e/T_e$ = ±10-30%) respectively at 10 mm axial distance from the anode centerline. These values explain why our thruster is as efficient as conventional ones even without a physical ionization chamber. Non-uniformity of the radial magnetic field strength in the azimuthal direction coupled with cathode position was found to play an important role in distributing plasma density. Our findings propose an alternative approach for low power Hall thruster design, and provide a successful proof of concept experiment of the XPT.

Acknowledgements

First of all, I would like to express my sincere gratitude to my advisor Prof. Ikkoh Funaki for replying my first email to him and providing me a place at his laboratory and for all his guidance that he has given me over the past six years, and to Embassy of Japan in Turkey for choosing me as one of the recipients of the monbukagakusho scholarship.

I owe special debt of gratitude to my co-advisor Dr. Shinatora Cho for his discussions, suggestions and invaluable comments. My heartfelt appreciation goes to Prof. Oshio Yuya, Prof. Watanabe Hiroki and Prof. Kazuma Ueno for their advice during my research. I owe thanks to Prof. Kimiya Komurasaki and his students Yushi Hamada and Junhwi Bak for their support in doing thrust measurements and for sharing their thruster configuration and experimental results.

I would like to extend my appreciation to Prof. Takumi Abe for letting me use vacuum facilities at ISAS/JAXA. I cannot thank Tomoyuki Nakazono and Yuuya Iwakura enough for their assistance with the vacuum facility till late at night. I am particularly grateful to old boys Fueki-san and Kubota-san for patiently teaching me how to use the workshop machines and tools. I am still amazed by the fact that they can precisely calculate limits, fits and tolerances despite their advancing age.

Special thanks go to David Ju and George Cristian Potrivitu for making the daily laboratory life more enjoyable. They have done incredible work in such short time. I also thank Sunao Hasegawa for borrowing me one of his high speed cameras, Prof. Tobe Hirobumi for taking SEM images of some thruster parts, Mayumi Yamashita and Naoko Fukayama for their help with student affairs.

Finally and most importantly, I am deeply thankful to my family for their enduring support and of course to Allah, the One and Only creator, the most Gracious and the most Merciful. Alhamdulillah!

Table of Contents

List of Figures

List of Tables

Nomenclature

B	magnetic field strength
B_r	radial magnetic field strength
D_A	anode diameter
$D_\perp$	cross-field diffusion coefficient
e	unit charge
EEDF	electron energy distribution function
F	thrust
I_b	beam current
I_{b1}	singly charged ion current
I_{b2}	doubly charged ion current
I_{cap}	capacitive current
I_d	discharge current
$\overline{I_d}$	average discharge current
I_g	magnetic pole current
I_i	ion saturation current
I_n	unionized neutral propellant current
I_p	probe current
I_{spa}	anode specific impulse
$j_z(r)$	axial ion current density
k_B	Boltzmann constant
K_n	Knudsen number
M_{xe}	equivalent mass of elemental xenon
m	electron mass
mg/s	milligram per second
mN	miliNewton
$\dot{m}$	propellant mass flow rate
n_n	neutral density
P_{jet}	energy deposited on propellant
P_d	discharge power
r	radial coordinate
r_p	probe radius
RMS	root mean square
S	probe surface area
XPT	external discharge plasma thruster
SPT	stationary plasma thruster
TAL	thruster with anode layer
T	Tesla
T_{anode}	anode temperature
T_{wall}	inner and outer wall temperature
T_e	electron temperature
V_b	beam voltage
V_c	cathode coupling voltage
V_d	discharge voltage
z	axial coordinate
λ_D	Debye length
λ_{MFR}	Mean free path

Δ	discharge current oscillation amplitude
δ	charged-weighted divergence angle
η_a	anode efficiency
η_t	thrust efficiency
η_E	energy efficiency
η_V	voltage utilization efficiency
ν	electron collision frequency
η_u	propellant utilization efficiency
η_a	beam utilization efficiency
η_b	current utilization efficiency
η_d	plume divergence efficiency
η_m	mass utilization efficiency
η_q	charge utilization efficiency
ω_c	electron cyclotron frequency
θ	azimuthal angle
τ	time

CHAPTER 1

Introduction

Contents

"Professor Oberth has been right with so many of his early proposals. I wouldn't be a bit surprised if one day we flew to Mars electrically!"

Wernher von Braun

1.1 A Short History of Electric Propulsion

Although their widespread use over the past two decades, electric propulsion systems or with its popular name plasma rockets are actually as old as chemical rocket engines. At the end of the 19th century it was found that electrons move thousands of times faster than the average speed of hydrogen gas molecules (30,000-100,000 km/s). Inspired by this development R. H. Goddard (1906) and K. E. Tsiolkovsky (1911) independently raised the same idea that the high-speed electron flow could be used to move a spacecraft. Note that the existence of protons was not confirmed until 1920.

There were technical issues that have to be resolved to form a useful electric propulsion concept. For example, the underlying physics of electron-ion pair production was not clear. Moreover, it was believed that electric propulsion systems would require

enormous amounts of energy, and therefore could not be realized in the near future. Besides, chemical rocket engines had to be developed first to go into space.

H. J. Oberth devoted a whole chapter to electric propulsion in his book titled 'Ways to Spaceflight' in 1929, and praised the benefits it will bring such as fuel savings. Then, electric propulsion became known by many professional and amateur space enthusiasts. At the beginning of the 1930's, V.P. Glushko succeeded in producing and testing the first laboratory prototype of an electric propulsion system under the Soviet Space Program. However, electric propulsion was often shown as scientifically weak but fascinating interplanetary propulsion system in science fiction literature until the end of the Second World War.

Significant work was done towards ion current generation in the 1940s and 50s, and it was shown that ion propulsion is fully applicable. In addition, it was proven that some trajectory maneuvers could be performed more efficiently by using electric propulsion. E. Stuhlinger did the first systematic analysis of electric propulsion systems, which laid the groundwork for the establishment of serious research programs, and increased spending on R&D of electric propulsion systems. In the 1960s, the first electric thrusters were successfully tried in space by the US and the Soviets about half a century after its introduction.

Despite remarkable fuel savings, electric thrusters were considered risky for expensive space missions in the US, and were limited to experimental work until the late 1990s. The Soviets adopted a more open attitude towards this new technology, and employed electric thrusters to control trajectory and attitude of hundreds of satellites from the 1970s to the present day. While the US concentrated on gridded ion engines, the Soviets contributed significantly to the Hall thruster literature until the 1990s. The successful use of electric thrusters in the Soviet Union gave rise to renewed interest in this technology in the US. In 1998 a gridded ion engine was used for the first time as a main propulsion system by NASA in the Deep Space 1 mission. High thrust density/efficiency and reliable/stable operation of Hall thrusters caught the attention of the US and Europe. With the fall of the Soviet Union, intensive research program and technology transfer from Russia was established in the US followed by Japan, Europe and China.

Electric propulsion has been used in many missions to date. For example, there were four gridded ion engines HAYABUSA spacecraft of Japan Space Exploration Agency (JAXA), which won international reputation for collecting and returning samples to Earth from the surface of an asteroid for the first time. Subsequently, the European Space Agency (ESA) sent its first spacecraft, which used a Hall thruster as a primary propulsion system, to the Moon. With the acceptance of reliability and cost benefits, electric propulsion technology is becoming more and more important, and many missions are planned in the future. Details of the electric propulsion history can be found in Ref.1.

1.2 Electric Propulsion Classification

Electric propulsion (EP) is a generic name of methods in which propellant are accelerated by using electric power. EP systems require less propellant mass compared to chemical propulsion (CP) systems by achieving very high exhaust velocities. Velocity change of a spacecraft (ΔV) is formulated by ideal rocket equation as below:

$$\Delta V = V_e \ln\left(\frac{m_i}{m_f}\right) \tag{1.1}$$

where V_e is exhaust velocity (m/s), m_i is initial total mass including propellant, m_f is final total mass without propellant. Then, any increase in exhaust velocity reduces the ratio of final-to-initial mass, which can be interpreted as reduction in propellant mass or increase in payload mass. Exhaust velocity is often characterized by specific impulse (I_{sp}). I_{sp} shows efficiency of propellant acceleration, and it is described as the total impulse per unit weight. The higher I_{sp}, the lower propellant mass flow rate will be required for a given thrust. It is formulated as below:

$$I_{SP} = \frac{\int F dt}{g \int \dot{m} dt} \approx \frac{v_e}{g} \tag{1.2}$$

where F is thrust (N), g is the acceleration due to gravity (m/s2), $\dot{m}$ is propellant mass flow rate (kg/s).

Unlike CP systems, in which chemical reactants have certain amount of energy per unit mass, EP systems are not energy limited as they can drive the energy generated by solar panels and/or nuclear power sources to generate thrust. Although, theoretically unlimited I_{sp} may be obtained, I_{sp} of EP systems is limited by the available onboard power. Nevertheless, high power applications require heavy power processing units (PPU), and therefore PPU is an important consideration in EP systems design.

The main disadvantage of EP systems is that it offers orders of magnitude lower thrust than CP systems, which means long operation time is required to fulfil a maneuver, and they cannot be used for space launch purpose. However, EP is preferable as a secondary propulsion system for operations such as East-West station keeping maneuver, orbit-rising maneuver and attitude control because they extend spacecraft lifetime, amount of payload to orbit and reduce launch costs. EP systems may also be utilized as the primary propulsion system in planetary and deep space missions.

EP systems are basically divided into three categories. The first is electrothermal propulsion, in which the propellant is heated electrically, and then expanded thermodynamically through a converging-diverging nozzle. The second is electromagnetic

propulsion, in which a current is driven through the propellant, and the Lorentz force ($J \times B$) accelerates the plasma. The final one is electrostatic propulsion, in which ionized propellant is accelerated through an electric field. Table 1.1 lists typical I_{sp} ranges of CP and EP systems. This study focuses on Hall thrusters and an overview of Hall thrusters will be presented in the following section.

Table 1.1 Typical specific impulse ranges of EP and CP systems.

Propulsion System	Specific Impulse [s]
Chemical Propulsion	
Monopropellant	150-250
Bipropellant	250-500
Electrothermal Propulsion	
Resistojet	150-300
Arcjet	500-1000
Electromagnetic Propulsion	
Magneto Plasma Dynamic Thruster	1000-5000
Pulsed Plasma Thruster	1000-1500
Electrostatic Propulsion	
Hall Thruster	1000-5000
Gridded ion thruster	2000-10000

1.3 Overview of Hall Thrusters

Hall thrusters have been under active development since the early 1960's. They have many advantages such as high thrust-to-power ratio, high efficiency at moderate specific impulse range and design simplicity with outstanding in-space experience. In comparison with ion engines, space-charge limitation defined by Child’s law is not an issue as ions are accelerated in quasi-neutral plasma, which enables Hall thrusters to achieve the highest thrust density among the solar EP systems. Hall thrusters might replace gridded ion thrusters and some other EP systems in the future considering recent achievements in the development of these thrusters and ever increasing number of published journal articles/conference papers.

Hall thrusters are usually classified into two types: Stationary plasma thruster (SPT) and thruster with anode layer (TAL). SPT has a dielectric ceramic discharge channel wall, which is usually made of Boron Nitride (BN); whereas TAL has a relatively short metallic channel wall biased to cathode potential to minimize the electron wall loss. Electron and ion current flow through the sheath to channel walls and secondary electron emission, power deposition on anode due to high near-anode electron temperature are power loss

mechanisms in SPT and TAL respectively. Figure 1.1 shows diagram of typical SPT and TAL. Ion bombardment to dielectric walls determines lifetime of SPT; whereas lifetime of TAL is determined by ion bombardment to metallic guard rings. SPTs are the most developed and used Hall thrusters for satellite missions because of their stable (low discharge current oscillations) and reliable operation. Details of the difference between the two version can be found in Ref.2-3.

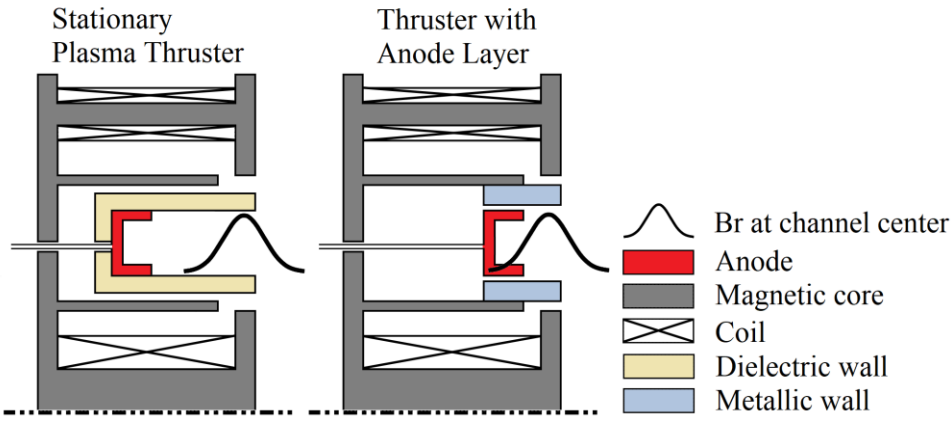

Figure 1.1 Comparison of SPT and TAL.

Hall thruster has a rich heritage and flight history. Table 1.2 and Table 1.3 lists performance of state-of-the-art Hall thruster technology found in the literature.

Table 1.2 Performance of state-of-the-art high power Hall thruster technology.

Model	Developer	Power [kW]	Thrust [mN]	Isp [s]	Efficiency [%]	Type
SPT100 [4]	Fakel	1.35	80	1600	50	SPT
BPT-4000 [5]	Aerojet	4.5	270	1800	58	SPT
PPS 5000 [6]	SNECMA	5	135	2300	50	SPT
D-100 [7]	TsNIIMASH	3.5-15	8-65	2000-4200	60-70	TAL

Table 1.3 Performance of state-of-the-art low power Hall thruster technology.

Model	P [W]	ηA [%]	T [mN]	Isp [s]	Lifetime [h]
SPT 35 [8]	200	30	10	1200	2500
BHT-200 [9]	200	44	13	1390	1700
PlaS-40 [10]	200	31	15	800	4000
SPT 50 [4]	350	35	20	1100	1500
HT 100D [8]	400	40	18	1600	2000

1.3.1 Principles of operation

A Hall thruster usually comprises four main components. An anode which also serves as the gas distributor, magnetic field circuit, plasma discharge channel and cathode as an electron source. Figure 1.2 illustrates a Hall thruster diagram with externally-mounted hollow cathode.

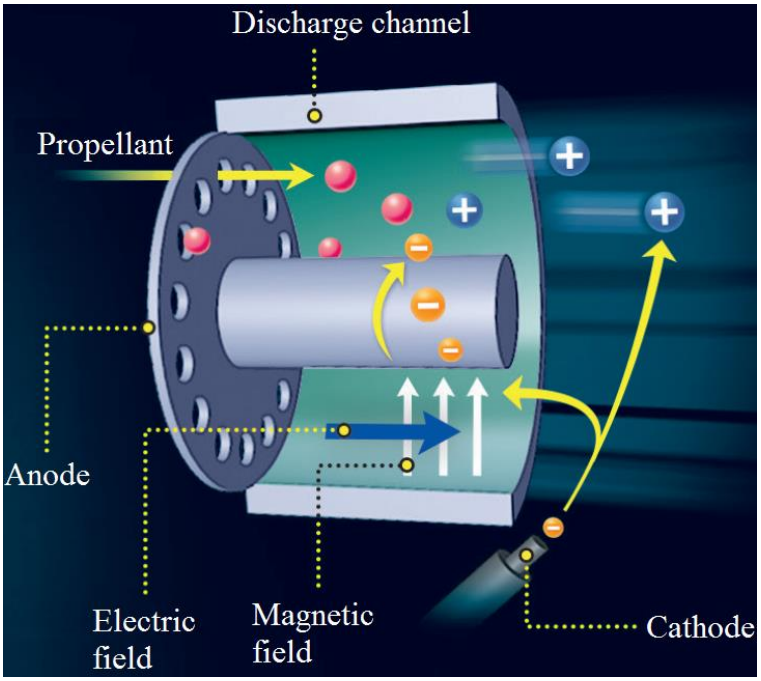

Figure 1.2 A diagram to describe Hall thruster working principle.

Despite Hall thruster is categorized in electrostatic EP systems, it has features of both electric and magnetic thruster. Electrons are injected into a radial magnetic field by the cathode. Magnitude of the magnetic field is strong enough to trap the electrons and insert them into spiral orbit around the magnetic field lines inside the chamber due to the E × B

drift. Hall current, which enables the heavy particle acceleration and thrust generation, is formed by this azimuthal guiding center drift. The entrapped electrons, which ionize the neutral propellant, are gradually accelerated toward the anode and a strong axial electric field is maintained throughout the discharge channel. The ions are too heavy to be affected by the magnetic field. Therefore, they are accelerated by the axial electric field, exhausted in high speed generating thrust according to the Lorentz force law, $F = q(E + v \times B)$, and finally neutralized by electrons emitted from the cathode not to charge the spacecraft. The details of the operating principle can be found in Ref. 2, 3, 11, 12.

1.3.2 Design parameters

This subsection describes some critical design criteria for Hall thrusters. Electron Larmor radius r_e should be much less than characteristic length of discharge channel (L, or plasma length) so that they spiral around magnetic field lines:

$$r_e = \frac{v_{th}}{\omega_c} \ll L \tag{1.3}$$

where v_{th} is electron thermal drift velocity, ω_c is electron cyclotron frequency.

Electron Hall parameter (Ω_e) shows how many times an electron orbits around a magnetic field lines before getting into collision. To let electrons get magnetized and complete many cyclotron orbits, electron Hall parameter should be much greater than unity:

$$\Omega_e{}^2 = \frac{\omega_c{}^2}{\nu^2} \gg 1 \tag{1.4}$$

Where ω_c is electron cyclotron frequency, ν is total collision frequency.

Ionization mean free path λ_i should be much less than unity to obtain high mass utilization efficiency.

$$\frac{\lambda_i}{L} \ll 1 \tag{1.5}$$

Equipotential lines, and thus the direction of electric field lines, inside a Hall thruster are strongly correlated to the magnetic field lines. Then, magnetic field topography can affect ion trajectories even though ions are supposed to be non-magnetized. Electron temperature is constant along a line of magnetic field since electrons can move freely along field lines. Ionization process is linked to electron temperature, and it is a strong factor in power loss mechanisms. Magnetic field topography has direct influence on thruster

performance and lifetime. Therefore, it is arguably the most important consideration in Hall thruster design.

1.4 Statement of Problems

Scientific and commercial interest in small satellites is expected to continue to grow over next decades due to their low cost and short development time. Electric propulsion (EP) systems are critically important for small satellites because they can reduce required propellant mass for attitude and orbit maneuvers one order of magnitude compared to chemical propulsion ones. Among all the current and prospective EP systems, Hall thrusters draw particular attention as they have high thrust-to-power ratio (> 60 mN/kW), efficiency (%50-70), and specific impulse (1000-5000 s), reliable and robust operation (e.g., no grid short circuit), simple design and extensive space flight heritage (Flown since 1970s). However, scaling-down these plasma devices to low power levels (< 500 W) results in a sharp reduction in lifetime (< 4000 hours) because thruster parts protecting the magnetic circuit such as discharge channel walls and pole pieces erode more rapidly due to larger surface-area-to-volume ratio, which directly translates into more intense plasma-wall interactions. Thrust efficiency also tends to degrade as power loss to the discharge channel walls increases.

Plasma wall interactions significantly affect discharge characteristics as well as thruster performance.[13, 14] Fundamentally, it is electric field gradients within a Hall thruster's discharge channel that should be arranged to prevent plasma contacting the wall surfaces. The electric field gradients can be modified through two kinds of approach: 1) optimization of magnetic field profile and 2) position of anode(s). Thrusters employing cusped magnetic fields[15], magnetic shielding[16] and peak radial magnetic field located outside of the channel[17] are all examples of the first approach. Among these the magnetic shielding method was the most successful to lower discharge channel wall erosion, although magnetically shielded Hall thrusters are usually demanding in terms of mass, volume, and power.

The second approach has been investigated under different names and designs. Semenkin[18] varied the discharge channel (guard ring) length of a TAL by extending the end of the anode downstream and studied its effect on the erosion rate. The configuration corresponding to the limit of zero channel length was named the "external anode layer thruster". Mazouffre et al.[19] moved the anode of a SPT towards the channel exit, and characterized its effect under the name of "Wall-less Hall thruster (WL-HT)". Placing the anode closer to the thruster exit certainly helps reduce discharge channel wall erosion as the acceleration region is shifted outside of the thruster body.

We study the second approach with an alternative Hall thruster design called the "external discharge plasma thruster (XPT)". The XPT is the first Hall thruster that operates without any annular or cylindrical discharge channel walls. In particular, it is expected to operate in very low power regime where conventional Hall thrusters cannot prevent high ion/electron losses to the channel walls. The XPT might provide a promising solution to the long-standing efficiency problem of low power Hall thrusters. It can significantly reduce thruster head mass, and also its simple design can minimize failure modes of a thruster.

Furthermore, a first-principles description of electron transport and cathode coupling for accurate numerical models is needed to develop a plasma code that can reliably predict Hall thruster performance and lifetime. Numerical simulations are important to optimize performance of Hall thrusters and understand discharge chamber plasma physics in that they are cheaper and faster compared to experiments and they provide physical information often difficult to obtain from experiments. For example, quantifying plasma properties inside the discharge chamber is a difficult task as interaction of probes with highly energetic particles would affect the measurement result. For the present, numerical simulations are only assistive methods and unlikely to replace the experiment since complex plasma behavior is far from being well understood. Reduced wall effects in the XPT can facilitate study of the interaction between the plasma and magnetic field, which can deepen our understanding of these interactions. In addition, the simpler boundary conditions will facilitate improvement of the prediction accuracy of plasma codes.

The goal of this study is to carry out a proof of concept experiment and, to try to explain how the XPT achieves similar propellant utilization efficiency compared to conventional Hall thrusters at the same power levels without a physical ionization chamber. Table 1.4 compares the XPT and the other members of Hall thruster family. Relative magnetic field strength is a measure of the maximum radial magnetic field on discharge channel centerline at thruster exit.

Table 1.4 Comparison of Hall thrusters.

	SPT/TAL	MS HET	HEMPT	WL-HT	XPT
Erosion prevention method	None	Magnetic field shape	Magnetic field shape	Anode location	Anode location
Anode front	Discharge channel	Discharge channel	Discharge channel	Thruster exit	Outside thruster body
Geometry	Co-axial	Co-axial	Cylindrical	Co-axial	Co-axial
Discharge channel	Dielectric/ Metallic	Dielectric	Dielectric	Dielectric	None
Magnetic circuit	Coil/magnet, iron core, pole piece and screen	Coil, iron core, pole piece and screen	Only magnets	Coil/magnet, iron core, pole piece and screen	Only magnets
Relative magnetic field strength	X/2X	X	-	X	4X

1.5 Research Objectives

The research objectives listed below were pursued:

i. To question the necessity of discharge channel walls in Hall thrusters by characterizing an alternative Hall thruster design both experimentally and numerically in order to address efficient scaling down issue

ii. To conduct a sensitivity analysis method for a fully kinetic code, and study model uncertainties in it for better prediction accuracy of Hall thruster simulation

iii. To apply this sensitivity analysis method to the simulations of proposed alternative Hall thruster design, and study the physics of its operation

iv. To develop a plasma device that might be useful to deepen our understanding on interaction between plasma and magnetic field through its highly simplified boundary conditions, and a standard test bed for benchmarking accuracy of various plasma codes

1.6 Dissertation Outline

This work comprises 6 chapters, and the organization is as follows. Chapter 2 introduces design of external discharge plasma thruster, and describes its key physics.

In chapter 3, firstly a sensitivity analysis is conducted to validate a fully kinetic particle-in-cell (PIC) code, and to investigate the importance of uncertainties associated to physical parameters. Then, the external discharge plasma thruster is numerically investigated, and its thrust performance/ plasma properties are presented.

Chapter 4 describes the experimental setup and facilities. It presents, and analyzes results related to thrust performance, discharge current oscillations, farfield ion current density, plasma properties and visual observations made during the thruster operation. Also it includes a description of a simple method to measure anode and wall temperature. Appendix section evaluates suitability of a commercial precision balance as an alternative micro-Newton resolution continuous thrust stand on a vertically oriented low power Hall thruster.

Chapter 5 discusses propellant ionization efficiency, ionization and acceleration regions, discharge current stability, thruster front wall deposition and background pressure effect. It compares the simulation and the experimental results as well.

Chapter 6 summarizes major conclusions, provides recommendations to improve thruster performance, and identifies some potential applications.

References

[1] Choueiri, E. Y., "A Critical History of Electric Propulsion: The First 50 years (1906-1956)," Journal of Propulsion and Power, Vol. 20, No. 2, 2004, pp. 193-203.

[2] Zhurin, V. V., Kaufman, H. R., and. Robinson, R. S., "Physics of Closed Drift Thrusters," Plasma Sources Science and Technology, Vol. 8, No. 1, 1999, pp. R1-R20.

[3] Choueiri, E., "Fundamental difference between the two variants of Hall thrusters: SPT and TAL," 37th AIAA/ASME/SAE/ASEE Joint Propulsion Conference, Salt Lake City, 2001. AIAA 2001–3504.

[4] Kim, V., et al. "Electric Propulsion Activity in Russia," *27th International Electric Propulsion Conference,* Pasadena, October 15-19, 2007, IEPC-01-05.

[5] de Grys, K., et al. "4.5 kW Hall Thruster System Qualification Status," *41st AIAA/ASME/SAE/ASEE Joint Propulsion Conference and Exhibit*, Tucson, July 10-13, 2005, AIAA-2005-3682.

[6] Dudeck, M., Doviel, F., Arcis, N., and Zurbach, S., "Plasma Propulsion for Geostationary Satellites and Interplanetary Spacecraft," Romanian Journal of Physics, Vol. 56, 2011, pp. 3–14.

[7] Garkusha, V., et. al., "Electric Propulsion Activity in TsNIIMASH," *24th International Electric Propulsion Conference*, Moscow, September 19-23, 1995, IEPC-95-09.

[8] Ducci, C., et al. "HT100D performance evaluation and endurance test results," 33rd International Electric Propulsion Conference, Washington D.C., October 6-10, 2013, IEPC-2013-140.

[9] Cheng, S. and Martinez-Sanchez, M., "Hybrid Particle-in-Cell Erosion Modeling of Two Hall Thrusters," *Journal of Propulsion and Power,* Vol. 24, No. 5, pp. 987–998, 2008.

[10] Potapenko, M. Y., et al. "PlaS-40 Development Status : New Results," *34th International Electric Propulsion Conference*, Kobe, July 4-10 2015, IEPC-2015-99 / ISTS-2015-b-99.

[11] Goebel, D., and Katz, I., "Fundamentals of Electric Propulsion: Ion and Hall Thrusters," Wiley, Hoboken, NJ, 2008.

[12] Boeuf, J-P., "Tutorial: Physics and modeling of Hall thrusters," *J. Appl. Phys.* 121 011101.

[13] Morozov, A. I., and Savelyev, V. V., *Reviews of Plasma Physics* (Springer Science+Business Media, New York, 2000).

[14] N. Gascon, M. Dudeck, and S. Barral, "Wall Material Effects in Stationary Plasma Thrusters: l. Parametric Studies of an SPT-100," *Physics of Plasmas*, Vol. 10, pp. 4123-4136, 2003.

[15] Kornfeld, G., Koch, N., and Harmann, H. P., "Physics and Evolution of HEMP-Thrusters," *30th International Electric Propulsion Conference*, Florence, Italy, September 17-20, 2007, IEPC-2007-108.

[16] Mikellides, I. G., Katz, I., Hofer, R. R., Goebel, D. M., "Magnetic Shielding of

Walls from the Unmagnetized Ion Beam in a Hall Thruster", *Applied Physics Letters*, 102, 023509 (2013).

[17] Schmidt, D. P., Meezan, N. B., Hargus, W. A., and Cappelli, M. A., "A Low-power, Linear-geometry Hall Plasma Source with an Open Electron-drift," *Plasma Sources Science and Technology*, Vol. 9, 2000, pp. 68–76.

[18] Semenkin, A. V., "Investigation of Erosion in Anode Layer Thruster and Elaboration High Life Design Scheme," *23th International Electric Propulsion Conference*, Seattle, 1993, IEPC-93-231.

[19] Mazouffre, S., Tsikata, S., and Vaudolon, J., "Development and Experimental Characterization of a Wall-less Hall thruster," *Journal of Applied Physics*, 116, 243302 (2014).

CHAPTER 2

External Discharge Plasma Thruster

Contents

"I am enough of an artist to draw freely upon my imagination. Imagination is more important than knowledge. For knowledge is limited, whereas imagination encircles the world!"

Albert Einstein

2.1 Key Physics

Figure 2.1 shows a typical Hall thruster, which comprises an anode, an annular discharge channel, a magnetic circuit and a cathode. The anode placed at one end of the discharge channel also functions as a propellant distributor. The magnetic circuit circumscribes the discharge channel, and its main components are a ferromagnetic core, pole pieces, magnetic screens and electromagnetic coils. A radial magnetic field (0.01 – 0.03 T) traps free electrons ejected by the cathode and inserts them into spiral orbits. The entrapped electrons ionize the propellant gas through collisions and gradually diffuse from the cathode to the anode maintaining a strong axial electric field throughout the discharge channel. Axial electric field crossed with the radial magnetic field forces the electrons to drift azimuthally, thus forming the Hall current. Interaction of the Hall current with the

radial magnetic field enables quasi-neutral plasma acceleration. The resulting ion beam is neutralized by the electrons emitted from the cathode not to charge the spacecraft. The problem in this process is that not only an axial electric field but also a radial electric field exists inside the discharge channel. It imparts enough energy to the impinging ions or electrons to erode the discharge channel walls and the poles that protect the coils. The discharge channel thickness decreases over time, and the coils get exposed to hot plasma and eventually fail to operate. The external discharge plasma thruster (XPT) overcomes this problem by producing and sustaining a plasma discharge fully outside a non-anodic cavity giving the thruster its name, in analogy to the differentiation made between internal and external combustion engines.

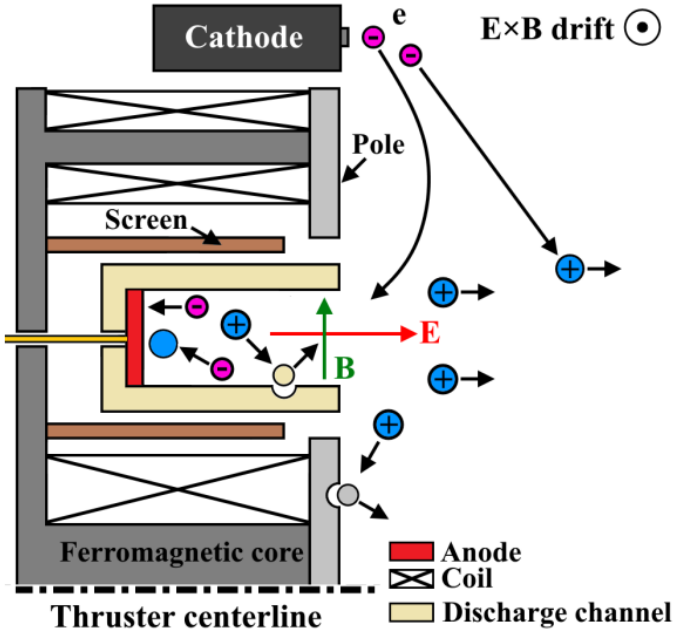

Figure 2.1 A schematic of a typical Hall thruster.

A schematic of the XPT discharge is shown in Figure 2.2. The XPT is a simplified annular geometry Hall thruster and it mainly consists of an annular anode, a pair of hollow cylindrical permanent magnets and a cathode. The propellant gas is introduced at the upstream end of the anode cavity from the holes azimuthally arranged on the dielectric front wall. The permanent magnets produce a magnetic field, which is stronger at magnetic cusps on the front wall than that at the anode centerline due to curvature of the magnetic field lines. This rise to an effect called magnetic mirroring as magnetic dipole moment of a particle ($\mu = mv_{\perp}/2B$) is conserved along a magnetic field line. Electrons emitted from the cathode undergoes periodic motion along the magnetic field lines if magnetic mirror

ratio ($r_{mirror} = B_{max}/B_{min}$) is higher than unity, and pitch angle of the electrons is large ($v_{\perp} > v/\sqrt{r_{mirror}}$). Magnetic mirroring has been widely used to confine hot deuterium plasma in fusion studies. The XPT is a magnetic confinement device with the magnetic mirror ratio varies between 2 and 12 from axial distances z = 0 mm to z = 10 mm. The trapped electrons bounces forward and backwards between the mirror points formin an electron cloud rotating in the E×B direction. Neutral atoms introduced at the upstream end of the anode cavity enter into the the rotating electron cloud, and are mostly ionized as the thermal velocity of the electrons ($v_{th} = \sqrt{8k_BT/m\pi} = 2.6x10^6$ m/s for 15 eV), and neutral atoms ($v_n = 3.4x10^2$ m/s for xenon and an anode temperature of 700 K) differs by four orders of magnitude. The radial magnetic field reduces axial electron mobility making it possible for the quasi-neutral plasma to maintain strong axial electric field. As the ions are accelerated outward by the electric field, thrust is generated according to the Lorentz force law, $F = q(E + v \times B)$.

The ionization and acceleration regions overlap similar to a typical Hall thruster; however, ionization of neutrals and acceleration of ions are expected to take place in a very narrow region near the anode surface and completely in the open space outside of the thruster structure.

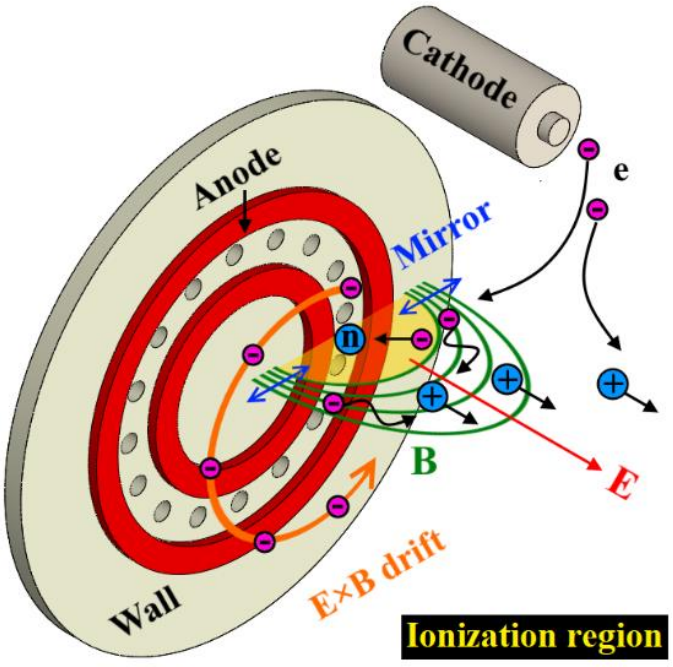

Figure 2.2 A schematic of the XPT discharge.

Figure 2.3-4 shows a radial electric field (E_r) and electron temperature (T_e) distribution of XPT for 250 V - 0.95 mg/s operating condition respectively, calculated by a full kinetic code whose details can be found in Chapter 3. Electrons move radially in the inward direction in the red region where the electric field is positive, while they move in opposite direction in the blue region where the electric field is negative as shown in Fig. 2.4, confirming the electron bouncing between the mirror points. The mirroring might occur at the location marked by the purple double arrow lines shown in Fig. 2.4 because the electron temperature decreases sharply.

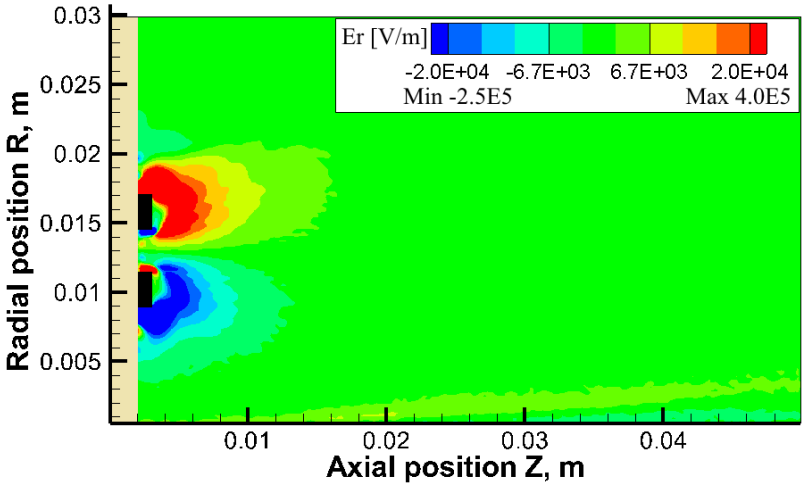

Figure 2.3 Simulated radial electric field distribution of the XPT for 250 V - 0.95 mg/s.

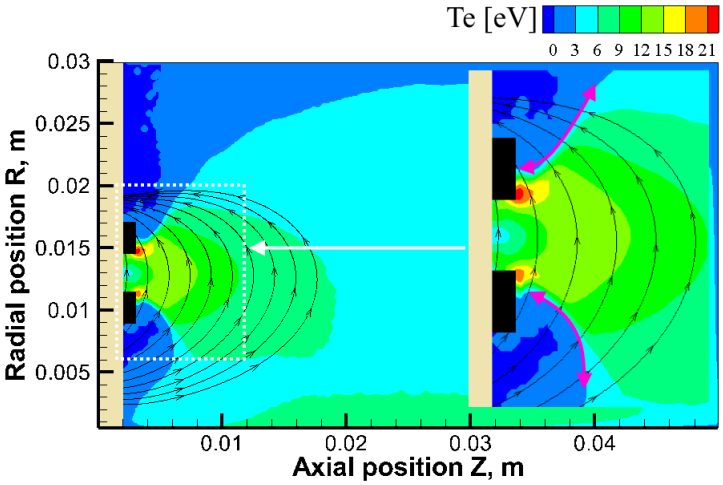

Figure 2.4 Simulated electron temperature distribution of the XPT for 250 V - 0.95 mg/s. *The purple double arrow lines indicate possible electron mirroring points.*

2.2 Thruster geometry

Figure 2.5 shows a section view of the first prototype and electrical diagram. Propellant gas is fed into the thruster structure through an annular tube fitting, which is concentrically aligned both with symmetry axis of the thruster and the anode disc. A planar front wall made of boron nitride electrically isolates the anode made of molybdenum from the thruster body, and it has plurality of holes arranged azimuthally releasing propellant gas into slots that are symmetrically distributed on the anode. Structural material is made of a soft and easy to machine diamagnetic metal, preferably copper. Copper was selected as the structural material because it is a soft diamagnetic metal that is easy to shape and work.

Neutral gas density is high behind the front wall, so the anode is attached to the front wall by alumina flat head screws as a precaution against arcing. Thermal stresses were calculated by commercial software to ensure structural safety of the thruster components especially the ceramic front wall. The thruster passively cools itself via radiation to vacuum chamber walls.

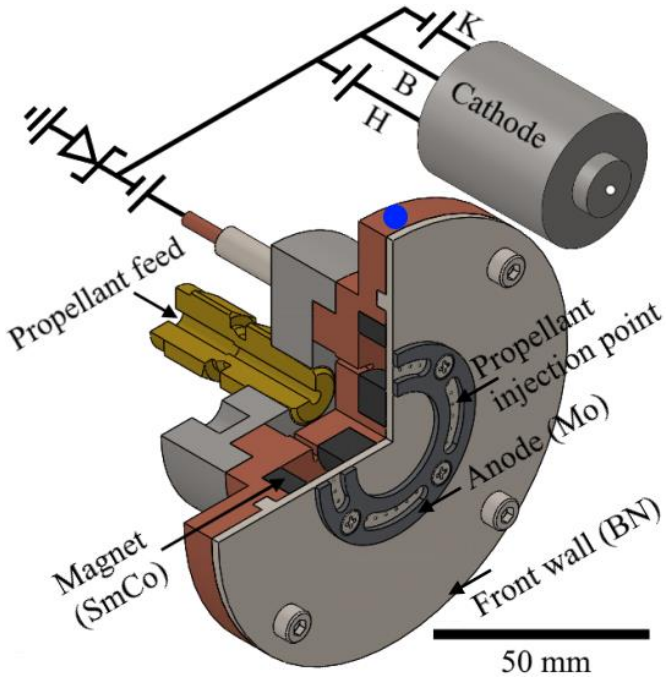

Figure 2.5 Thruster cross section view and electrical diagram. *Blue dot indicates thermocouple location.*

2.3 Magnetic circuit

The magnetic circuit is composed of a pair of samarium cobalt (SmCo) cylindrical permanent magnets concentrically aligned with the anode disc to produce radially extending magnetic field lines. Figure 2.6 shows a model of the magnetic circuit that is created and solved in FEMM (Finite Element Method Magnetics)[1] on 2D axisymmetric domain.

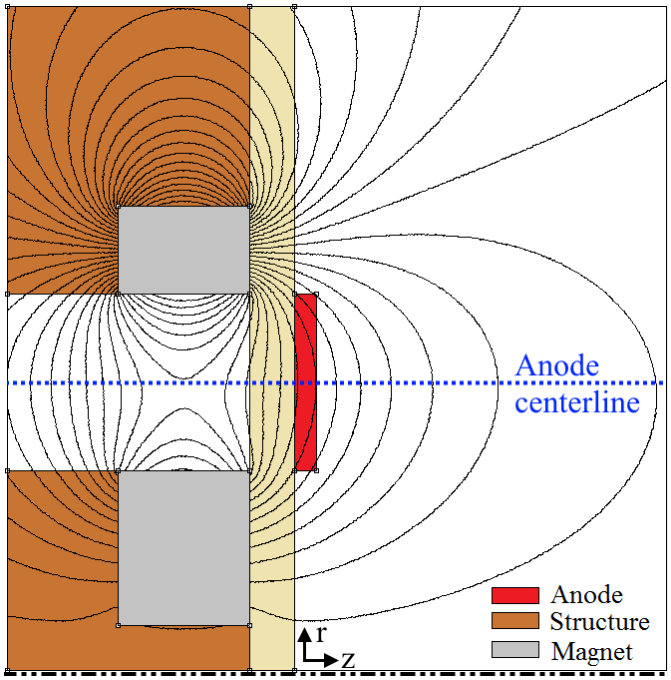

Figure 2.6 Magnetic circuit model.

Fig. 2.7 shows Br distribution of the XPT thruster head along the anode centerline. The largest radial magnetic field strength (Br) along the anode center line is about 0.12 T. The anode is located downstream of the magnetic field maximum, and the radial magnetic field profile has a negative-only gradient ($dB/dz < 0$). The negative-only gradient was also confirmed by measuring the radial magnetic field strength along the anode centerline through a Gauss meter. Anode centerline means the line passing through the midpoints between the inner and outer edges of the anode disc. Even though the radial magnetic field strength could not be measured up to 2.4 mm from the anode front surface due to the transverse probe tip structure, a good agreement is observed between the measured and computed values.

Distribution of neutral density calculated for 1.43 mg/s xenon mass flow by a 2D axisymmetric DSMC model[2] is also shown in Fig. 2.7. Note that neutral density in front of the slots should be higher due to the asymmetric injection.

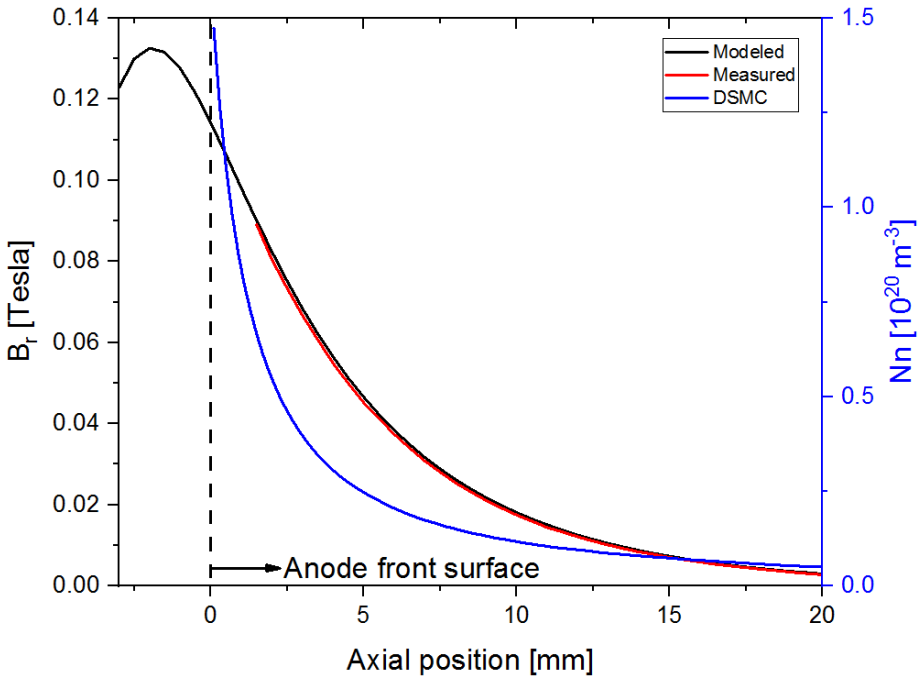

Figure 2.7 Br Nn distributions of the XPT thruster head. Br and Nn are along the anode centerline.

Neutral density (n_n) at the center of the anode front surface (z = 0 mm) is $1.5\text{x}10^{20}$ m^{-3} from Fig. 2.7. Assuming an average electron temperature of 15 eV at 250 V anode potential, total collision cross section (S_{total}) is found to be $3.6\text{x}10^{-19}$ m^{-2} from the fitted curve in Ref 3. Then, total collision frequency ($\nu_e = n_n v_{th} S_{total}$), Hall parameter ($\Omega_e = \omega_{ce}/\nu_e$) and electron Larmor radius ($r_e = \omega_{ce}/v_{th}$) at z = 0 mm where B_r = 0.11 Tesla are equal to $1.4\text{x}10^{8}$ Hz, 147 and 0.13 mm respectively. The Hall parameter is much larger than unity satisfying the critical Hall thruster design criteria, and it increases up to 300 at z = 2 mm where $n_n = 5.3\text{x}10^{19}$ m^{-3}(without plasma condition) and B_r = 0.08 Tesla implying that the thruster strongly confines electrons, and provides high neutral density near the anode surface, which, as a result, starts cascade ionization in a very narrow region.

2.4 Magnetic mirror ratio

Figure 2.8 shows measured magnetic flux density and flux lines of the magnetic circuit of the XPT, and Table 2.1 gives magnetic mirror ratio for the magnetic flux lines shown in Fig. 2.8. It can be seen that the magnetic mirror ratio is larger than unity even in the near-anode region. In addition, pitch angle of the electrons, the angle between the velocity vector of electrons and the magnetic field vector, should be large ($v_\perp > v/\sqrt{r_{mirror}}$) because the electrons with the small pitch angle can escape the magnetic mirror. Due to the axial electric field and radial magnetic field we can expect that electrons will have a large pitch angle especially in the near-anode region.

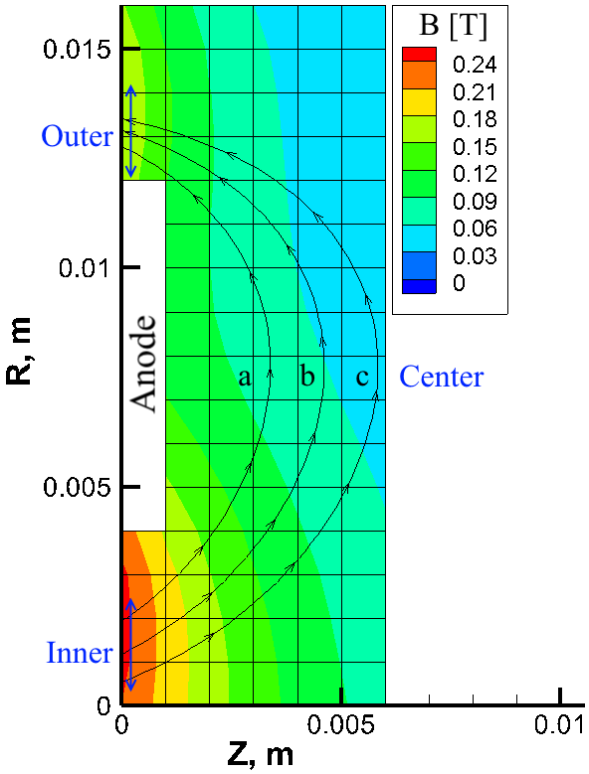

Figure 2.8: Measured magnetic flux density and flux lines.

Table 2.1 Magnetic mirror ratios for the magnetic flux lines shown in Fig. 2.8.

Line	B_{inner}	B_{center}	B_{outer}	B_{inner}/B_{center}	B_{outer}/B_{center}	Anode-to-line distance*
a	0.251	0.0754	0.176	3	2	2.4 mm
b	0.249	0.0596	0.178	4	3	3.6 mm
c	0.244	0.0469	0.179	5	4	4.8 mm

* Measured at the anode centerline.

2.5 Thermal consideration

The SmCo magnets used in this study have the maximum allowable temperature of 330 °C. If temperature of the magnets exceeds this value, they will suffer irrecoverable losses in magnetism, which may cause to large axial electron current decreasing thrust efficiency due to weaker confinement.

When the thruster is in continuous operation at approximately 400 W, temperature of a point on the thruster structure near the front wall (See the blue dot in Fig. 2.5) was monitored by a K-type thermocouple for more than 2 hours. Fig. 2.9 shows temperature of the thruster head as a function of time. The rate of change of the temperature of the thruster structure was negligible at a temperature of approximately 220 °C. The thruster structure reaches thermal equilibrium at a temperature well below the maximum operating temperature of the magnets. Magnetic field degradation is therefore not considered as an issue assuming that the thruster structure will quickly accommodate to temperatures of the inner and outer magnets due to relatively short distance (< 30 mm) between the measurement point and the magnets.

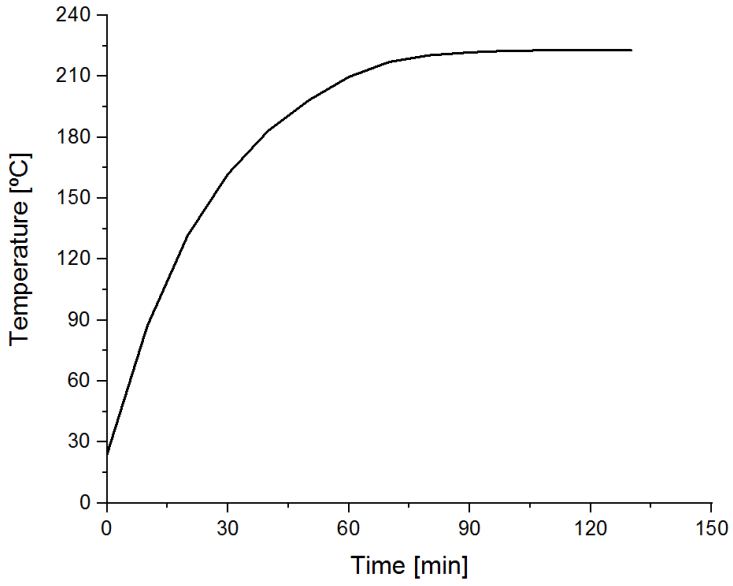

Figure 2.9 Thruster head temperature as a function of time.

2.6 Summary of features

Figure 2.10 shows a schematic comparison of the XPT, wall-less Hall thruster and an external anode layer thruster. The XPT is distinguished by the following characteristics:

1) There is literally no discharge channel side walls or guard rings, so ionization of neutrals and acceleration of ions occur completely in the open space outside of the thruster structure,

2) Radial magnetic field has negative-only gradient and its strength is uncommonly high (> 0.1 Tesla),

3) The front surface of the anode extends outside of the thruster exit plane and is located downstream of the magnetic field maximum,

4) It does not have any ferromagnetic cores, pole pieces, magnetic screens, or electromagnetic coils and related power supplies, which are the heaviest component of Hall thrusters, and

5) Propellant feed is not uniform, and yet the XPT offers additional freedom of design optimization to make uniform propellant feed or extremely non-uniform easily by changing the anode design.

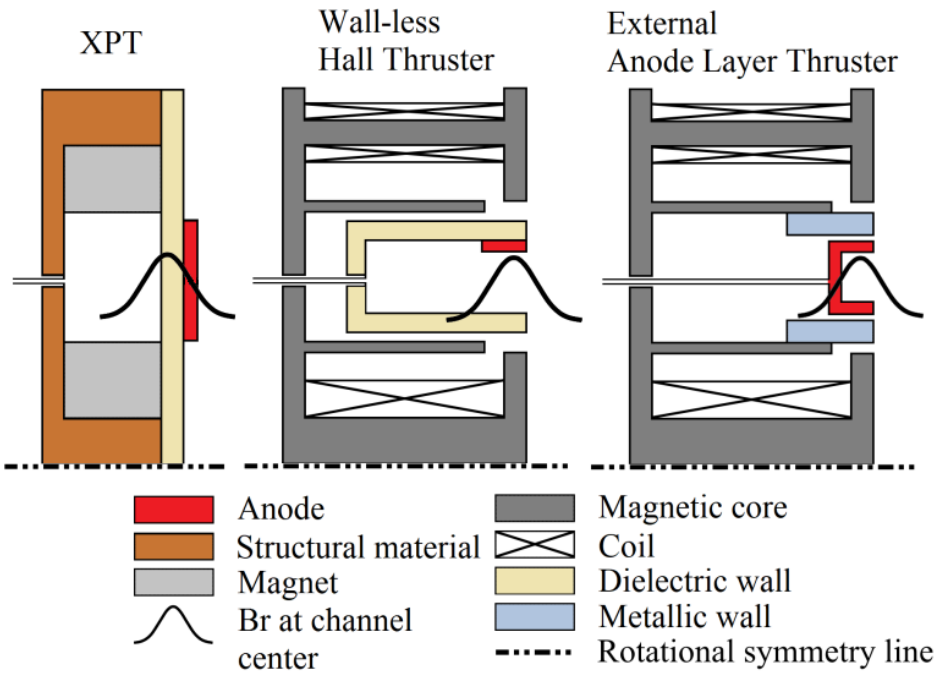

Figure 2.10 Schematics comparison. *Cathode is not shown.*

References

[1] Meeker, D.C.: Finite Element Method Magnetics, Version 4.2 (2010).
[2] Cho, S., Komurasaki, K., and Arakawa, Y.: Kinetic Particle Simulation of Discharge and Wall Erosion of a Hall thruster, *Physics of Plasmas*, Volume 20, Issue 6, 063501, 2013.
[3] Subramanian, K. P., and Kumar, V., "Total Electron Scattering Cross Sections for Argon, Krypton, and Xenon at Low Electron Energies," *Journal of Physics B: Atomic, Molecular and Optical Physics*, Vol. 22, No. 15, 1987.

CHAPTER 3

Numerical Investigation

Contents

"It doesn't matter how beautiful your theory is, it doesn't matter how smart you are. If it doesn't agree with experiment, it's wrong."

Richard P. Feynman

3.1 Introduction

One particular problem with the external discharge plasma thruster (XPT) may be considered as low propellant utilization efficiency and high plume divergence angle since there are not any physical walls to confine neutral propellant gas. It is needed to simulate thrust performance of this conceptual design before moving on to experiment. In this chapter, we therefore first make sensitivity analysis of a fully kinetic code particle-in-cell code on a conventional Hall thruster using existing experimental data. The main advantage of the fully kinetic code particle-in-cell used in this study is that it can self-consistently solve the energy distribution of the particles with relatively less computational cost due to use of a semi implicit field solver and an artificial mass ratio model. We then simulate the XPT by the fully kinetic code, and present the numerical results.

3.2 Validation of a Fully Kinetic Particle-In-Cell Code

A Hall thruster[1] is a type of electric propulsion used for satellite missions like station-keeping, orbit transfer or deep space exploration. Hall thrusters are preferable due to many advantages, such as high thrust density (no space-charge limitation defined by Child's law as ions are accelerated in quasi-neutral plasma), moderate specific impulse, and outstanding in-space experience. To improve/optimize the performance of Hall thrusters and understand discharge chamber plasma physics, numerical simulations are important in that they are cheaper and faster compared to experiments and they provide physical information often difficult to obtain from experiments. For example, quantifying plasma properties inside the discharge chamber is a difficult task as the interaction of probes with highly energetic particles would affect the measurement result. For the present, numerical simulations are only assistive methods and unlikely to replace experiments since complex plasma behavior is far from being well understood. There are three main approaches (Fluid, fully kinetic, and hybrid) in modeling Hall thrusters.[2-4] Fluid codes treat both electrons and ions as fluid and assume Maxwellian velocity distribution function (VDF).[5] Fully kinetic codes treat electrons and ions as discrete particles and compute VDF self-consistently.[6] As for hybrid codes, electrons are treated as a fluid, whereas ions are treated as particles, compromising the difference between fluid and kinetic approaches.[7, 8] Fully kinetic codes are computationally expensive and time-consuming; however, they can capture non-equilibrium features unlike the fluid and hybrid codes. For instance, plasma-wall sheath is self-consistently modeled in fully kinetic codes, while a sheath model is required for fluid and hybrid codes. It is therefore expected that fully kinetic simulation is potentially capable of high-accuracy predictive modeling. Nevertheless, prediction accuracy of fully kinetic codes is decreased by various sources of uncertainty and error, which involves both numerical discretization errors and uncertainties in model physical parameters. It is important to investigate these errors/uncertainties and quantify their confidence range for the realization of predictive modeling. However, there are few previous studies on this subject so far, especially for the physical parameter uncertainties of fully kinetic simulation.

This subchapter serves as the first step of uncertainty quantification of fully kinetic Hall thruster modeling. As for the sensitivity analysis, a one-factor-at-a-time sensitivity analysis method was preferred due to its simplicity. The one-factor-at-a-time method involves repeatedly varying one parameter value in a presumed confidence range at a time while keeping others fixed at their nominal value. Previously, Watanabe et al.[9] adopted this approach to conduct a sensitivity analysis of the input parameters of a numerical tool to validate grid erosion of an ion thruster. In the following sections, the results of our sensitivity analysis are presented, and the significance of the physical parameters is discussed.

3.2.1 Hall thruster

A laboratory model magnetic-layer Hall thruster of The University of Tokyo named UT-62[10], and having an outer-channel diameter of 62 mm was chosen to be the test bed. The electrical diagram of the experimental setup is shown in Figure 3.1 (a).

3.2.2 Code description

A 2D3V fully kinetic Particle-in-Cell (PIC)/Direct Simulation Monte Carlo (DSMC) code was used in this study. To compensate for the lower electron mobility across the magnetic field due to the lack of azimuthal resolution, Bohm diffusion was implemented in terms of virtual scattering collision[11] between neutrals and electrons as $\nu_{Bohm} = 1/16(eB/m_e)$. The total collision frequency is defined as:

$$\nu_{total} = \nu_{elastic} + \nu_{ionization} + \nu_{excitation} + \nu_{Bohm} \tag{3.1}$$

To speed-up the code and make the simulation feasible, so-called macroparticles and an artificial mass ratio model were used. The magnetic field induced by the plasma was considered to be negligible. The magnetic field was calculated using Finite Element Method Magnetics (FEMM).

A uniform rectangular grid in a cylindrical coordinate system (r, z, θ) was adopted as shown in Fig. 3.1 (b), and the cell interval was arranged in the same order as the dielectric wall sheath. A fixed potential was applied to the anode and the plume boundary, and the space potential φ was calculated according to the Poisson's equation. A semi-implicit solver was used because it stabilizes the simulation even at larger time steps than electron plasma frequency and larger grid spacing than Debye length, thus remarkably reducing computational cost. The grid spacing was decided according to the parametric study conducted by Cho et al. [13] Even though the Debye length (~0.05 mm) is not resolved, plasma oscillations such as discharge current oscillation are captured by the semi-implicit solver. To calculate the particle trajectories of all species, the Lorentz force equation of motion is solved using the 4th-order Runge-Kutta method. Electric and magnetic forces were applied via the PIC method while inter-particle collisions were implemented using DSMC. Only singly charged ions, doubly charged ions, electrons, and neutrals were simulated. The computational time-step was chosen such that the plasma oscillation and electron cyclotron motion were captured.

The code was parallelized using the Message Passing Interface (MPI) and Portable, Extensible Toolkit for Scientific Computation (PETSc), and simulations were conducted using a quad-core 3.4 GHz CPU personal computer. Further details of the simulation methodology can be found elsewhere.[12, 13]

3.2.3 Simulation conditions

The discharge voltage, mass flow rate, and coil current were set to 300 V, 1 A_{eq} (1.361 mg/s for Xenon), and 2 A respectively. Figure 3.2 plots the radial magnetic field strength distribution along the inner/outer wall surfaces and discharge channel centerline for a 2 A coil current. Magnetic field strength varied between 0.005 - 0.03 Tesla along the discharge channel centerline and its strength increased from the anode towards the thruster exit. Simulations for each case were run for 0.4 million steps. All of the performance results and plasma distribution plots were time-averaged. Table 3.1 lists simulation nominal physical parameters. Additionally, the measurement results of discharge current, thrust, and anode efficiency were tabulated.[13]

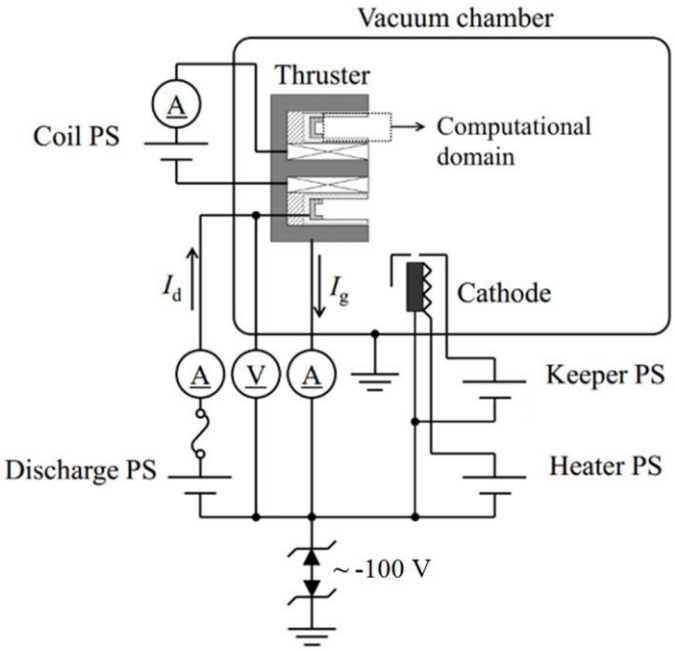

(a) Electrical diagram of the experimental setup. *PS = Power supply*

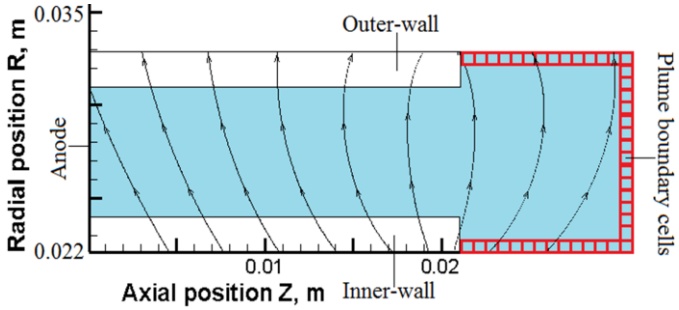

(b) Close-up view of computational domain. *Lines with arrows represent the magnetic field applied.*

Figure 3.1 UT-62 Hall thruster schematics.

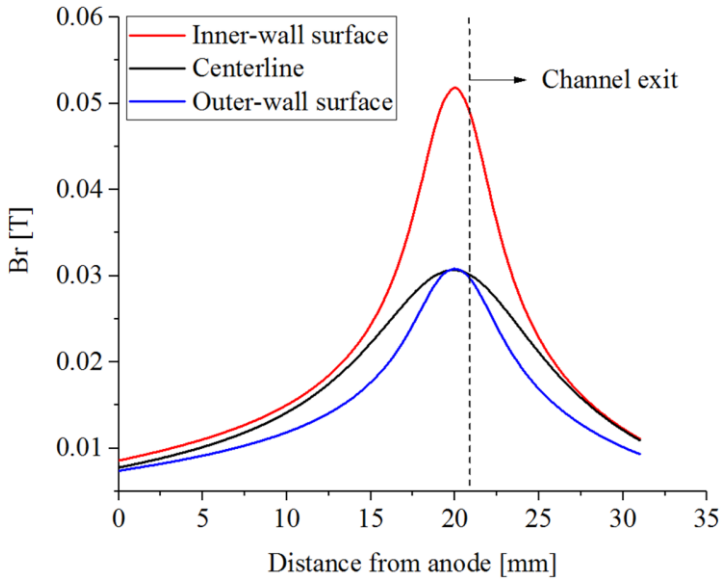

Figure 3.2 Radial magnetic field distribution of UT-62 Hall thruster.

All of the simulation results were time-averaged over 0.1 ms samplings every 100 simulation steps. The convergence of the simulation was judged by the time-history of the total number of simulation particles. The efficiency analysis scheme of Brown[14] was used to investigate the details of thruster performance (see appendix).

Table 3.1 Simulation conditions for UT-62 Hall thruster.

Thruster operation conditions	Discharge voltage [V]	300
	Xe mass flow rate [mg/s]	1.36
	Magnetic coil current [A]	2.0
Numerical settings	Time step [s]	5×10^{-10}
	Macroparticle size	1×10^{7}
	Mass ratio m_i/m_e	96.4
	Grid spacing [mm]	0.2
Experimental results	Discharge current [A]	0.99
	Thrust [mN]	16.3
	Anode efficiency [%]	32.6

3.2.4 Physical parameters investigated in this study

The physical parameters investigated in this study involve the thermal accommodation coefficient of heavy particles, anode temperature, wall temperature, Bohm diffusion coefficient, cathode coupling potential drop, electron injection current to the computational domain, and background pressure effect. This set of parameters essentially comprises all of the physical parameters of our fully kinetic model, and each of them can have a non-trivial influence on the simulation results. The thermal accommodation coefficient and anode/wall temperatures are expected to change the neutral flow inside the discharge channel.[15] The noble Bohm diffusion coefficient is known to dominate the electron cross-field transport.[16] Cathode potential drop and electron injection current are related to the thruster-cathode coupling, which can mainly influence the voltage utilization of ions.[17] Additionally, the background pressure effect[18] is attracting increasing attention from the Hall thruster community[19] though it is an uncertainty of the experiment rather than simulation. Uncertainties in all of these physical parameters can be categorized under epistemic uncertainty[20] or systematic error, which means there is a true deterministic value for each parameter, although we do not know about its exact value due to lack of accessibility (i.e., unable to measure, measurement error, etc.).

In numerical simulation, the deficiencies of the models can be divided into two subcategories: 1) Errors associated with numerical methods, and 2) uncertainties in code input parameters related to physical phenomena, which will be called “physical parameters” hereafter. Errors in numerical calculations come from approximations to solve partial differential equations and physical recovery models, such as macroparticle number and mass ratio. Uncertainties in physical parameters come from lack of experiments to measure certain parameters, such as thermal accommodation coefficient and lack of knowledge to model complex phenomena like Bohm diffusion. The scope of this paper is the sensitivity analysis of physical parameters, even though consideration of errors will be discussed in the following sub-sections. Table 3.2 summarizes the physical parameters investigated in this study and their presumed nominal, maximum, and minimum values. This set of parameters essentially comprises all of the physical parameters of our fully kinetic model. The rest of this section serves to explain the detail of the investigated parameters and how the parameter ranges was decided.

Table 3.2 Physical parameters investigated for UT-62 Hall thruster. *A: Thermal accommodation coefficient and anode/wall temperatures, B: Bohm diffusion coefficient, C: Cathode coupling voltage, E: Electron injection current, and BP: Background pressure effect.*

Parameter		Minimum	Nominal	Maximum
	TAC	0.5	0.9	1.0
A	T_{anode} [K]	900	500	500
	T_{wall} [K]	900	700	500
B		0	1/16	1/8
C [V]		0	0	30
E [Aeq]		1	2	3
BP [Pa]		-	0	6.7×10^{-3}

3.2.4.1 Range of physical parameters related to neutral flow

In the fully kinetic code, mainly two kinds of parameters have a major impact on neutral propellant flow. The first one is the thermal accommodation coefficient (TAC), which defines the percentage of heat transfer between heavy particles (ions and neutrals) and solid wall surfaces. A TAC of 1.0 means the wall-incident heavy particles will be fully accommodated; that is to say they will be bounced back with a kinetic energy corresponding to the wall temperature, whereas a TAC of 0.0 means the incident particles will be reflected at the wall surface with their initial energy before collision. Since typically heavy particles hit the wall with energy much higher than the wall temperature, the higher TAC slows down the neutral propellant increasing the resident time in the channel, which can cause a significant impact on discharge. The experimental work of Kim et al.[21] suggests a xenon accommodation coefficient on boron nitride between 0.6 and 0.8 for ion energies between 100 and 400 eV under a controlled experimental configuration. In the real configuration inside a Hall thruster channel, the uncertainty of wall-surface roughness, impurity, temperature, etc. are considered to further broaden the confidence range of the exact TAC value. Therefore, a TAC value of 1.0 was selected as the maximum case, whereas 0.5 was assumed to be the minimum case. Note that, for simplicity, the TAC was assumed to be the same for both ions and neutrals against either the channel wall or anode. Besides, 100% momentum accommodation assumed that all of the particles leave the wall with the velocity sampled from the Maxwellian distribution. As for the injection condition of the neutrals, their velocity components were randomly assigned according to a half-range Maxwellian distribution.

The second parameter is wall temperature, which essentially affects the energy of the particles accommodating the walls and particles injected from the anode. Direct measurement of the wall surface temperature during the thruster operation is a complicated task, although according to a previous study,[22] 500 K was assumed to be the maximum (in the sense of neutral resident time) and 900 K to be the minimum.

3.2.4.2 Range of Bohm diffusion coefficient

The perpendicular component of the classical diffusion coefficient scales with $1/B^2$, and is given as:

$$D_{\perp} = \frac{1}{1 + \omega_c^2/\nu^2} \frac{k_B T_e}{m\nu} \tag{3.2}$$

where ω_c is the electron plasma frequency, ν is collision frequency, k_B is the Boltzmann constant, T_e is the temperature, and m is the electron mass. In E×B devices like Hall thrusters, the electron cross-field transport is known to be much greater than what is predicted by the classic diffusion theory. This anomalously enhanced electron transport was first observed by David J. Bohm in 1949, who suggested an empirical coefficient, known as the Bohm coefficient, to account for this anomalous transport.[23] Although almost seven decades have passed since its first observation, there does not yet exist a conclusive physical model to be used in numerical simulations. Hence, it is a common practice in Hall thruster simulation that the coefficient of 1/16 suggested by Bohm is used as:

$$D_B = \frac{1}{16} \frac{k_B T_e}{eB} \tag{3.3}$$

where D_B is the diffusion coefficient, B is the magnetic field strength, and e is the unit charge. However, it should be noted that this empirical coefficient of 1/16 is not necessarily applicable for different thruster configurations and operation conditions, thus a sensitivity analysis was conducted. The coefficient of 1/8 was assumed to be the maximum, and naturally, elimination of the Bohm diffusion model (e.g., coefficient of zero) was selected to be the minimum.

3.2.4.3 Range of cathode coupling voltage

The voltage utilization efficiency is defined as the ratio of beam voltage to discharge voltage, $\eta_V = V_b/V_d$. As for the beam voltage, it is defined as $V_b = V_d - V_c$, where V_c is the cathode coupling voltage. Large cathode coupling voltage is undesirable since it decreases the available potential energy that ions convert into kinetic energy, and thus generate thrust. Cathode coupling voltage in a Hall thruster is usually around 10-30 V. To quantify its effect, a maximum V_c of 30 V was assumed according to the measurement results of thrusters operating under similar conditions,[17] and the anode potential applied was simply reduced by V_c.

3.2.4.4 Range of electron injection current

In the fully kinetic code, electrons are injected through plume boundary cells (see Fig. 3.1 b) to sustain the discharge. Note that this electron injection current was not equal to the cathode electron emission current because the cathode was located outside the computational domain. Therefore, the beam neutralization process took place outside the computational domain. Thus, the net electron injection current plus the beam current must equal the discharge current. Since it is nontrivial to know the net electron injection current beforehand, we injected a presumed number of electrons and let the excessive electrons eject from the domain simultaneously. The nominal value of the electron injection current was 2 A, which is equal to double the equivalent xenon propellant current. To quantify its effect, 1 A and 3 A were selected as the lower and upper bounds.

3.2.4.5 Range of background pressure

Many studies in literature[18, 19] conclude that the vacuum chamber background pressure has a remarkable influence on Hall thruster plasma properties and performance parameters, especially for high power applications.[24] Thus, it is necessary to correct the experimental results to predict a thruster's in-space performance. The background pressure effect may be considered an experimental measurement error since it increases thrust and efficiency. During the experiments using the UT-62 thruster, the background pressure was kept lower than 3.7×10^{-3} Pa (~2.8×10^{-5} Torr) against a 1.36 mg/s (+ 0.27 mg/s cathode) xenon mass flow rate.[13] This pressure was gauged at a point far away from the thruster exit, so it may be assumed that the pressure near the thruster exit plume region is much higher. Therefore, the background pressure upper bound was chosen as 6.7×10^{-3} Pa (5×10^{-5} Torr).

3.2.5 Verification of statistical error

3.2.5.1 Macroparticle number

PIC simulations are subject to statistical or "discrete particle" noise. This non-physical effect is related to collisions, and it gives rise to noise-induced particle diffusion.[3, 25] This numerical heating of the plasma due to statistical noise is proportional to the number of macroparticles per cell, which is proportional to the grid space. Therefore, attention must be paid to convergence with macroparticle size prior to any sensitivity analysis of the physical parameters. Acordingly, the macroparticle size convergence of the simulation was studied. The thruster simulated was the UT-62, and the simulation conditions were the same as listed in Table 3.1 and the "Nominal" physical parameters of Table 3.2. It is to be noted that the ideal condition is for the macroparticle size to equal to one, which means one simulation particle represents one real particle.

Figure 3.3 presents the inverse average electron macroparticle number against the simulated discharge current. It should be noted that the simulated discharge current has a

linear relationship with the number of particles per grid. The parallel decrease in discharge current and macroparticle size is because of the noise-induced particle diffusion. This result suggests that the simulation result converges almost linearly; therefore, the size of $1x10^7$ was selected as a good trade-off between the numerical error and the computational cost for this specific thruster. Note that the discharge current extrapolated to macroparticle size equals one does not match the measurement result perfectly, which is natural because various measurement and model uncertainties in physical parameters are yet to be accounted for.

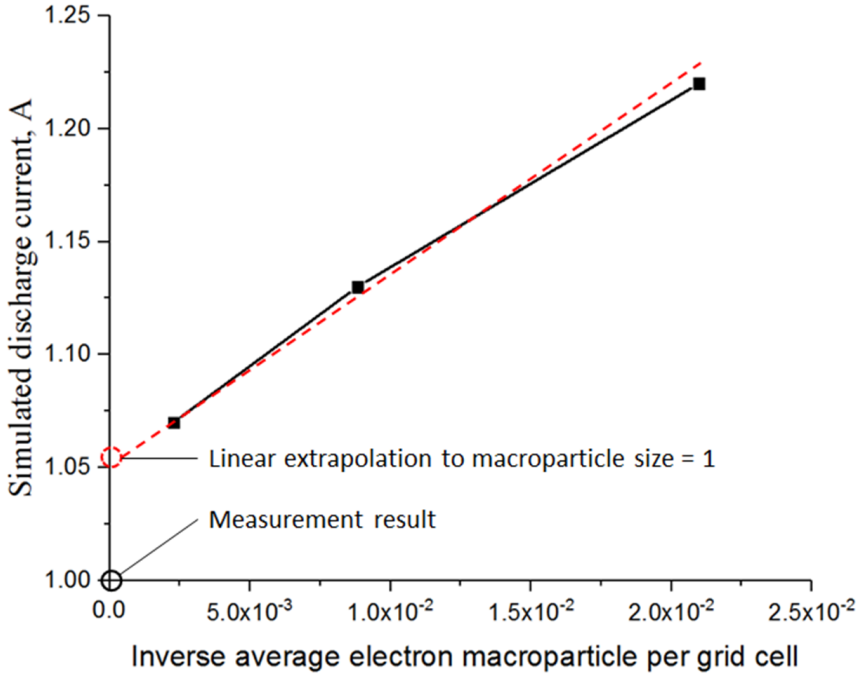

Figure 3.3 Convergence of discharge current against electron macroparticle size for UT-62 Hall thruster. *The linear fit shows the result extrapolated to the ideal condition of size = 1.*

3.2.5.2 Grid spacing

The effect of grid spacing on the discharge plasma and wall sheath structure was investigated by Cho et al. [13] It was concluded that a grid spacing of 0.2 mm is sufficient to accurately capture the sheath potential drop. Some additional simulations were conducted to examine the effect of grid size on the simulation results, which is shown by Table 3.3. Furthermore, the effect of thermal accommodation coefficient, anode and wall temperatures (Case A) was also simulated on a smaller grid spacing of 0.1 mm along with the nominal grid spacing (0.2 mm). It can be seen in Table 3.3 that, for both of the grid spacings,

discharge current, thrust, and wall erosion rate are considerably affected by the change in thermal accommodation coefficient, and anode/wall temperature. This result means that the effect observed in thruster performance is not caused simply by the choice of grid size. Even though the grid spacing selected is larger than the Debye length causing uncertainty to the sheath modeling, it seems to have a minor impact on the sensitivity analysis.

Table 3.3 Effect of thermal accommodation coefficient, anode and wall temperatures on smaller grid spacing for UT-62 Hall thruster.

Grid spacing	Case A	F [mN]	I_d [A]	Max Erosion rate [mm/kh]
0.1 mm	Nom	18.4	1.2	21.5
	Min	17.2	1.1	19.1
	Max	19.3	1.3	24.7
0.2 mm	Nom	15.7	1.1	20.7
	Min	14.6	1.0	16.7
	Max	17.0	1.2	22.7

3.2.6 Thrust performance results and discussion

Figure 3.4 summarizes the results of the one-factor-at-a-time sensitivity analysis for thrust and discharge current and compares them to experimental results. It should be noted that a water-cooling system was used for ground testing of the UT-62; however, the experimental results were not evaluated under thermal equilibrium conditions, but measured under cold-start conditions. It was observed that the sensitivity of A, neutral flow (thermal accommodation coefficient and anode/wall temperatures), and B, Bohm diffusion coefficient, were by far the most influential. It was found that the uncertainties in physical parameters arising from the neutral flow (thermal accommodating coefficient and anode/wall temperatures) were just as influential as the Bohm diffusion coefficient. This was one of the most important findings of this study because less attention has been paid to them so far. This suggests that improving (narrowing) the confidence range of uncertainties in physical parameters related to neutral flow will be as beneficial as that of the Bohm diffusion model for the accuracy of fully kinetic simulation.

The rest of this section presents the details of the top three influential physical parameters: parameters related to neutral flow, Bohm diffusion coefficient, and background pressure.

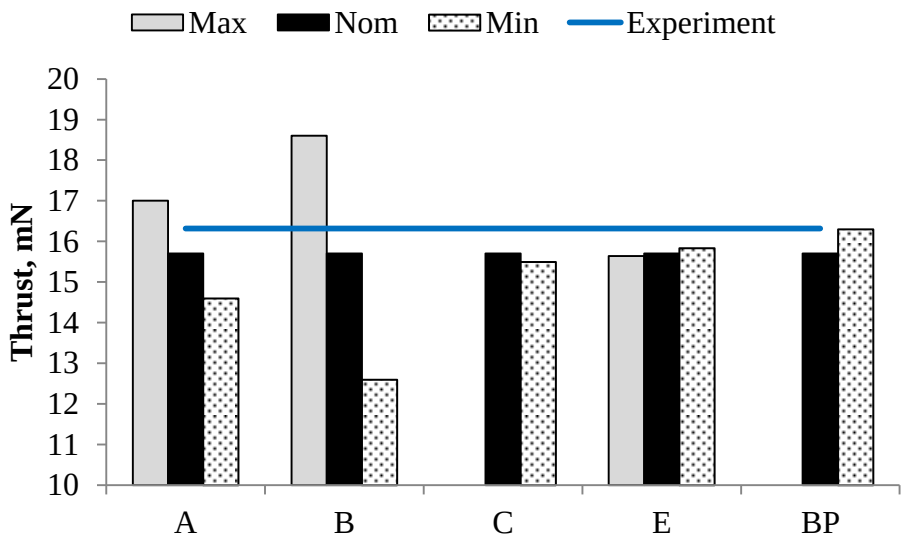

(a) Thrust

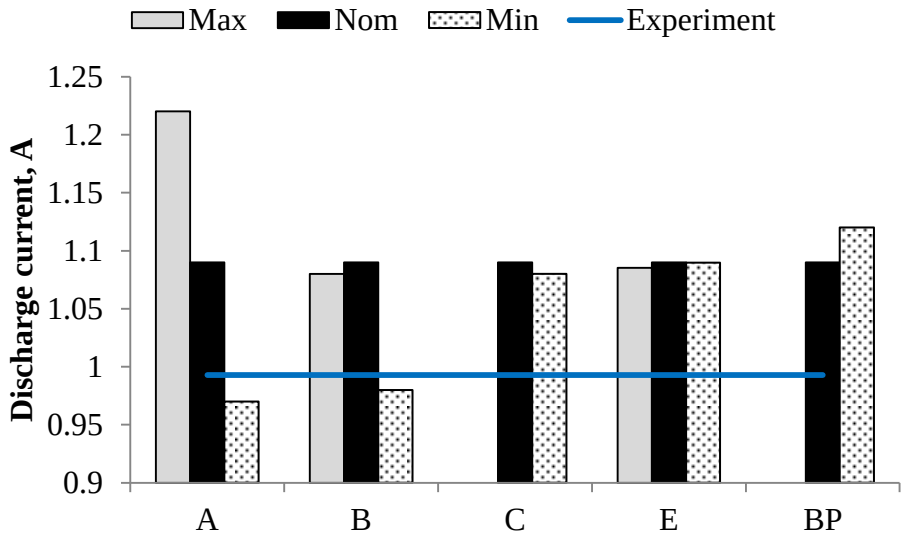

(b) Discharge current

Figure 3.4 Summary of the one-at-a-time sensitivity analysis results of UT-62 Hall thruster for thrust and discharge current. *Note the "nom" nominal condition is displaying the same result for all cases.*

3.2.6.1. Effect of thermal accommodation coefficient, anode and wall temperatures

Table 3.4 shows the detailed results of the sensitivity analysis for A, B, and BP physical parameters. The symbol "nom" represents the nominal case, while A_{max}, A_{min} are respectively the maximum and minimum cases. It can be seen from Table 3.4 that any change in thermal accommodation coefficient and temperature mostly affects the ionization process, represented by propellant efficiency Φ_P. This was caused by the increase in propellant residence time in the discharge channel due to the slower flow speed of unionized propellant, the origination of which is increase in thermal accommodation coefficient and lower wall temperature. The discharge current and ion beam current increase monotonically from the minimum case to the maximum case; whereas the unionized neutral propellant current I_n decreases. The plasma properties illustrated by Fig. 3.5 support this understanding in that the plasma density of the maximum case (A_{max}) was much higher than that of the minimum case (A_{min}).

Table 3.4 Simulation results of UT-62 Hall thruster for A, B, and BP.

	Case	Nom	A		B		BP
			Min	Max	Min	Max	Max
Sensitivity (input) parameters	T_{co}	0.9	0.5	1.0	0.9	0.9	0.9
	E_{co}	0.9	0.5	1.0	0.9	0.9	0.9
	T_{anode}[K]	500	900	500	500	500	500
	T_{wall}[K]	700	900	500	700	700	700
	Bohm	1/16	1/16	1/16	0	1/8	1/16
	Bp[Pa]	0	0	0	0	0	6.7×10^{-3}
Output parameters (numerical simulation results)	F[mN]	15.7	14.6	17.0	18.6	12.6	16.3
	I_d[A]	1.09	0.97	1.22	0.98	1.08	1.12
	I_{b1}[A]	0.78	0.69	0.87	0.78	0.74	0.80
	I_{b2}[A]	0.11	0.10	0.12	0.10	0.10	0.11
	I_n[A]	0.17	0.26	0.07	0.16	0.21	0.22
	Δ	0.03	0.04	0.02	0.04	0.07	0.02
	η_t[%]	27.9	27.0	29.0	43.5	17.9	29.2
	η_E[%]	60	56	61	64	60	59
	η_u[%]	83	74	93	84	79	85
	η_a[%]	56	65	51	81	38	58

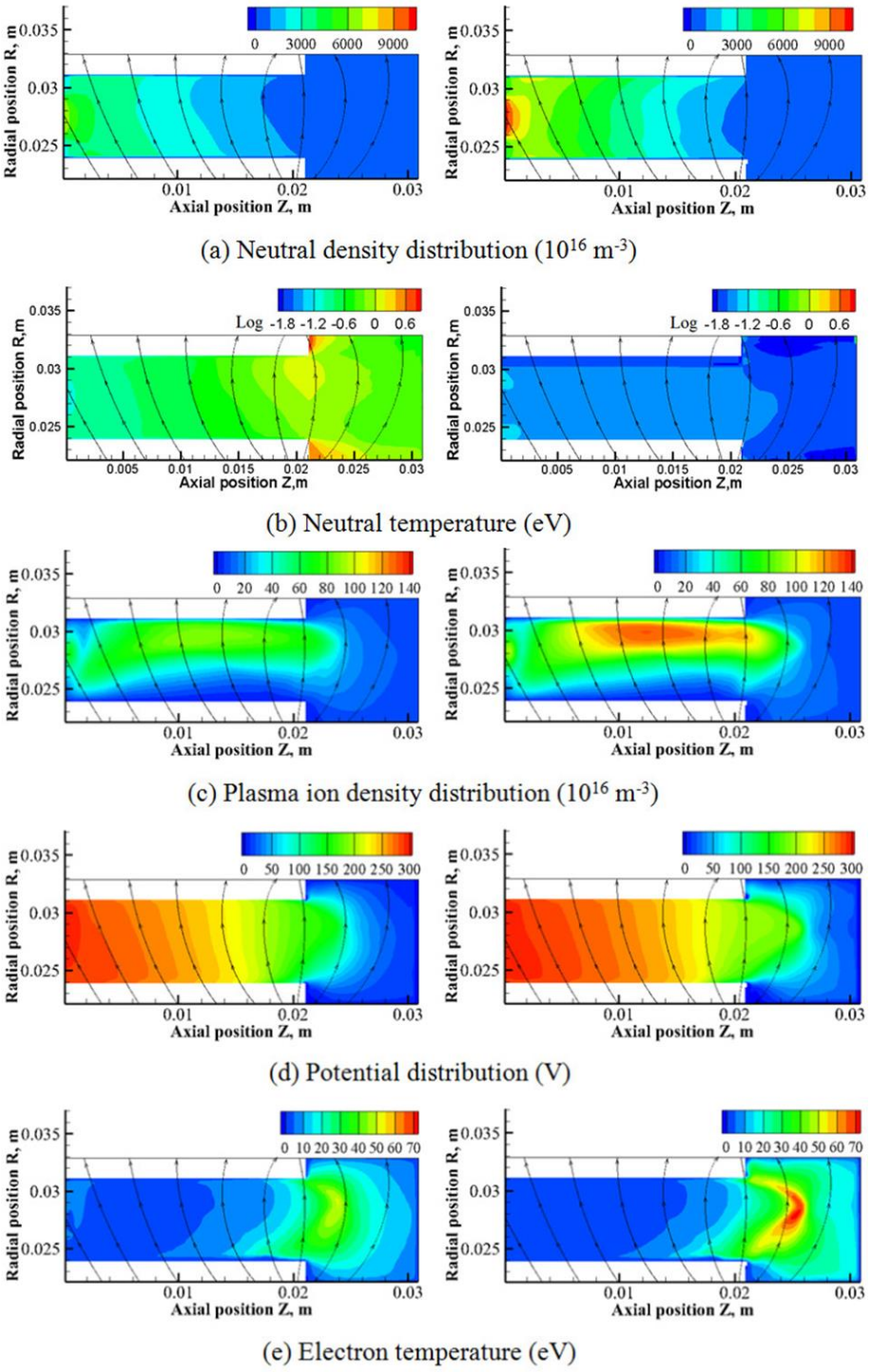

Figure 3.5 Simulated plasma properties of UT-62 Hall thruster for the accommodation coefficient & anode/wall temperature (A_{max} and A_{min}). *Plots on the left belong to A_{min} case. Plots on the right belong to A_{max} case. Lines with arrows represent the applied magnetic field.*

Notice that the ion density distribution is not uniform in the radial direction. We believe that the concentration of ion density in the vicinity of outer channel was caused by the shape of the magnetic field lines, which generated equipotential lines slanted towards the outer outer wall as compared to the inner wall. As a result, ions are accelerated from the bulk plasma toward the outer wall where they become neutral after recombination, and increase neutral density, electron-neutral collision frequency, and thus ion/electron density near the outer wall. This may also explain why the neutral temperature difference between A_{max} and A_{min} is two orders of magnitude large. It is worth mentioning that not only the propellant utilization, but also the beam efficiency (η_a in Table 3.5) and the shape of the equipotential lines (Fig. 3.5 d) changed slightly. This was considered to be caused due to the change in electron cross-field transport; namely, the higher electron temperature and density of the maximum case leading to an increase in electron diffusion and diffusive plasma distribution. In addition, it should be noted that the electron temperature is controlled by the electron-neutral collisions since these collisions are the primary contributor to electron energy loss. The enhanced electron temperature in the maximum case (A_{max}) is because the neutral density, and thus electron energy loss due collisions, outside the channel was reduced in contrast to that inside the channel.

3.2.6.2. Effect of Bohm diffusion coefficient

The differences in plasma properties are presented in Fig. 3.6. This time, the beam efficiency η_a was the efficiency most influenced. From Table 3.4, it was found that thruster performance deteriorated as the Bohm coefficient increased, and thus, cross-field electron transport increased due to the increasingly diverse beam. The electron current (discharge current minus total beam current) also monotonically increased from the minimum case (B_{min}) to the maximum case (B_{max}), which was apparently caused by the increased electron transport.

Unlike the A parameter cases, the major differences were found to be the shape of the equipotential lines and electron temperature. Obviously, these changes were caused by the change in electron cross-field transport due to the artificially increased/decreased diffusion due to the Bohm diffusion model.

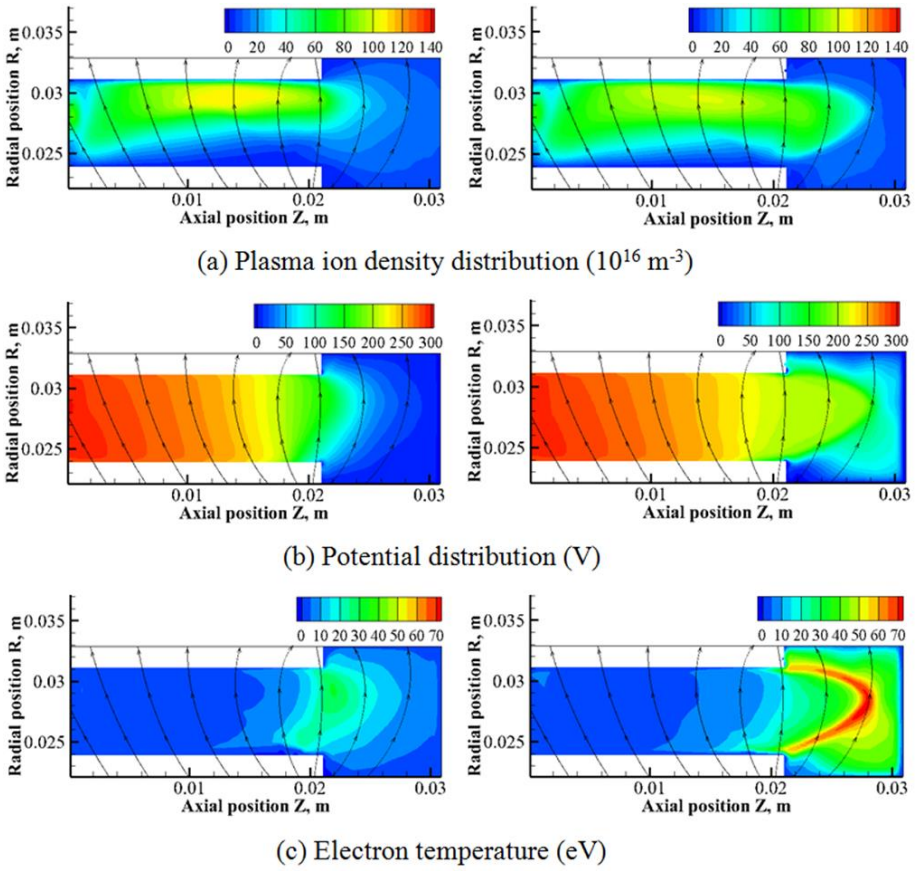

Figure 3.6 Simulated plasma properties of UT-62 Hall thruster for the Bohm diffusion coefficient (B_{max} and B_{min}). *Plots on the left belong to B_{min} case. Plots on the right belong to B_{max} case.*

3.2.6.3. Background pressure effect

To set various background pressures inside the channel, the background pressure was controlled by a neutral xenon flow rate from the plume boundary cells as shown in Fig 1. The background pressure at the plume boundary was assumed to be spatially uniform, and the amount of the background neutral injection was determined to be equal to the difference between the presumed background pressure and the pressure of the plume boundary cells. Thus, no background neutrals were injected into a cell when the pressure in that cell was higher than the presumed background pressure. The background neutrals were assumed to be thermalized to the vacuum chamber wall temperature of 300 K.

Figure 3.7 shows the simulation results of thrust and anode efficiency under different background pressure conditions. The existence of background pressure artificially increased the thrust and anode efficiency as reported in a previous study.[24] It was also observed that

the simulated thrust and efficiency come close to the results measured, when the background pressure increases, which might explain the discrepancies between the simulation and experiment.

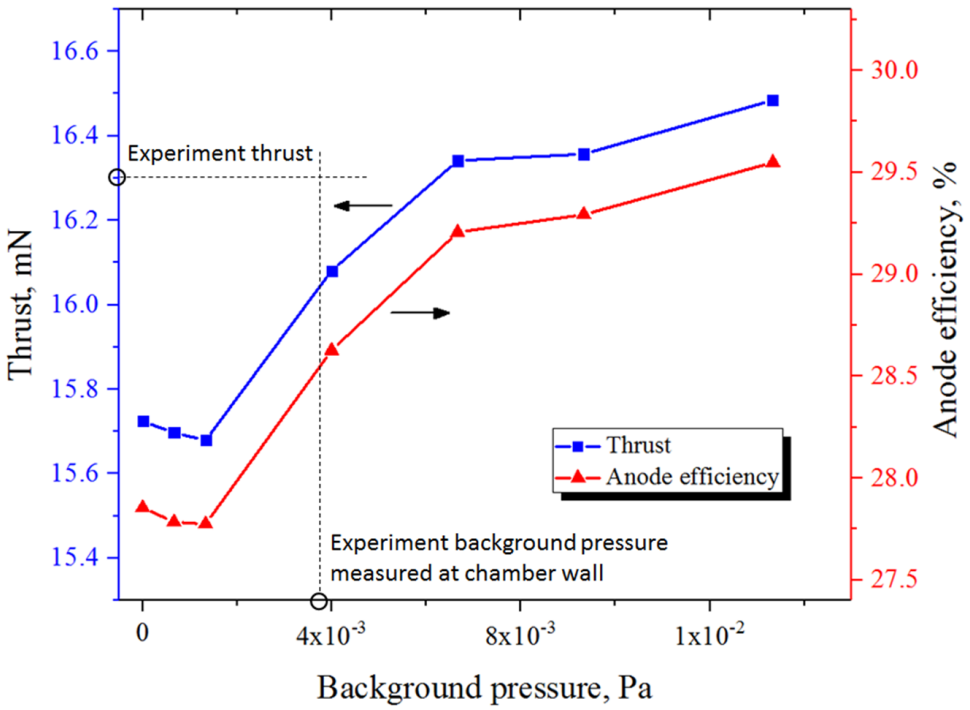

Figure 3.7 Simulated thrust and anode efficiency of UT-62 Hall thruster under different background pressure conditions.

The breakdown of the efficiency in Table 3.4 shows that the background pressure artificially increases the thrust efficiency by increasing propellant efficiency as a result of injecting background neutrals. It also shows that the background pressure not only increases the thrust, but also the discharge current, which means it has a relatively small impact on the thrust-to-power ratio compared to the specific impulse.

It is to be noted that there was no change in the thruster performance for background pressures presumed lower than 1.33×10^{-3} Pa, which means the pressure of the plume boundary cells cannot be lower than 1.33×10^{-3} Pa due to the unionized neutrals escaping from the thruster.

3.2.7 Channel wall erosion results and discussion

Lifetime is another critically important performance consideration for Hall thrusters. Usually, the lifetime of a Hall thruster is determined by the erosion rate of the discharge channel walls, which is caused by sputtering due to the high-energy ion bombardment. Figure 3.8 summarizes the simulated wall erosion rate results calculated according to the wall-incident ion flux and energy. The channel wall material (boron nitride, BN) threshold energy of ion sputtering was assumed to be 35 electron volts, and the Yamamura model was used to approximate the sputtering yield.[26] Since the wall erosion rates were not uniformly distributed throughout the channel, only the maximum rate was shown as the bottleneck of the thruster lifetime.

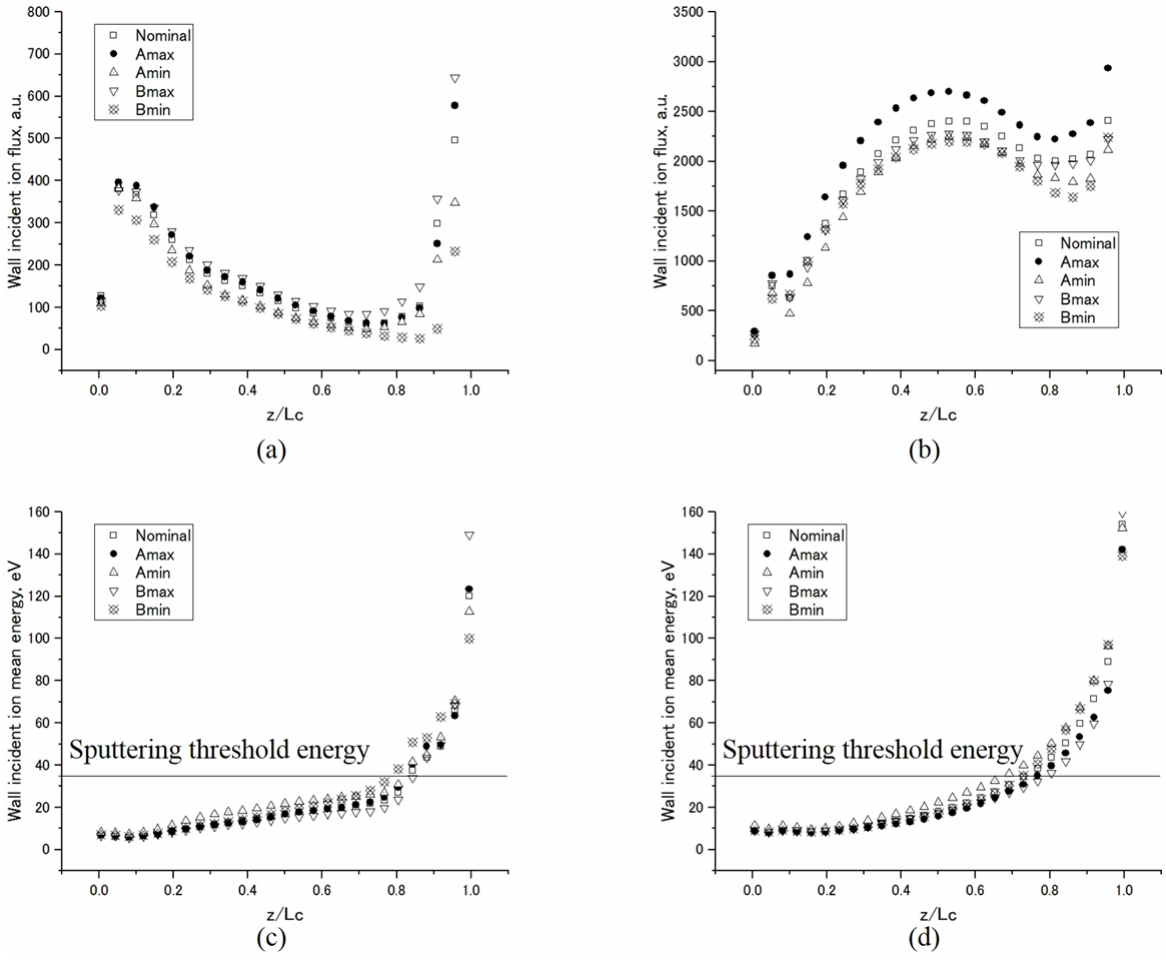

Figure 3.8 Simulated wall-incident ion properties distribution of UT-62 Hall thruster. *(a): Inner-wall incident ion flux, (b): Outer-wall incident ion flux, (c): Inner-wall incident ion mean energy, and (d) Outer-wall incident ion mean energy.*

The results indicate that the thruster lifetime is more sensitive to the physical parameters than the discharge current or thrust. The influential parameters are the ones related to neutral flow and the Bohm diffusion coefficient; however, the impact of cathode-coupling voltage loss became nontrivial in contrast to its impact on the thrust efficiency. To elucidate the cause of the wall erosion, the wall-incident ion properties of nominal, parameter A, and parameter B cases are shown by Fig. 3.9. For all of the cases and the inner-channel and outer-channel, the peak of the wall erosion rate placed at the channel exit (not shown) having the highest ion flux and energy. On the contrary, the upstream channel was essentially erosion-free because the incident ion energy was lower than the BN sputtering threshold energy. According to the comparison between the five cases listed, it was found that both ion flux and energy contribute to the change in channel wall erosion rate. Although the discrepancy of the ion flux was larger than that of the ion energy, the difference in ion energy was also important because of the non-linearity of the sputtering rate near the threshold.

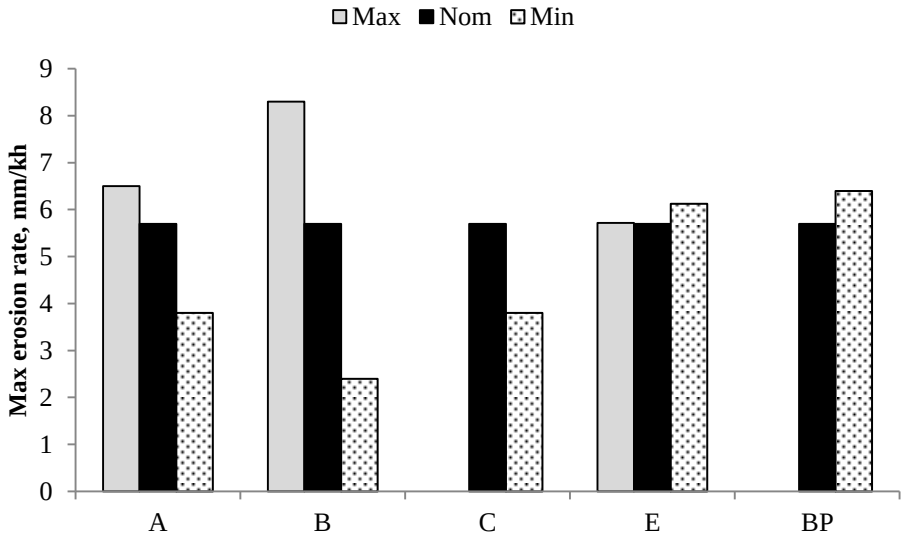

(a) Inner wall

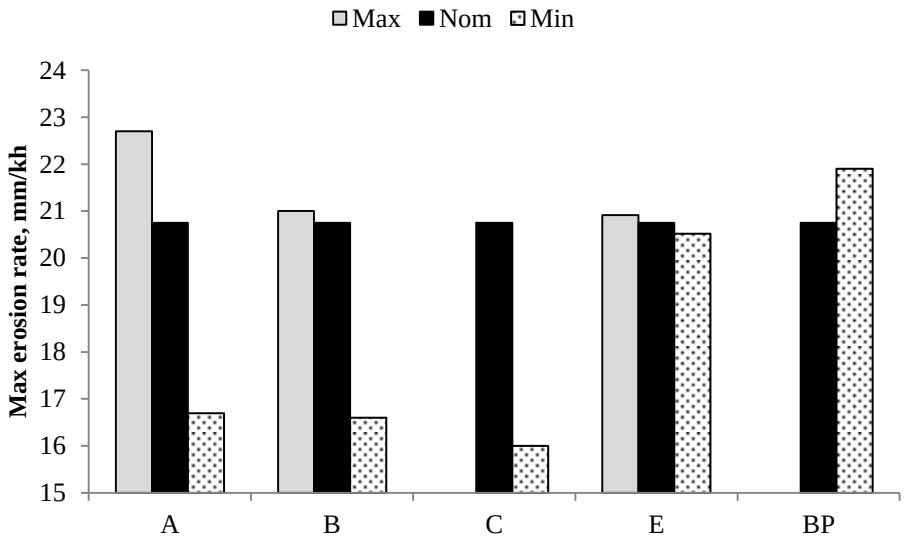

(b) Outer wall

Figure 3.9 Summary of the one-at-a-time sensitivity analysis results of UT-62 Hall thruster for the maximum channel-wall erosion rate.

3.3 Simulation of External Discharge Plasma Thruster

3.3.1 Computational domain

The fully kinetic code was modified to satisfy boundary conditions of the XPT. Figure 3.10 summarizes the boundary conditions for the semi implicit field solver and all kinds of particles. Neutral particles and ions are thermalized on the front wall surface with the pre-determined accommodation coefficients. Charge accumulation on the front wall was taken into consideration when calculating the electric field. Secondary electrons were emitted according to $\delta = \sqrt{(T_e/35)}$, where δ is emission yield and T_e is electron temperature. The ion-beam neutralization process is not directly simulated as the cathode is located outside the computation domain. Instead electrons with initial energy of 2 eV are injected from the plume boundary cells to keep local quasi-neutrality. The front wall is expressed by the difference of electric permittivity and the boundary conditions for particles. Neumann condition ($\partial\phi/\partial n = 0$) was imposed at the front wall and thruster centerline. Dirichlet condition was imposed at the anode surface ($\phi = \phi_a$) and free space ($\phi = 0$ V). Those particles entering the boundary cells along the thruster centerline are reflected back into the computation domain. Figure 3.11 shows a schematic of the computational domain and magnetic field lines.

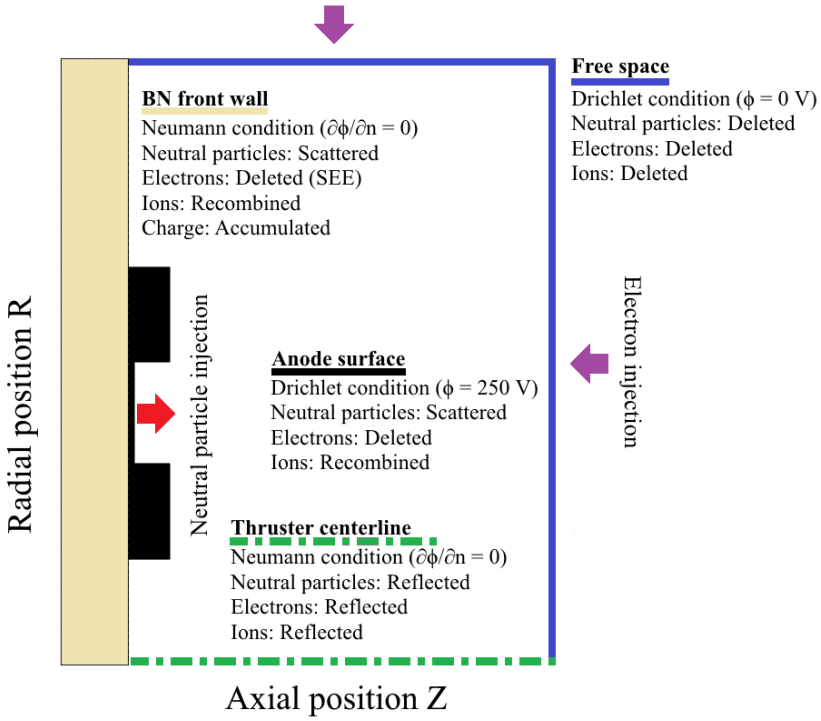

Figure 3.10 Boundary conditions of the XPT for field solver and particles.

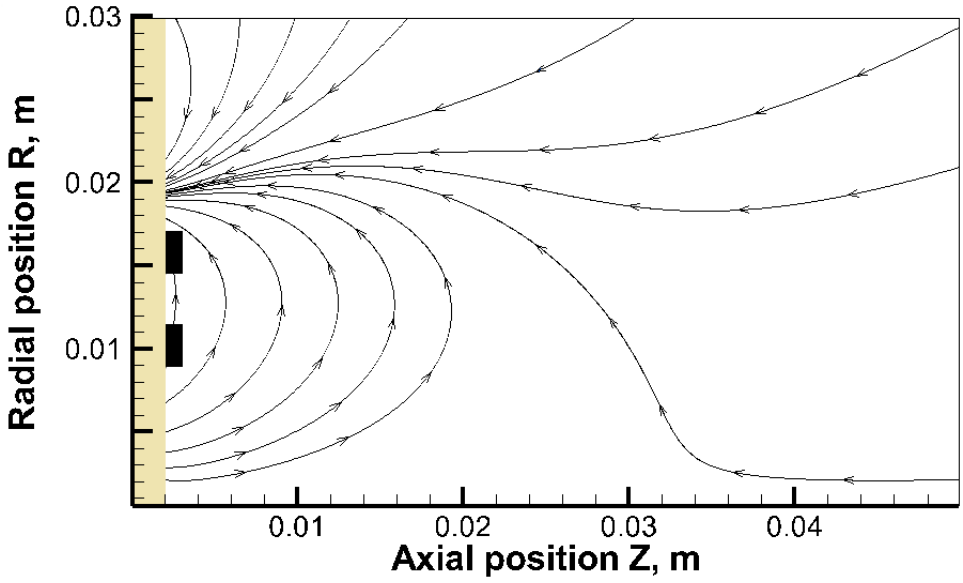

Figure 3.11 Schematic of computational domain of the XPT. *Lines with arrows represent the magnetic field lines.*

3.3.2 Simulation conditions

The one-factor-at-a-time sensitivity analysis method presented in Chapter 3.2 was repeated for the XPT at 250 V anode potential and 0.95 mg/s mass flow rate operating condition to determine a range to errors due to physical uncertainties. Simulations for each case were run for 0.5 million steps. All of the performance results and plasma distribution plots were time-averaged over 0.2 ms samplings every 100 simulation steps. Table 3.5 summarizes numerical settings. The fully kinetic code employs artificial electron mass to accelerate the computation and it manipulates code input and plasma parameters to recover the real physics. The convergence of the simulation was judged by the time-history of the total number of simulation particles. The efficiency analysis scheme of Brown[14] was used to investigate the details of thruster performance (see Appendix).

Table 3.5 Numerical settings for the XPT.

Discharge voltage [V]	250
Xe mass flow rate [mg/s]	0.95
Code	2D3V fully kinetic PIC/ DSMC
Field solver	Semi implicit
Cell network	Uniform rectangular
Particle mover	4^{th} order Runge Kutta
Time step [s]	$4x10^{-10}$
Grid spacing [mm]	0.2
Macroparticle size	$1x10^{7}$
Artificial mass ratio	Electron mass multiplied by $f^2 = 2500$
Magnetic field correction for electron	$f_B = f^{2/3} = 13.6$
Bohm diffusion model	Spatially uniform virtual scattering
Particles	e^-, X_e , X_e^+ and X_e^{++}
Collisions	e^--X_e elastic scattering e^--X_e excitation e^--X_e ionization e^--X_e^+ ionization Coulomb collisions

3.3.3 Investigated model uncertainties

The thermal accommodation coefficient of heavy particles, Bohm diffusion coefficient, cathode coupling potential drop, electron injection current to the computational domain and background pressure effect were investigated. The anode temperature was assumed to be about 700 K, and it was considered to be in thermal equilibrium with the front wall as they are in close contact with each other. Table 3.6 lists the physical parameters investigated in this study and their presumed nominal, maximum and minimum values.

Table 3.6 Investigated model uncertainties for the XPT. TAC: Thermal accommodation coefficient, B: Bohm diffusion coefficient, C: Cathode coupling voltage, E: Electron injection current, and BP: Background pressure effect.

Parameter		Minimum	Nominal	Maximum
	TAC	0.5	0.9	1.0
A	T_{anode} [K]	-	700	-
	T_{wall} [K]	-	700	-
B		0	1/16	1/8
C [V]		0	0	30
E [Aeq]		1	2	3
BP [Torr]		-	0	5×10^{-5}

3.3.4 Results and discussion

3.3.4.1 Thrust performance

Figure 3.12 summarizes the results of the one-factor-at-a-time sensitivity analysis for thrust and discharge current and compares them to experimental results. At a glance, it was shown that the uncertainty of cathode coupling and Bohm diffusion coefficient were by far the most influential. We observed that plasma discharge disappears when Bohm diffusion coefficient is turned off (Bohm Min case). Simulation results for higher mass flow rate case (1.43 mg/s) were not given here; however, plasma discharge was sustainable even without Bohm diffusion. Please recall that the sensitivity of neutral flow (thermal accommodation coefficient and anode/wall temperatures) was just as influential as the Bohm diffusion coefficient in the case of UT-62 Hall thruster. The effect of thermal accommodating coefficient was found to be insignificant for the XPT. This is expected because there are only very short anode cavity walls for neutral particles or ions to exchange thermal energy. Electron injection current also has quite small effect. Table 3.7 shows the detailed results of the sensitivity analysis for top three influential physical parameters: parameters related to Bohm diffusion coefficient, cathode coupling voltage and background pressure.

The systematic one-at-a-time sensitivity analysis results show a thrust of 8.7 mN with an error range of -26%+4%, and a discharge current of 0.48 A with an error range of +26%-24% relative to the model parameter uncertainties. Efficiency analysis shows that thruster performance deteriorates with higher Bohm diffusion mainly because of increased discharge current and doubly-charged ion current. Thrust and anode efficiency decreases with cathode coupling voltage due to energy efficiency and propellant utilization efficiency. Boosted mean neutral velocities due to the background particles entering the thruster exit may reduce plume divergence.

The XPT achieves a propellant utilization efficiency of 66% and beam efficiency of 74% for the nominal input parameters. It is remarkable that even though there is not any non-anodic cavity to confine the neutrals, the thruster succeed in obtaining moderate propellant utilization efficiency and high beam efficiency.

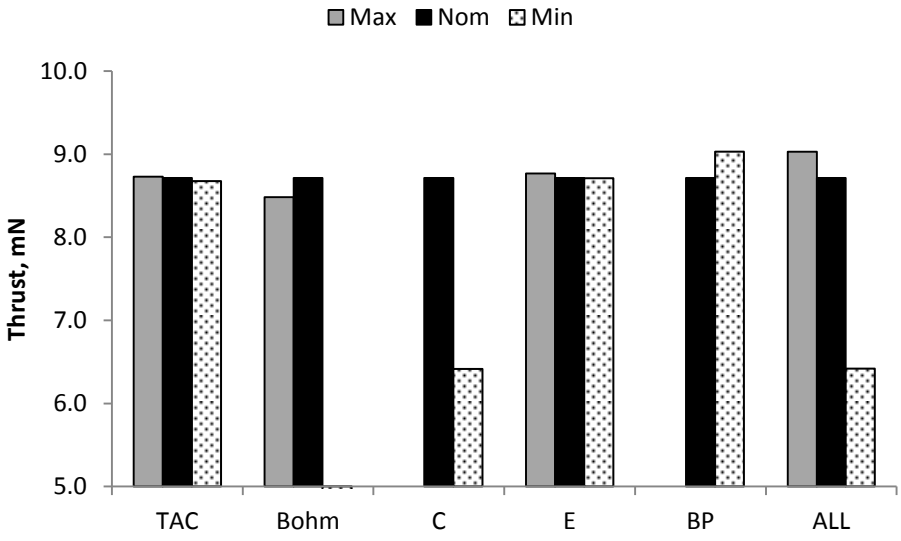

(a) Thrust

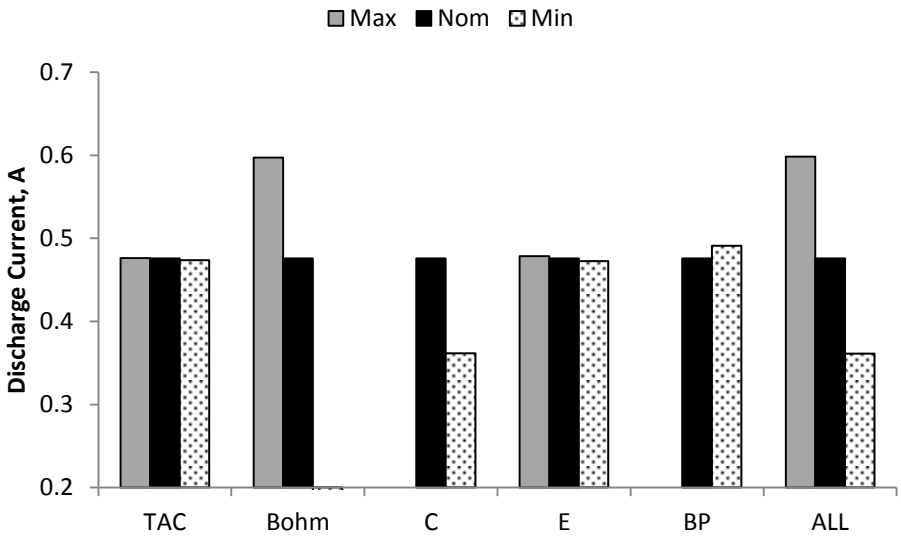

(b) Discharge current

Figure 3.12 Summary of the one-at-a-time sensitivity analysis results of the XPT for thrust and discharge current. *Note the "nom" nominal condition is displaying the same result for all cases.*

Table 3.7 Simulation input and output parameters of the XPT for the Bohm diffusion, cathode coupling, and the background pressure physical uncertainties.

	Case	Nominal	Bohm		C	BP
			Min	Max	Max	Max
Sensitivity (input) parameters	Bohm	1/16	0	1/8	1/16	1/16
	V_c[V]	0	0	0	30	0
	Bp[Torr]	0	0	0	0	$5x10^{-5}$
Output parameters (numerical simulation results)	F[mN]	8.7	Plasma disappears	8.5	6.4	9.0
	I_d[A]	0.48		0.60	0.36	0.49
	I_{b1}[A]	0.43		0.49	0.34	0.45
	I_{b2}[A]	0.04		0.10	0.02	0.04
	I_n[A]	0.24		0.17	0.36	0.30
	η_t[%]	33.6		25.0	23.5	34.9
	η_E[%]	69		58	61	69
	η_u[%]	66		76	51	62
	η_a[%]	74		57	76	81

3.3.4.2 Plasma properties

Figure 3.13 shows 2D plots of neutral number density, ion number density, plasma potential, and electron temperature for the nominal and Bohm max cases. Plasma potential has its maximum value at the anode then decreases gradually. Equipotential lines follow the magnetic field lines more closely at the anode centerline. Hot electrons are more concentrated towards the outer edges of the anode wall at the exit, which increases energy lost to the anode walls.

Increasing Bohm diffusion coefficient shows a similar trend to the results UT-62 Hall thruster. Electron temperature increases as a result of increased electron conductivity/ transport, and equipotential lines move downstream. Ions are generated in a wider region both inside and outside the anode slot causing a more diffuse plasma distribution, and thus less plume divergence efficiency. Unlike the case of UT-62, the unionized neutral propellant decreases with increasing Bohm diffusion coefficient, which may be related to the higher neutral number density in the ionization region.

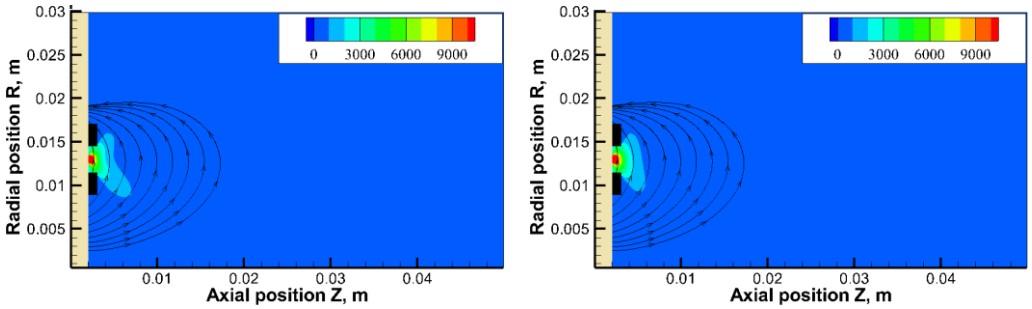

(a) Neutral density distribution (10^{16} m^{-3})

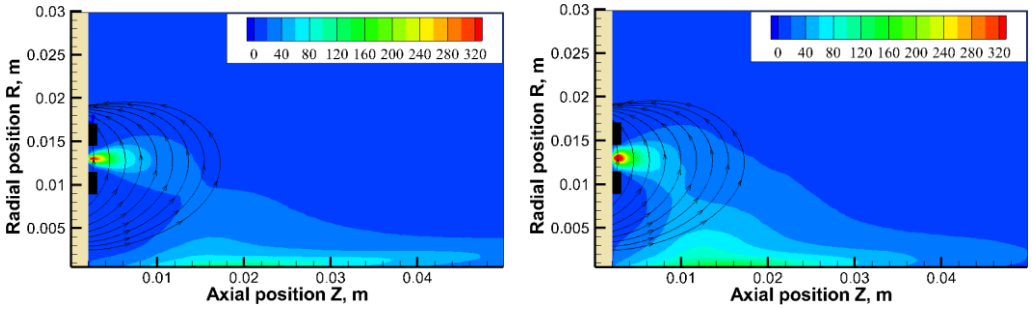

(b) Plasma ion density distribution (10^{16} m^{-3})

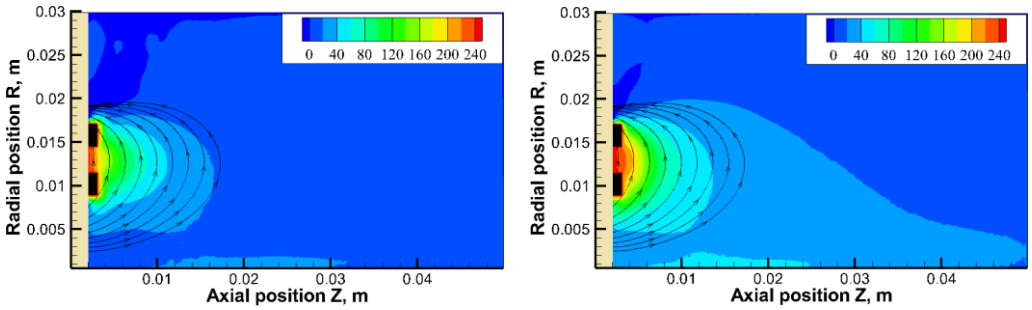

(c) Potential distribution (V)

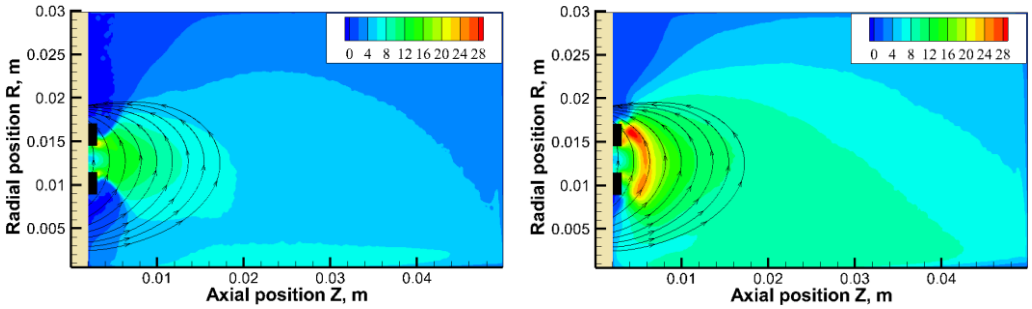

(d) Electron temperature (eV)

Figure 3.13 Simulated plasma properties of the XPT for 250 V - 0.95 mg/s. *Plots on the left belong to nominal case. Plots on the right belong to Bohm max case.*

3.4. Summary

The first and second paragraphs summarize the results for UT-62 Hall thruster. A sensitivity analysis of a fully kinetic particle-in-cell (PIC) code was conducted to evaluate the importance of the uncertainties associated with physical parameters for better predicting the accuracy of Hall thruster simulation. Fully kinetic code physical parameters (thermal accommodation coefficient, anode/wall temperatures, Bohm diffusion coefficient, electron injection current, cathode coupling voltage, and background pressure) were investigated. The impact of each physical parameter on thrust efficiency and wall erosion rate was quantified one-by-one over a presumed possible range. The simulation was conducted for a laboratory model magnetic-layer Hall thruster.

The uncertainties in the physical parameters reasonably account for the discrepancies between the measured and simulated results. Furthermore, the results indicate that the model parameters have a more severe impact on wall erosion than thrust efficiency. Among the sources of uncertainties, the Bohm diffusion coefficient and uncertainties related to the neutral flow (thermal accommodation coefficient and anode/wall temperatures) were by far the most influential for both thrust efficiency and wall erosion; whereas the impact of other uncertainties including electron injection current, cathode coupling voltage, and background pressure was minor. It was found that uncertainties in physical parameters related to the neutral flow has a comparable influence to that of Bohm diffusion, which suggests that accurately identifying not only the Bohm diffusion coefficient, but also the thermal accommodation coefficient and anode/wall temperatures is essential for better predictive modeling of Hall thrusters.

The external discharge plasma thruster (XPT) was also simulated through the fully kinetic code, and the sensitivity analysis methodology was applied to determine upper and lower bounds for estimated thrust performance. Numerical investigation suggested that the XPT can be as much efficient as conventional Hall thrusters of the same power range. This result urged us to manufacture the thruster, and perform experimental investigation, which is covered in the next chapter.

References

[1] Zhurin, V. V., Kaufman, H. R., and Robinson R. S.: Physics of Closed Drift thrusters, *Plasma Sources Science and Technology*, Vol. 8, No. 1, Feb., 1999, pp.R1-R20.

[2] Komurasaki, K., and Arakawa, Y.: Two-dimensional numerical model of plasma flow in a Hall thruster, Journal of Propulsion and Power, Vol. 11, No. 6, 1995, pp. 1317 – 1323.

[3] Szabo, J. J.: Fully Kinetic Numerical Modeling of a Plasma Thruster, *PhD thesis*, Massachusetts Institute of Technology, Cambridge, 2001.

[4] Fife, J. M.: Hybrid-PIC Modeling and Electrostatic Probe Survey of Hall Thrusters, *PhD thesis*, Massachusetts Institute of Technology, 1998.

[5] Mikellides, I. G., Katz, I., Hofer, R. R., and Goebel, D. M.: Magnetic Shielding of Walls from the Unmagnetized Ion Beam in a Hall Thruster, *Applied Physics Letters*, Volume 102, Issue 2, id. 023509, 2013, 5 pages.

[6] Adam, J. C., Heron, A., and Laval, G.: Study of Stationary *Plasma* Thrusters Using Two-dimensional Fully Kinetic Simulations, *Physics* of *Plasmas*, Volume 11, Issue 1, 2004, pp. 295-305.

[7] Fife, J., Martinez-Sanchez, M., and Szabo, J.: A Numerical Study of Low-frequency Discharge Oscillations in Hall Thrusters, *Proceedings of 33rd AIAA Joint Propulsion Conference*, No. 97-3051, 1997.

[8] Parra, F. I., Ahedo, E., Fife, J. M., and Martinez-Sanchez, M.: A Two-dimensional Hybrid Model of the Hall Thruster Discharge, *Journal of Applied Physics*, Journal of Applied Physics, Volume 100, Issue 2, 2006, pp. 023304-023304-11.

[9] Watanabe, H., Nakano, M., Kajimura, Y., and Funaki, I.: Feasibility Study on Numerical Life Qualification of Ion Thruster's Ion Optics Using the JIEDI Tool, *Transactions of the Japan Society for Aeronautical and Space Sciences*, Aerospace Technology Japan, Vol. 12, No.ists29, pp.Pb_65-Pb_72, 2014.

[10] Yamamoto, N., Nakagawa, T., Komurasaki, K. and Arakawa, Y.: Discharge plasma Fluctuations in Hall Thrusters, *Vacuum*, Vol.65, Issues 3-4, 2002, pp. 375-381.

[11] Yokota, S., Komurasaki, K., and Arakawa, Y,: Plasma Density Fluctuation Inside a Hollow Anode in an Anode-layer Hall Thruster, *Proceedings of 42nd AIAA/ASME/SAE/ASEE Joint Propulsion Conference& Exhibit*, AIAA-2006-5170.

[12] Cho, S., Watanabe, H., Kubota, K., Iihara, S., Honda, K., Fuchigami, K., Uematsu, K., and Funaki, I.: Parametric Kinetic Simulation of an IHI High Specific Impulse SPT -Type Hall Thruster, *Proceedings of 50th AIAA/ASME/SAE/ASEE Joint Propulsion Conference & Exhibit*, 2014-3426.

[13] Cho, S., Komurasaki, K., and Arakawa, Y.: Kinetic Particle Simulation of Discharge and Wall Erosion of a Hall thruster, *Physics of Plasmas*, Volume 20, Issue 6, 063501, 2013.

[14] Brown, D. L.: Investigation of Low Discharge Voltage Hall Thruster Characteristics and Evaluation of Loss Mechanisms, *PhD thesis*, University of Michigan, 2009.

[15] Hofer, R. R., Katz, I., Mikellides, I. G., and Gamero-Castano, M.: Heavy Particle Velocity and Electron Mobility Modeling in Hybrid-PIC Hall Thruster Simulations, *AIAA Paper*, 2006-4658.

[16] Hofer, R. R., Katz, I., Mikellides, I. G., Goebel, D. M., Jameson, K. K., Sullivan, R. M., and Johnson, L. K.: Efficacy of Electron Mobility Models in Hybrid-PIC Hall Thruster Simulations, *AIAA Paper*, 2008-4924.

[17] Jameson, K. K., Goebel, D. M., Hofer, R. R., and Watkins, R. M.: Cathode Coupling

in Hall Thrusters, *Proceedings of 30th International Electric Propulsion Conference*, 2007-278.

[18] Randolph, T., Kim, V., Kaufman, H., Kozubsky, K., Zhurin, V., and Day, M.: Facility Effects on Stationary Plasma Thruster Testing, *Proceedings of 23rd International Electric Propulsion Conference*, IEPC-93-93 844.

[19] Kamhawi, H., Huang, W., Haag, T., and Spektor, R.: Investigation of the Effects of Facility Background Pressure on the Performance and Voltage-Current Characteristics of the High Voltage Hall Accelerator, *Proceedings of 33rd International Electric Propulsion Conference*, IEPC-2013-446.

[20] Hora, S. C.: Aleatory and Epistemic Uncertainty in Probability Elicitation with an Example from Hazardous Waste Management, *Reliability Engineering and System Safety*, Volume 54, 1996, pp. 217-223.

[21] Kim V., Semenov A., and Shkarban I.: Investigation of the Accelerated Ions Energy Accommodation Under Their Impingement with Solid Surfaces, *Proceedings of 38th AIAA/ASME/SAE/ASEE Joint Propulsion Conference & Exhibit*, 2002-4110.

[22] Karadag, B., Cho, S., and Funaki, I.: Numerical Investigation of Thermal Accommodation Coefficient and Temperature Sensitivity in a Hall Thruster, *Proceedings of Plasma Conference 2014*, 19pD2-5.

[23] Bohm, D.: The Characteristics of Electrical Discharges in Magnetic Fields, *edited by A. Guthrie and R. K. Wakerling*, McGraw-Hill, 1949, pp.77-86.

[24] Byers, D., and Dankanich, J.W.: A Review of Facility Effects on Hall Effect Thrusters, *Proceedings of 31st International Electric Propulsion Conference*, IEPC 2009-076.

[25] Hockney, R. W., and J. W. Eastwood. Computer Simulation Using Particles. Institute of Physics Publishing, Bristol and Philadelphia, 1988.

[26] Yamamura, Y., and Tawara, H.,: Energy Dependence of Ion-Induced Sputtering Yields from Monatomic Solids at Normal Incidence, *Atomic Data and Nuclear Data Tables,* Volume 62, Issue 2, March 1996, pp149–253.

Chapter 3 Appendix

A. 1 Efficiency analysis

The efficiency breakdown scheme proposed by Brown[14] was used to analyze thrust generation processes influenced by the physical parameters.[9] First of all, anode efficiency η_t, the indicator of overall energy conversion of the thruster-head, can be divided into energy efficiency η_E, propellant efficiency η_u, and beam efficiency η_a as:

$$\eta_t = \frac{F^2}{2\dot{m}P_d} = \eta_E \eta_u \eta_a \tag{A1}$$

where F is the thrust, $\dot{m}$ is anode mass flow rate, and P_d is discharge power. Energy efficiency η_E represents the ratio of energy deposited on the propellant P_{jet} to the discharge power as:

$$\eta_E = \frac{P_{jet}}{P_d} = \frac{\frac{1}{2}\dot{m}\langle\overline{v^2}\rangle_m}{V_d I_d} \tag{A2}$$

where $\langle\overline{v^2}\rangle_m$ is the mass weighted average of the square of the propellant velocity, V_d is discharge voltage, and I_d is discharge current. Propellant efficiency η_u represents the relationship between the propellant momentum and kinetic energy. It is used mainly to show the thrust loss due to the unionized propellant ejected:

$$\eta_u = \frac{\langle\overline{v}\rangle_m{}^2}{\langle\overline{v^2}\rangle_m} \tag{A3}$$

where $\langle\overline{v}\rangle_m$ is the mass weighted average velocity. Finally, beam efficiency η_a shows the thrust vector loss due to beam divergence:

$$\eta_a = \left(\frac{F}{\dot{m}\langle\overline{v}\rangle_m}\right)^2 \tag{A4}$$

All of the efficiencies were computed straight-forwardly probing the simulation particles and their variation caused by the physical parameters examined.

A. 2 Discharge current oscillation amplitude

Discharge current oscillation amplitude (Δ) is defined as:

$$\Delta = \frac{\mathrm{RMS}}{\overline{I_d}} = \frac{1}{\overline{I_d}} \sqrt{\int_0^{\tau} \frac{(I_d - \overline{I_d})^2}{\tau}}, \left(\overline{I_d} = \frac{\int_0^{\tau} I_d}{\tau} \right) \quad (A5)$$

where, RMS is the root mean square, I_d is discharge current, and τ is time. An oscillation amplitude of $\Delta<0.2$ is desirable due to power processing unit (PPU) constraints.

CHAPTER 4

Experimental Characterization

Contents

"Originality thrives in seclusion free of outside influences beating upon us to cripple the creative mind. Be alone, that is the secret of invention; be alone, that is when ideas are born."

Nikola Tesla

4.1 Experimental Setup

4.1.1 Vacuum facility and operating conditions

Experiments were conducted in Space Science Chamber of ISAS/JAXA, which is 5 meters long and 2.5 meters in diameter, and shown in Fig. 4.1. The vacuum chamber is equipped with one rotary vane pump, one turbomolecular pump and two cryogenic pumps. Maximum value of background pressure measured by a crystal ion gauge (Anelva M-336MX) located in near upper middle of the vacuum chamber was 2.5×10^{-5} Torr (corrected for xenon by a coefficient given in the gauge manual). A commercial hollow cathode (Iontech HCN-252) was mounted at a 45° angle with respect to the thruster axis with orifice of the cathode approximately 150 mm above the thruster centerline. The cathode and thruster were electrically isolated from chamber ground and allowed to float. The cathode mass flow rate (0.29 mg/s), heater current (5A, Takasago GP035-50R) and keeper current (0.3 A, Takasago GP0650-05R) were held constant during all tests. The heater power supply was not turned off once the cathode starts, which is not usually the case, because small amount of electrical current drawn by the thruster did not allow the self-heating mode.

Figure 4.1 Space Science Chamber of ISAS/JAXA.

The thruster head and the cathode were electrically isolated from vacuum chamber ground, and placed in the middle of the vacuum chamber near one end. High purity xenon (99.995 %) was fed into both the anode and the cathode through argon mass flow controllers (Horiba STEC SEC-E440) incorporating a conversion factor of 0.971. Anode mass flow rate was varied between 0.48 mg/s and 1.43 mg/s with approximately 0.48 mg/s increments. The anode potential was varied between 150 V and 250 V with 50 V increments. Before any data were taken, the thruster was allowed to outgas for a few hours, and then it was operated for about 1 hour so that thruster parts can reach thermal equilibrium.

Results reported here are for the XPT with a 2–mm-thick boron nitride wall. The wall thickness difference may be expected to alter voltage-current characteristics of the thruster due the difference in the electron conductivity.

Table 4.1 summarizes the operating conditions.

Table 4.1: Performance test matrix.

	Mass flow rate [mg/s]				**Cathode current [A]**	
Potential [V]	Anode			Cathode	Keeper	Heater
150	0.48	0.95	1.43	0.29	0.3	5
200	0.48	0.95	1.43	0.29	0.3	5
250	0.48	0.95	1.43	0.29	0.3	5

4.1.2 Thrust stand

A hanging pendulum thrust stand[1] developed at the University of Tokyo was used to measure the thrust. The stand consists of two pendulums, a gap sensor, an electromagnetic actuator, and a calibration system. Thruster is mounted on an inner pendulum, while a light-emitting diode sensor is mounted on an outer pendulum, which serves as reference. Thermal drift and vacuum chamber inclination effects are canceled out by measuring displacement between the two pendulums.

Calibration was performed using six precision weights (1x50 mg, 2x200 mg, 1x500 mg, 1x1g, and 1x2 g) and a pulley directing their respective forces (0.5-39.5 mN) to the inner pendulum, and it was repeated six times before and after the thruster operation to reduce errors. The resulting calibration curve had an R squared value of 0.9999 indicating almost perfect linearity. Figure 4.2-3 shows a photo of the XPT mounted on the thrust stand and the calibration curve.

In addition, a commercial precision balance has been successfully tested for micro-Newton resolution thrust measurement of electric thrusters. Results suggest that a precision balance can be useful as a very simple alternative thrust stand or it can used to validate results of the existing thrust stands. Please see Appendix 4.3 for the details of this thrust measurement method, and to see how its results compare to the dual pendulum thrust stand.

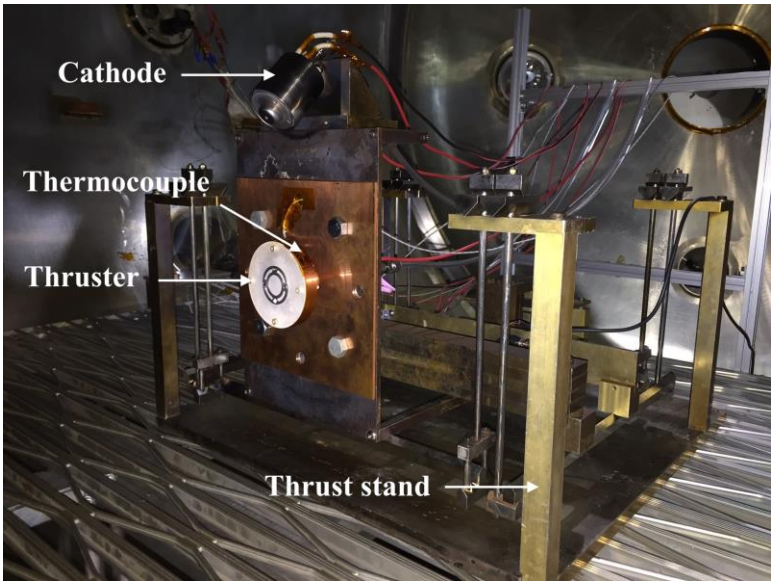

Figure 4.2 Dual pendulum thrust stand.

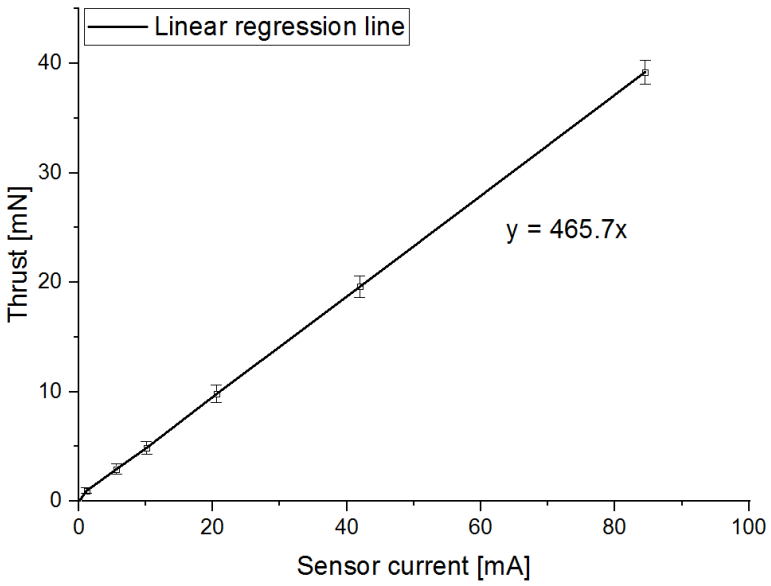

Figure 4.3 Calibration curve.

4.1.3 Discharge current oscillations

A high frequency current probe (Hioki 3273-50) having a bandwidth of 50 MHz, was clamped on to the anode cable near a high voltage DC power supply (Takasago EX-1125U2) to capture discharge current waveforms via an oscilloscope (Iwatsu DS-5614A). No filter unit is used between the thruster and the power supply. Discharge current oscillation amplitude (Δ) is an indicator of stability for a thruster operation. It is defined as the root-mean-square (RMS) of the time-varying component of the discharge current waveform, and can be formulated as follows:

$$\Delta = \frac{\mathrm{RMS}}{\bar{I}_d} = \frac{1}{\bar{I}_d}\sqrt{\int_0^{\tau}\frac{(I_d - \bar{I}_d)^2}{\tau}}, \qquad \left(\bar{I}_d = \frac{\int_0^{\tau} I_d}{\tau}\right) \tag{4.1}$$

where RMS is root mean square, I_d is discharge current, and τ is time.

Lower oscillation amplitudes at wide range of operating conditions are preferred because it can alleviate complexity of a power processing unit (PPU) and reduce its mass. Besides, if current oscillations grow strongly in amplitude, the discharge (and thrust generation) can be suddenly interrupted. Oscillations may also be linked to adverse effects such as defocusing of the ion beam and intensified erosion of the discharge channel.[2] Broader stability region (i.e., the oscillation amplitude of SPTs is usually below 0.2, whereas it may exceed 1 for TALs.) is one of the main reasons that SPTs have been more actively employed in space missions although TALs are physically more compact.

4.1.4 Uncertainty analysis of performance results

Table 4.2 shows the detailed uncertainty analysis. There are four physical parameters produces uncertainties in the experimental results: Thrust, mass flow rate, discharge current and anode potential. Thrust measurement and mass flow rate measurement are the main source of uncertainties. The thrust stand measurement error was calculated to be minimum ±0.25 mN, and a maximum ±1.0 mN depending on the thrust level according to the standard deviation of the calibration curve, which was assumed to include systematic errors (Thermal drift, friction between moving and stationary components) and errors due to the calibration mechanism (Pulley friction, and the angle of string connecting calibration weights to the thrust stand). Uncertainties in the masses of the calibration weights were assumed to be insignificant.

The mass flow controller delivering gas to the anode has a full scale (100 sccm) measurement uncertainty of ±1%, provided by the manufacturer. It should be noted that uncertainty in the mass flow rate is higher for lower mass flow rates (20 % for 0.48 mg/s, 10% for 0.95 mg/s and 6.7 % for 1.43 mg/s).

Discharge current was measured by a current probe with ±1% reading accuracy, which is provided by the manufacturer. Regarding the anode potential, maximum voltage drop due to resistance between power supply output and thruster anode (~0.08 Ohm) was calculated to be ~ 0.1 V, and thus assumed to be trivial (less than 0.1%).

Table 4.2 Detailed uncertainty analysis.

Thrust	
Dispersion of repeatedly measured thrust (1 sigma)	0.25 - 1mN depending on the operation condition
Calibration weights (Provided by the manufacturer)	±0.5%
The angle of string connecting calibration weights to the thrust stand (Estimated)	±0.5%
Pulley friction (Measured using a precision balance)	±0.5%
Anode mass flow rate	
100-sccm mass flow controller with ±1% full scale accuracy (Provided by the manufacturer)	20 % for 0.48 mg/s 10% for 0.95 mg/s 6.7 % for 1.43 mg/s
Discharge current	
Current probe reading accuracy (Provided by the manufacturer)	±1%
Anode potential	
0.1 V voltage drop due to resistance between power supply output and thruster anode (Measured using a voltmeter)	± 0.1 %

Thrust and discharge current measurements at each operating condition were repeated three times, and the average of the measured values are plotted in Fig. 4.11 with error bars. Error bars represent total measurement uncertainty for thrust and the standard deviation of the mean of the discharge current. To determine error bars for efficiency and specific impulse, uncertainty in thrust, mass flow rate, and discharge current measurements were aggregated according to error propagation formula below:

$$Q = \frac{ab\cdots c}{xy\cdots z};\ \frac{\delta Q}{|Q|} = \sqrt{\left(\frac{\delta a}{a}\right)^2 + \left(\frac{\delta b}{b}\right)^2 + \cdots + \left(\frac{\delta c}{c}\right)^2 + \left(\frac{\delta x}{x}\right)^2 + \left(\frac{\delta y}{y}\right)^2 \cdots + \left(\frac{\delta z}{z}\right)^2} \quad (4.2)$$

where, a, b, c,... are measured quantities with uncertainties δa, δa, δc,... . Q is the quantity of interest which depends on a, b and so forth. Table 4.2 breaks down the uncertainties.

4.1.5 Faraday probe and data collection

A cylindrical coordinate system is defined such that the plasma plume is axisymmetric about the z axis. The thruster exit plane is located at z = 0, and the centerline of the probe is always parallel to the z-axis. Ion current density measurements were taken by sweeping a nude Faraday probe with a 2-axis motorized translation stage in the radial direction at several axial distances. Figure 4.4 shows a diagram of the measurement setup. The method is in line with a variation of that used by Huang et al.[3] with some alterations, and it was chosen due to equipment constraint although it may be more sensitive to non-beam ions than sweeping the probe according to a hemispherical coordinate system.[4]

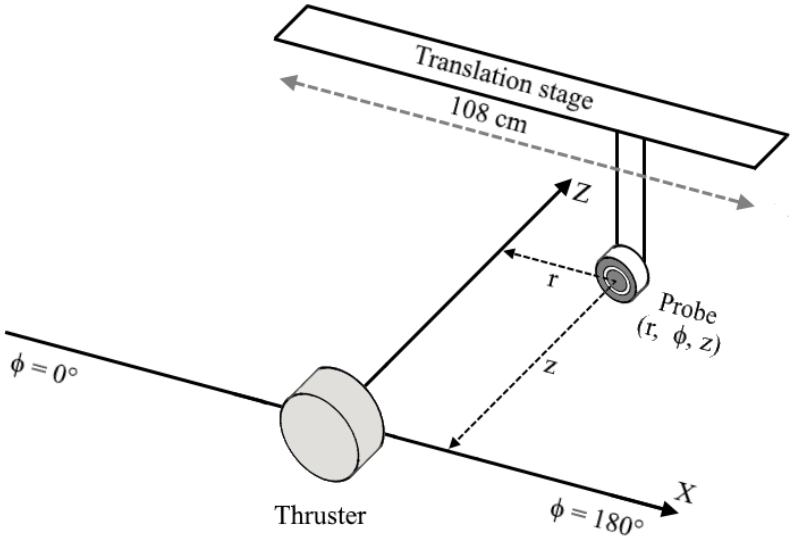

Figure 4.4 A diagram of Faraday probe measurement setup.

The probe consists of a collector (⌀20 mm, SUS 403) and a guard ring (⌀30 mm, SUS 403) mounted to a macor backplate with venting holes to reduce neutral flow effects. Gap between the electrodes is about 0.4 mm providing a flat sheath over the collector surface. To reduce edge effects, the collector and the guard ring were both biased at the same potential (-20 V, Takasago GP0110-1), which was sufficient to reach ion saturation. Figure 4.5 shows the probe design and electrical diagram for data collection.

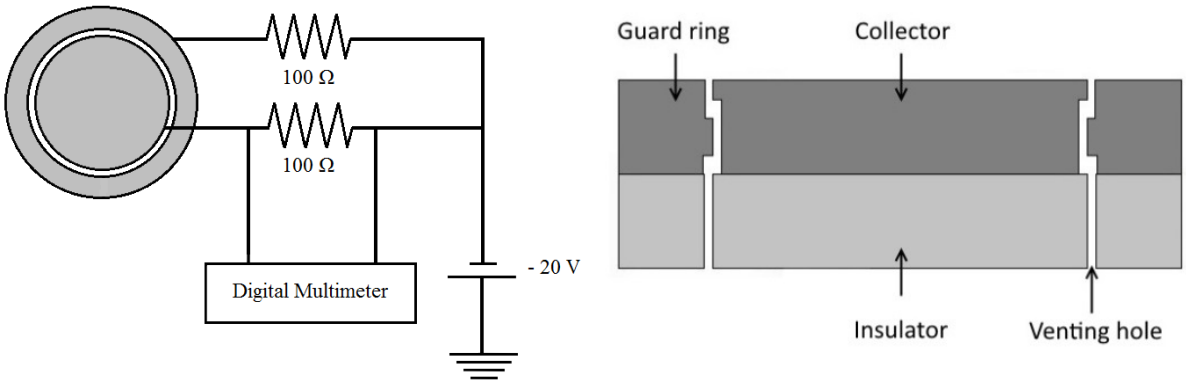

Figure 4.5 Electrical diagram and probe cross section.

The motorized translation stage has a width of 108 cm providing a maximum 54 cm travel distance in +X /-X directions. The probe was moved with 20 mm resolution starting at +X, and stopped at each point about 3 seconds to measure the shunt voltage. Moving the probe from +X to –X took approximately 3 minutes. The thruster plume was also scanned in the opposite direction to check repeatability. Measurements were taken at two fixed axial distances 4 and 8 D_A (anode diameter).

Vertical aluminum arm carrying the probe head was covered with Kapton. Twisted shielded pair cables were used and the shield was grounded to the vacuum chamber walls for signal noise reduction. Discharge currents were not disturbed during the probe sweeps. Practices recommended by Brown et al.[4] were generally adopted.

4.1.6 Efficiency analysis

Anode efficiency η_a is the indicator of overall energy conversion of the thruster-head. To analyze thrust generation processes it can be divided into voltage utilization efficiency η_V, current utilization efficiency η_b, charge utilization efficiency η_q, mass utilization efficiency η_m, and beam utilization efficiency η_d, which is also called plume divergence efficiency as:

$$\eta_a = \frac{T^2}{2\dot{m} I_d V_d} = \eta_V \eta_b \eta_q \eta_m \eta_d \tag{4.3}$$

where T is thrust, $\dot{m}$ is anode mass flow rate, I_d is discharge current, and V_d is anode potential.

The voltage across a 100 Ω current shunt resistor was recorded with a digital multimeter (Iwatsu VOAC 7523). Local ion current density $j_z(r)$ is calculated by dividing this voltage by the collector area and the shunt resistance. Ion beam current (I_b) can be obtained from Eq. (4.4) by integrating the local ion current density. Current utilization efficiency is the ratio of ion beam current to discharge current as shown in Eq. (4.5). Mass utilization efficiency can be estimated from the measured thrust using Eq. (4.6) if charge-state information from a E × B probe is not available. [3]

$$I_b = 2\pi \int_0^\infty j_z(r) r dr \tag{4.4}$$

$$\eta_b = \frac{I_b}{I_d} \tag{4.5}$$

$$\eta_m \cong \frac{T}{\dot{m}\sqrt{\frac{2e(V_d - V_L)}{M_{xe}}}} \tag{4.6}$$

where T is thrust, $\dot{m}$ is anode mass flow rate, e is the elementary charge, V_L is the voltage loss, and M_{xe} is the equivalent mass of elemental xenon.

The charge utilization efficiency measures overall charge state of the beam ions and decreases linearly with applied anode potential. Its value can be assumed to equal to 0.99 for Hall thrusters operating at low anode potentials (< 300 V). The voltage utilization efficiency explains amount of the potential energy which is converted to kinetic energy, and defined as the ratio of beam voltage to discharge voltage ($\eta_V = V_b/V_d$). The beam voltage can be assumed to be $V_b = V_d - V_L$, where V_L is the loss voltage (assumed to be 15 V).

$$\eta_V = 1 - \frac{V_L}{V_d} \tag{4.7}$$

Eq. (4.8) gives an approximate value of charge-weighted average divergence angle δ for a radially-swept probe [3]. Then, beam efficiency can be expressed in Eq. (4.9).

$$< \cos \delta >_j = \frac{2\pi \int_0^\infty j_z(r)\cos\theta r dr}{2\pi \int_0^\infty j_z(r) r dr}, \qquad \cos\theta = \frac{z}{\sqrt{r^2 + z}} \tag{4.8}$$

$$\eta_d = \left(< \cos \delta >_j\right)^2 \tag{4.9}$$

where z is the distance between the thruster exit(the front surface of the anode in our case) and the collector.

Equation (4.4) and Eq. (4.8) dictate that the probe should be swept from the center of thruster exit plane to infinity at an azimuthal angle in the radial direction, but obviously this is not feasible. So, half-width of the translation stage (54 cm) was chosen as the integration limit, which gave reasonable total ion beam current to discharge current ratios (< 1) for all the operating conditions. Details of this efficiency breakdown scheme can be found elsewhere.[3, 5]

4.1.7 Uncertainty analysis of Faraday probe measurement

The digital multimeter has an input resistance of 1000MΩ yielding to ~20 nA probe leakage current for a bias of -20 V. Secondary electron emission from the collector due to impingement of ions with energies lower than 300 eV can be assumed to be insignificant for stainless steel surfaces.[6] Tungsten coating might be necessary at discharge potentials over 300V. Positioning error of the translation stage is of ±1 mm. Systematic errors associated with Bohm current collection, sheath expansion, divergence angle reference point and thermionic emission due to excessive probe heating can be disregarded for the far-field ion current density measurements. Random errors and digital multimeter measurement error (e.g. drift, offset, noise, and etc.) were estimated to be ±0.05 mA/cm^2 by comparing consecutive measurements.

The effective collection area and background pressure effects can be given as two main sources of uncertainty. The collector and the guard ring have the shape of a cylinder with flat and curved surfaces. Ions entering the gap between the collector and guard ring are collected at the curved surfaces and give rise to uncertainty in the effective collection area. The area correction factor suggested by Brown[4] is not suitable for correcting radially swept data since the probe face does not remain constantly pointed at the thruster as in a polarly swept probe. It was still calculated and found to be 4% for our probe corresponding to an uncertainty of -4 % in ion current density. Quantifying background pressure effects (i.e. CEX collisions and neutral ingestion) is also difficult for the radially swept probe because the distance between the probe and the thruster is not constant. All things considered, it seems reasonable to assume a conservative range of ±10 % for the total uncertainty.

Measurements should be repeated at a minimum of three different background pressures for extrapolation of ion current density to zero. This was avoided because polar sweeps are more advisable for the space environment predictions, which is beyond the scope of this paper.

4.1.8 Langmuir probe and data acquisition

Langmuir probe is a kind of electrostatic probe used for diagnosing basic local macroscopic plasma properties. It is classified according to number of electrodes (e.g., single, double and triple) or electrode shapes (e.g. cylindrical and spherical). Plasma properties such as plasma density and electron temperature are determined by analyzing current-voltage (I-V) characteristic curves, which are obtained by varying the probe bias voltage, and measuring the current across a shunt resistor.

Langmuir probe theories such as thin sheath limited theory are applicable when the plasma is in collisionless regime. The Knudsen number ($K_n = \lambda_{MFP}/r_p$) defined as the ratio of the molecular mean free path length λ_{MFP} to the probe radius r_p is used to describe plasma flow regimes. Plasma flow is said to be in a collisionless regime when $Kn \gg 1$. In Hall thrusters the probe operates in the collisionless regime even near the anode region as electron and ion mean free paths (> 10 cm) are several orders of magnitude greater than the probe radius (< 1 mm). Langmuir probe I-V curves are often analyzed according to the thin sheath limit or the orbital motion limited (OML) ion collection theories.[7,8] The ratio of the probe radius to Debye length (r_p/λ_D) is used to determine which theory is appropriate. In order to apply the OML theory Debye length should exceed the probe radius ($r_p/\lambda_D < 1$). As for the thin sheath theory, Debye length should be much smaller than the probe radius ($r_p/\lambda_D \gg 1$). The OML theory is valid only for small probes in low density plasmas where the sheath is so thick compared to the probe radius. In this study, it was estimated that the ratio r_p/λ_D is much larger than the unity, so the thin sheath theory was applied to the I-V curves of a floating double probe.

Measurement domain represents a right circular cylinder. Figure 4.6 shows a cylindrical coordinate system (r, θ, z) with origin at the center of the anode front surface. I-V curves were taken at three radial positions (the thruster centerline, the anode disc centerline and the points halfway between them) with 22.5° angular resolution in the azimuthal direction and three axial locations (z = 10, 20 and 30 mm) and in two cathode position configurations: 1) on top of the thruster θ = 0° direction and 2) on bottom of the thruster at θ = 180° direction.

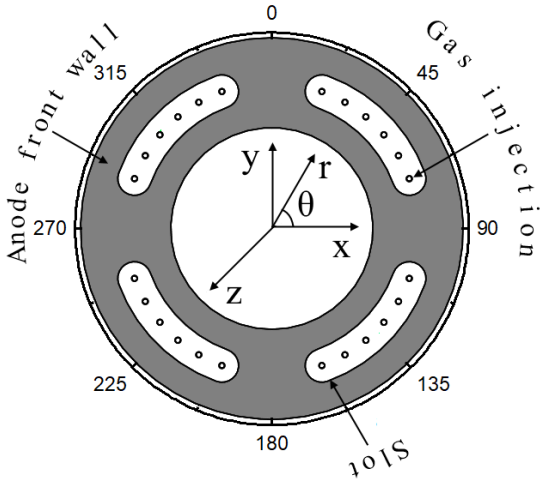

Figure 4.6 Measurement domain.

Figure 4.7 shows a simplified schematic of the double probe electrical circuit. The double probe consists of only an alumina ceramic tube with double-bore, and it has two identical tungsten electrodes 0.35 mm in diameter. Disturbance of the double probe on the plasma, but also its spatial resolution, lower than of the single probe as its electrodes floats with the local plasma, and collect ion saturation current. The wires exit 2 mm beyond one end of the alumina tube, and are attached to coaxial BNC cables and at the other end. The probe was mounted to a 3-axis positioning system (OriginalMind), which has an uncertainty of ± 0.1 mm provided by the manufacturer, and can attain a velocity of 500 mm/sec.

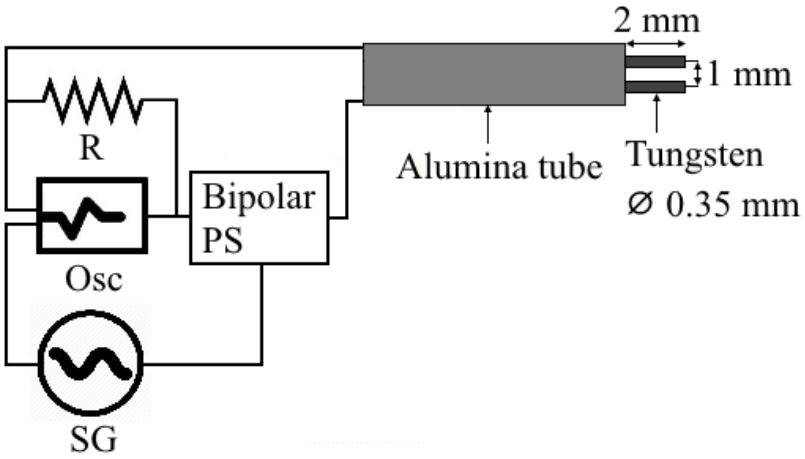

Figure 4.7 A schematic of the double probe electrical circuit.

The data acquisition circuit works as follows. The positioning system moves the probe to a pre-defined measurement point inside the thruster plume. A bipolar power supply (Takasago BWS 120-2.5) amplifies 5 Hz sine waves produced by a signal generator (Iwatsu FG-350), and applies a variable voltage ± 110 V to the probe. I-V trace is measured, and recorded with an oscilloscope data logger (Yokogawa DL750) across a 100 Ω ceramic current shunt resistor with a sampling rate of 10 kS/s. This corresponds to 2000 points per I-V curve for a 5 Hz voltage oscillation frequency. The probe is then taken out, and allowed to cool for over 10 seconds before the next injection.

4.1.9 Data processing and uncertainty analysis of Langmuir probe measurement

The shunt resistor was enclosed in a grounded metal box to reduce noise. A hysteresis between upward and downward voltage sweeps is observed when the probe electrode surface is contaminated. The contamination can lead to inaccurate estimates of plasma densities and electron temperatures if not corrected. The electrode contamination issue was addressed by periodically cleaning the double probe tips with ion bombardment. Insertion of the probe into the thruster plume can strongly disturb the plasma based on the distance downstream of the anode. The discharge current was monitored while inserting the probe, and we did not observe changes more than % 6. I-V curves had a clean shape (see Fig. 4.8), so the raw curves were not numerically smoothed. The capacitive current ($I_{cap} = CdV/dt$) may occur due to stray capacitance and probe voltage sweep. It was characterized by sweeping the same bipolar voltage on the probe without plasma discharge, and found to be lower than ion saturation currents by one order of magnitude. Figure 4.8 shows the capacitive current caused by stray capacitance.

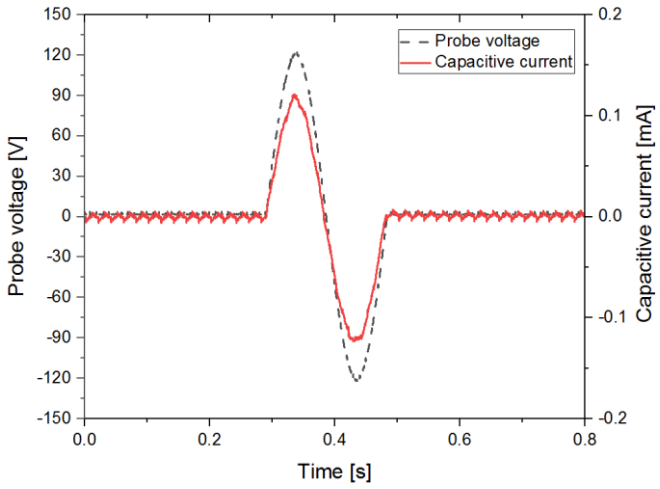

Figure 4.8 Capacitive current of the electrical circuit.

The probe is inserted into the plasma, and the current is measured as a function of the voltage difference between them. The polarity of the biasing voltage is varied from negative to positive to get ion saturation current in both directions, which results in symmetric I-V characteristics such as the one shown in Fig.4.9.

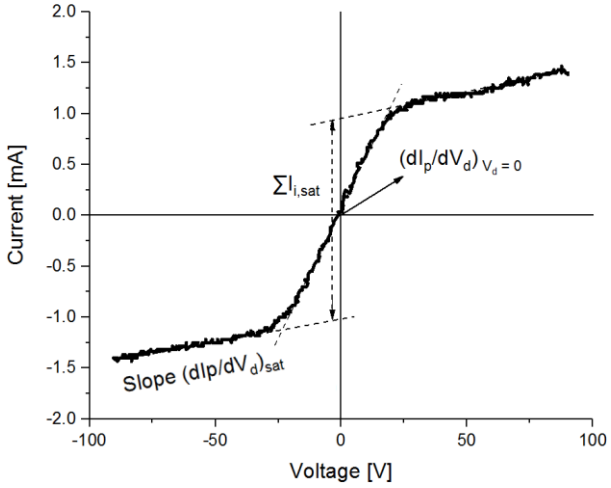

Figure 4.9 An example of raw I-V curve obtained at 250 V - 1.43 mg/s.

According to Eq. (7), electron temperature can be derived from the slope of an I-V curve at zero bias voltage. [9]

$$\frac{k_B T_e}{e} = -\frac{\sum I_{i,sat}}{4\left(\frac{dI_p}{dV_d}\right)_{V_d=0} - 3.28\left(\frac{dI_p}{dV_d}\right)_{sat}} \tag{4.10}$$

where $\sum I_{i,sat}$ is illustrated in Fig. 4.9, I_p is the probe current, V_d is probe bias voltage, k_B is Boltzmann constant, T_e is electron temperature, and e is the elementary charge.

The absolute value of the ion saturation current does not influence the electron temperature in Eq. (4.10). The fitting error for $(dI_p/dV_d)_{V_d=0}$ is less than 1%. Plasma fluctuations will affect shape of the slopes in the current saturation regions, but it will cause an error of 5% or less even if the slope error is large as much as has 200%.[10] The temporal fluctuation of the ion saturation current is the dominant source of error. Error for the electron temperature is estimated to be about 10-30%, which corresponds to the coefficient of variation (CV) of measured ion saturation currents. The ion number density (n_i) can be approximated by the thin sheath theory from Eq. (4.11) assuming a Maxwellian electron energy distribution, and that sheath around the probe tips is so thin that it does not notably

alter the effective probe collection area that is $r_p \backslash \lambda_D \gg 1$, where r_p is radius of the probe electrode, and λ_D is Debye length.

$$n_i = \frac{I_{i,sat}}{0.61 e A_s \sqrt{\frac{k_B T_e}{M_i}}} \tag{4.11}$$

where $I_{i,sat}$ is ion saturation current, A_s is surface area of the probe electrodes, and M_i atomic weight of ions.

Accuracy of the ion density measurement is much lower than the electron temperature because the propagation formula includes the error terms related to ion saturation current, sheath area, and also electron temperature. The minimum error in the ion density is estimated to be 52% assuming uncertainties of ±10%, ±50%, and ±10% for ion saturation current, sheath area, and electron temperature respectively. Determining an upper bound on the error is not an easy task because plasma is non-stationary (i.e., plasma Mach number $\approx \sqrt{2V_d/T_e} \gg 1$) in the plume of electric thrusters; however, the thin sheath theory gives an accurate estimate of the ion density for a cylindrical probe in stationary plasma, and under collisionless condition. The probe was mounted to the positioning system such that its longitudinal axis will be normal to the surface of anode and parallel to the plasma flow direction so that non-stationary plasma effects, and also the effect of magnetic field on the I–V characteristics will be reduced.[11] Measured maximum magnetic field strength at z = 10 mm was about 0.017 Tesla. Although these uncertainty ranges seem large, the trends in the data should be consistent with the reality. So, absolute plasma parameters cannot be accurately known but the double probe is still useful to discuss about plasma parameters.

4.1.10 Anode temperature measurement

Plasma density in a Hall thruster is directly related to residence time of neutrals in discharge channel, and it is a function of anode/channel wall temperature due to rapid thermal accommodation of neutrals at anode/channel walls. Hence, knowledge of anode temperature is very valuable for accurate plasma simulations especially for the external discharge plasma thruster for which power deposition from plasma to anode is a more significant factor in the thruster operation. Yet, a direct and accurate measurement of anode temperature is a challenging task.

Until now infrared cameras have been used to take thermal images of the thrusters from different observation angles at large relative distances (~2-4 m).[12, 13] One of the major drawbacks using a thermal camera during the thruster operation is that its readings are

questionable because the presence of plasma brings an important uncertainty in collected radiation.

Anode surface temperature was measured at several operating conditions using a commercially available low cost infrared sensor (Calex PyroUSB CF). The sensor can measure temperatures up to 1000 °C and its minimum focal spot size is 5 mm (i.e., it reads average temperature of a spot 5 mm in diameter) at 100 mm distance. The sensor was mounted on the translation stage inside the vacuum chamber and connected to PC through USB port. The output signal was processed and recorded using specialized software supplied by the manufacturer. The thruster was fired at operating conditions of 200-250 V and 0.95-1.43 mg/s mass flow rates. The anode was allowed to reach thermal equilibrium by continuous operation for 30 minutes at each operating condition. The sensor was put in a rest position behind the thruster during operation, and then moved to the front of the anode by the motorized translation stage right after the thruster shut down. Temperature was measured at one point on the anode centerline, which is the closest to the cathode and marked by the red dot laser seen in Fig. 4.9 (left). The ambient temperature near the thruster was also measured by a thermocouple. Moving the sensor from its rest position to the front of the anode took four seconds. The temperature at t = 0 s was extrapolated from the cool-down curves of the anode. Figure 4.10 (left) shows the emissivity measurement setup.

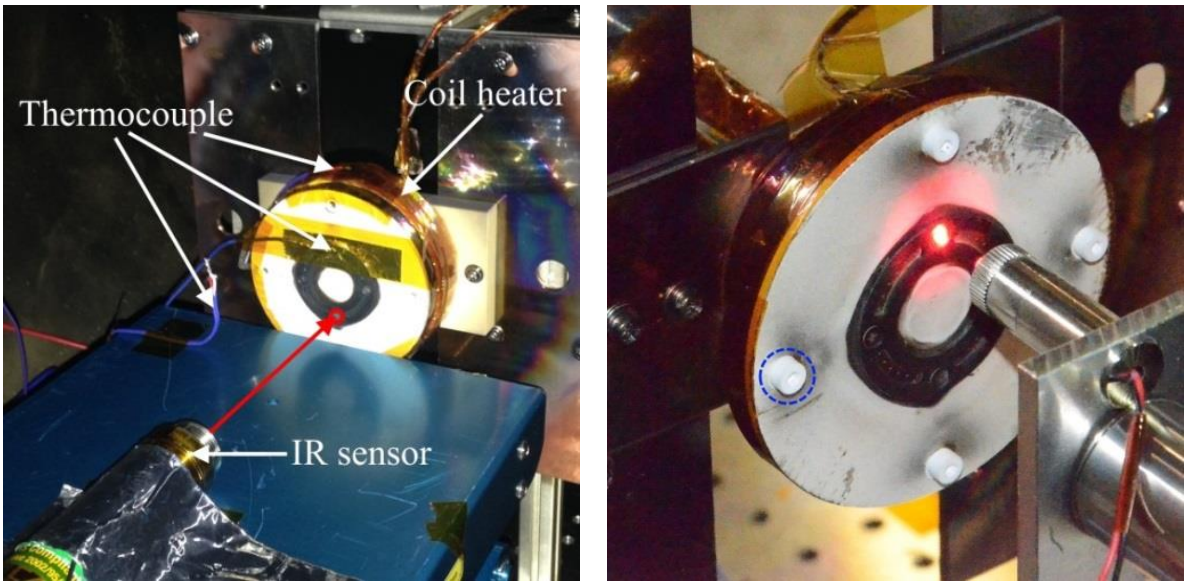

Figure 4.10 Sensor positioning (left) and emissivity measurement setup (right).

This method differs from the preceding ones in these:

1) A viewport window or a pressurized enclosure is not needed, thus eliminating the uncertainties related to the radiation transmission,

2) Measurements are taken immediately after the thruster was turned off so, there is no disturbance due to plasma flow, and

3) The distance between the sensor and the target can be kept very short (a few cm), which greatly increases resolution and cuts out interference from other thruster surfaces.

A thermocouple could also be used to measure temperature on the rear of the anode. Nevertheless, infrared sensor is able to directly measure surface temperature and does not require any structural modifications to thruster components, which can be prohibitive for a compact thruster like the XPT.

4.1.11 Determination of anode emissivity and data processing

Every grey body hotter than absolute zero emits light at infrared spectrum or infrared radiation whose intensity is proportional to the to the fourth power of its absolute temperature and emissivity ($E= \sigma\varepsilon T^4$). Non-contact temperature sensors detect intensity of this infrared radiation and convert it into a temperature value using a pre-defined emissivity coefficient. Emissivity significantly depends on chemical composition, surface characteristics such as temperature, wavelength and observation direction.

The anode of the XPT is made of 1 mm-thick molybdenum. Molybdenum is normally a silvery-white metal and has an emissivity between 0.05-0.2. Over the past experiments, a black material has been deposited on the anode and its surroundings as seen in Fig. 4.10 (right). This black material is electrically conducting and it originates from the beam damper and vacuum chamber walls sputtered away as ions impinge. Ceramic bolts, one of which is marked with dashed blue circle were replaced with brand-new ones for color comparison. To find emissivity of this deposited material, the anode was heated by a coil wrapped around the thruster body, and its temperature was measured under vacuum condition by the infrared (IR) sensor, and a K-type thermocouple. A second thermocouple was placed near the anode for ambient temperature compensation. The sensor's emissivity setting was adjusted until it displays the temperature of the thermocouple. The emissivity of the material deposited on the anode was 0.83 ± 0.01. Note that the thermocouple and the infrared sensor measures different points but the anode can be expected to have a uniform temperature distribution due to the symmetric structure of the heater coil and the thruster.

Figure 4.11 (left) compares the thermocouple, and infrared sensor readings. The temperature at $t = 0$ s was extrapolated from the cool-down curves of the anode, which was captured for three minutes. Figure 4.11 (right) shows a cool-down curve sample and exponential fit coefficients calculated by Origin data analysis software. The exponential fits were of the form:

$$y = A_1 \exp\left(\frac{x}{c_1}\right) + A_2 \exp\left(\frac{x}{c_2}\right) + A_3 \exp\left(\frac{x}{c_3}\right) + y_0 \qquad (4.12)$$

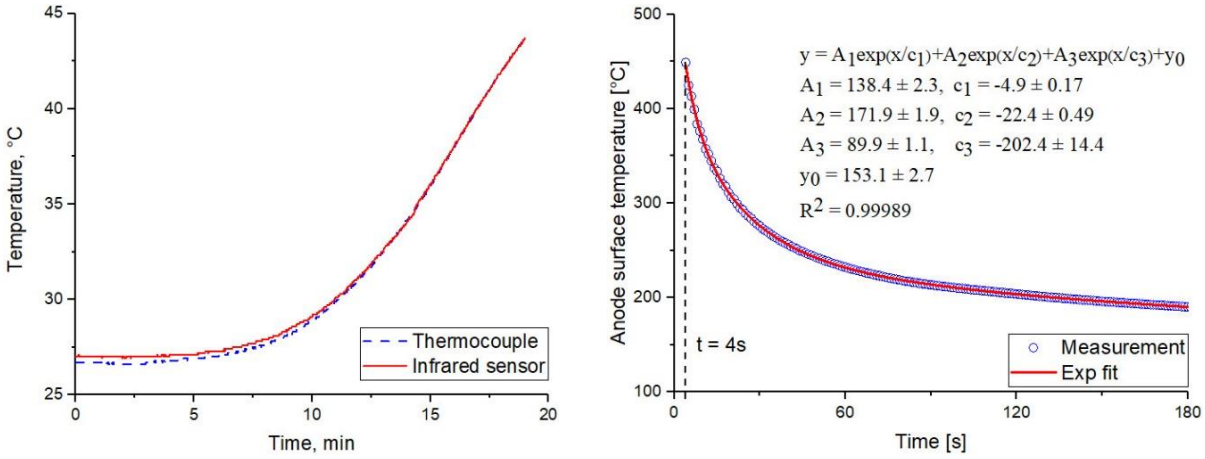

Figure 4.11 Infrared sensor calibration (left) and an exemplary cool-down curve of the anode (right).

4.1.12 Uncertainty analysis of infrared sensor measurement

Emissivity is the prevalent source of uncertainty. As stated before, chemical composition, surface characteristics, wavelength and observation angle are all the factors affecting emissivity. Emissivity is nearly constant when the sensor line of sight is normal to the anode surface. Spectral range of infrared sensors is from 7 to 14 µm and metals have relatively uniform emissivity at this wavelength range. Changes in chemical composition and surface characteristics of the anode except the surface temperature are expected to be insignificant. However, as surface temperature increases, emissivity of metals will also increase. Unfortunately, we were not able measure the anode emissivity at temperatures over 45 °C because of a coil failure. So it is hard to estimate the uncertainty in emissivity without experiment but we note here that actual anode temperatures should be underestimated. Regarding instrument uncertainty, infrared sensor has ±1% reading accuracy and thermocouple thermometer is able to measure temperature to 0.1°C accuracy.

In addition, although the regression lines almost perfectly fitted the data, travel time of the sensor from its rest position the anode downstream is considered to be long. The anode temperature would decrease sharply in the first four seconds which increases the uncertainty resulting from the extrapolation. It is therefore recommended that the sensor travel time should be reduced down to 1s or lower by using high speed translation stages. Also, it would be favorable to install an aperture stop on the infrared sensor head not to allow any material deposition on the sensor lens.

4.2 Results and Analysis

4.2.1 Thrust performance

Experiments were I-V curves, thrust, anode efficiency, and effect of background pressure on the discharge current are given in Fig. 4.12. The thrust and the anode specific impulse ranged from 2.4 to 17.4 mN, and from 503 to 1240 sec respectively at anode potentials of 150-200-250 V with anode mass flow rates of 0.48-0.95-1.43 mg/s demonstrating a versatile throttling range. The anode efficiency ranged from 12.3 to 25.6 % at discharge powers from 47 to 411 W. These values translated into a thrust-to-power ratio of 42 mN/kW.

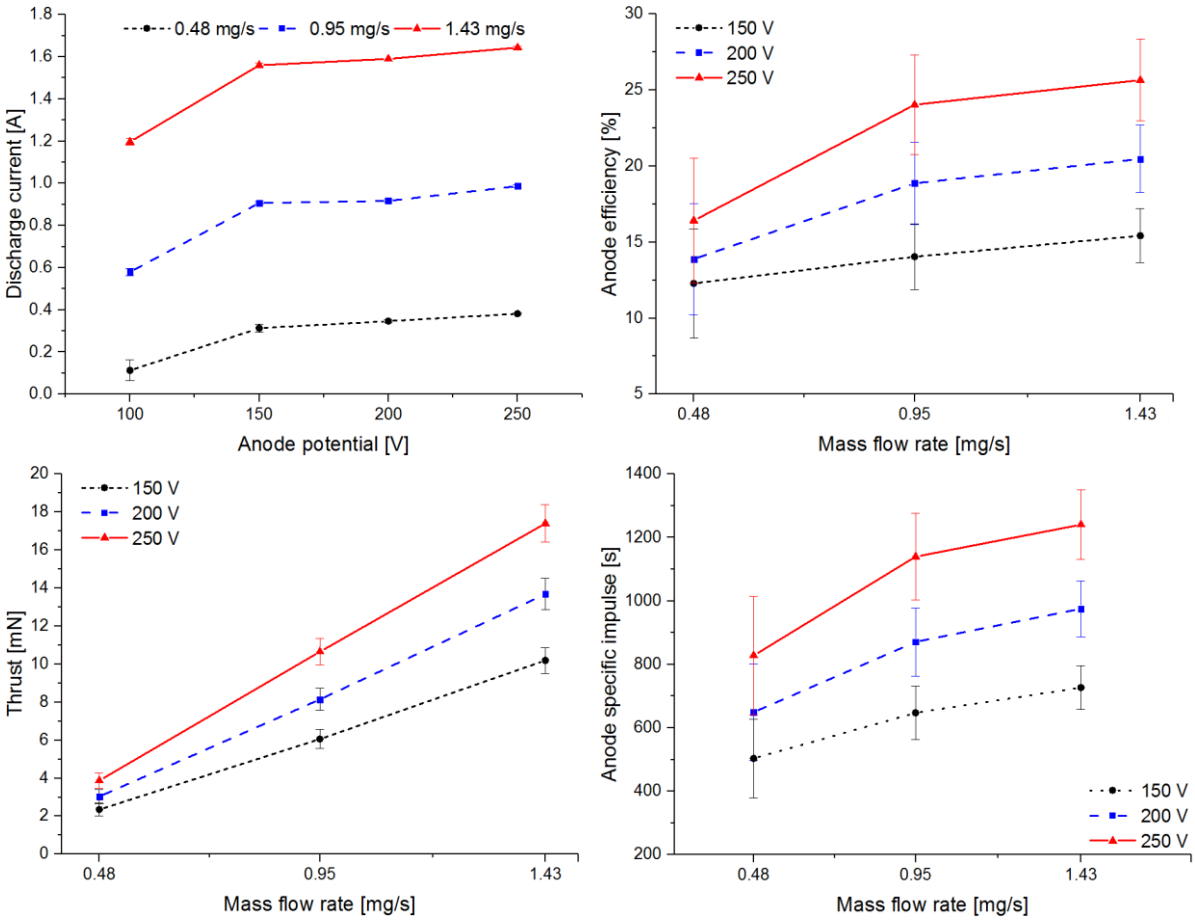

Figure 4.12 Experimental performance characteristics of the XPT. *Error bars represents 1-sigma standard deviation of the total error.*

The discharge current first increases rapidly due to the increased mean electron energy (ionization) as the anode potential increased from 100 V to 150 V as shown in Fig. 2(c), then the ionization fraction reaches its maximum value after which the discharge current either remains constant (current saturation) or increases slightly due to changes in electron mobility. This is a general feature of conventional Hall thruster behavior[14]. The cathode-ground potential remained between -7 V and -11 V.

In summary, the results demonstrate that the XPT can provide similar performance compared to stationary plasma thrusters (SPT), cylindrical Hall thrusters (CHT), and magnetically shielded SPTs at the same power levels despite the fact that neutrals are directly fed into vacuum after exiting the anode. For example, the SPT-30 thruster produces 13.2 mN of thrust at an anode specific impulse of 1370 s and an anode efficiency of 34% at 250 V anode potential and at 250 W discharge power.[15] The CHT produces 3 mN of thrust at an anode specific impulse of 1100 s and an anode efficiency of 20% at 250 V anode potential and at 90 W discharge power.[16] The MaSMi 40 produces a thrust of 13 mN with a specific impulse of 1,100 s at an anode efficiency of 22% at an anode potential of 275 V and discharge power of 325 W.[17] Please note that the performance of the other Hall thrusters reported here represents approximate values.

4.2.2 Discharge current oscillation

Oscillation amplitudes for a variety of operating conditions, and discharge current waves for 250 V operating condition, are presented in Fig. 4.13. Oscillation amplitudes remained lower than 0.2 for almost all of the operating conditions.

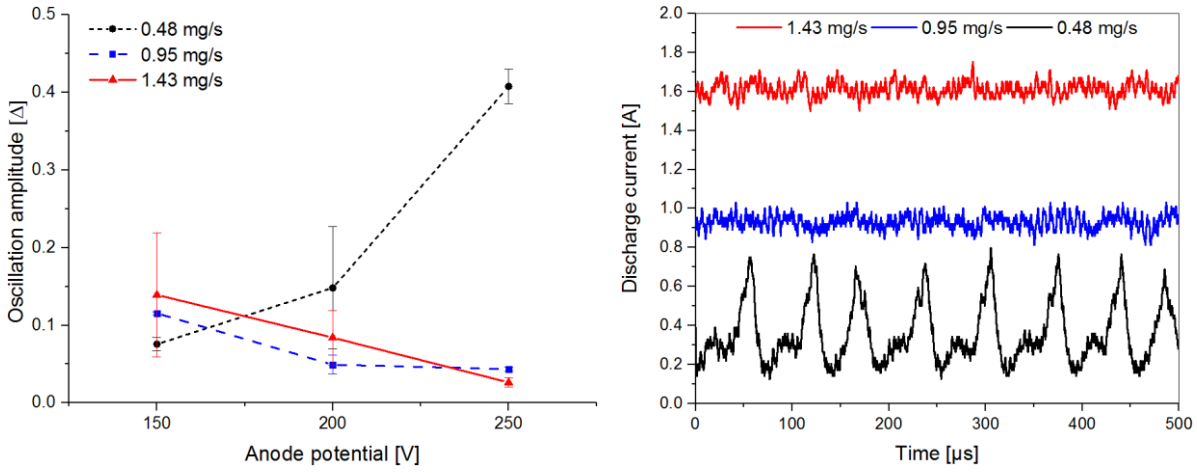

Figure 4.13 Experimental oscillation amplitudes and discharge current wave forms of the XPT at 250 V.

Oscillatory behavior is observed to decrease with increasing anode potential for 0.95 mg/s and 1.43 mg/s mass flow rates with increasing anode potential, whereas the reverse trend is observed for 0.48 mg/s. As for 250 V anode potential, oscillations become non-sinusoidal with peak-to-peak current values less than 0.2 A as the mass flow rate increased.

Power spectra density of the discharge current waves (Not given) indicated that low frequency oscillations (5-35 kHz) at 0.48 mg/s 250 V case is larger two orders of magnitude than 0.95 mgs/ and 1.43 mgs/ 250 V cases. Low frequency oscillations are related to ionization processes, and correspond to the breathing mode.[18] Breathing mode transition at 0.48 mg/s can be explained with periodic depletion of neutral atoms by electron impact ionization, also called predator-prey cycle[19]. The predator-prey cycle does not appear in 0.95 mg/s and 1.43 mg/s 250 V cases.

Hara[20] suggests that maximum ion production should be higher than ion acceleration to have steady-state plasma. We can discuss that plasma conditions to reach steady-state will be relaxed by the fact that loss of ions at wall boundary is so small because ionization region is not surrounded by a cavity. Besides, ionization and acceleration regions in the XPT are very close to the anode, and thus neutral supply. The time takes for the fresh neutrals, coming from the holes on the front wall, to reach ionization regions is about one order of magnitude shorter compared to SPTs. Therefore, we can say that breathing mode oscillations would be inherently stabilized to a certain extent according to the criterion for stabilization of the breathing mode[21]: $\partial n_n / \partial_t \geq 0$, which means neutral density (n_n) has a positive variation or not varying in time.

4.2.3 Beam characterization

Beam characterization gives us the breakdown of the thrust efficiency, so it is important for better understanding of the thruster operation. Ion current density profiles measured at axial distances of 4-8xD_A (D_A means anode diameter) for 1.43 mg/s mass flow rate are given in Fig. 4.14. The ion current density profiles are symmetric with respect to the thruster centerline. Peak current density decreases with axial distance due to particle scattering from the centerline to the plume wings, and the plume becomes more diffuse. High ion current density region called the center spike is observed on thruster centerline. The center spike becomes brighter and denser, and the plume loses its diffuse appearance when the discharge voltage increased from 150 V to 250 V. The ion current density profiles for 0.48 mg/s and 0.95 mg/s mass flow rates follow the same trends.

Double hump peaks that are often seen in Hall thruster plume profiles due to the annular discharge channel were not observed which may be due to relatively large area of the collector surface decreasing the sweep resolution. The probe data confirms that the far-field plume is strongly Gaussian, and ion beam focusing is fine.

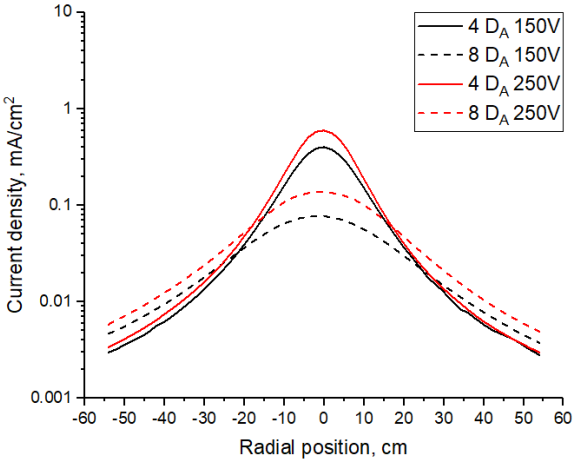

a) Ion current density profile 0.48 mg/s

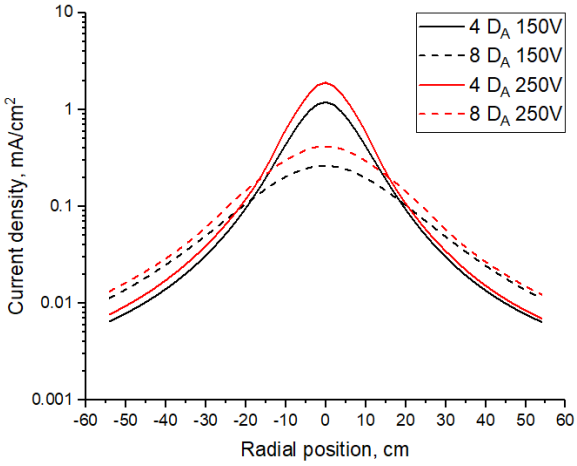

b) Ion current density profile 0.95 mg/s

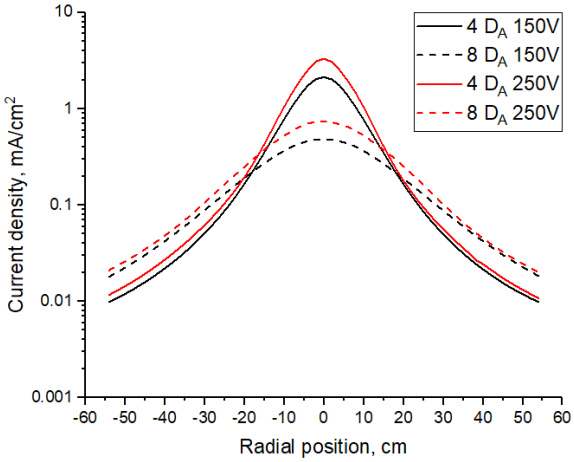

c) Ion current density profile 1.43 mg/s

Figure 4.14 Experimental ion current density profiles of the XPT. *Plotted on logarithmic scale, and D_A means anode diameter.*

Table 4.3 shows integrated ion beam currents, efficiency breakdown and plume divergence half-angles calculated for the ion current densities. The mass utilization efficiency, and plume divergence efficiency are the dominant loss mechanisms. Mass utilization efficiency indicates to what extent neutral propellant gets ionized, and contributes to thrust. It increases proportionally to mass flow rate, and discharge voltage since increasing mass flow rate results in higher neutral densities, and decreased ionization mean free path. A higher discharge voltage produces more ions due to increased electron density and temperature and improves current utilization efficiency.

Table 4.3 Experimental efficiency breakdown.

$\dot{m}$ [mg/s]		V_d [V]	D_A	I_d	I_b	η_V	η_b	η_m	η_d	η_q	δ [°]	η_a^F	η_a^T
0.48	Est →	150	0	0.29	0.29	0.90	1.00	0.28	0.43	0.99	49.1	0.11	0.09
		150	4	0.29	0.22	0.90	0.76	0.28	0.46	0.99	47.5	0.09	0.09
		150	8	0.29	0.15	0.90	0.59	0.28	0.56	0.99	41.6	0.08	0.09
	Est →	250	0	0.35	0.33	0.94	0.94	0.32	0.40	0.99	50.5	0.11	0.10
		250	4	0.35	0.28	0.94	0.79	0.32	0.48	0.99	46.0	0.11	0.10
		250	8	0.35	0.23	0.94	0.65	0.32	0.58	0.99	40.2	0.11	0.10
0.95	Est →	150	0	0.86	0.69	0.90	0.80	0.39	0.41	0.99	50.4	0.11	0.11
		150	4	0.86	0.58	0.90	0.67	0.39	0.48	0.99	46.1	0.11	0.11
		150	8	0.86	0.47	0.90	0.54	0.39	0.57	0.99	40.8	0.11	0.11
	Est →	250	0	0.94	0.91	0.94	0.97	0.54	0.46	0.99	47.1	0.22	0.20
		250	4	0.94	0.77	0.94	0.82	0.54	0.51	0.99	44.4	0.21	0.20
		250	8	0.94	0.63	0.94	0.67	0.54	0.60	0.99	39.2	0.20	0.20
1.43	Est →	150	0	1.53	1.20	0.90	0.78	0.50	0.42	0.99	49.5	0.15	0.15
		150	4	1.53	1.02	0.90	0.66	0.50	0.49	0.99	45.4	0.15	0.15
		150	8	1.53	0.84	0.90	0.54	0.50	0.58	0.99	40.3	0.14	0.15
	Est →	250	0	1.64	1.52	0.94	0.93	0.62	0.48	0.99	46.3	0.26	0.23
		250	4	1.64	1.31	0.94	0.80	0.62	0.52	0.99	43.9	0.24	0.23
		250	8	1.64	1.08	0.94	0.66	0.62	0.61	0.99	38.9	0.23	0.23
		250	12	1.64	0.88	0.94	0.54	0.62	0.68	0.99	34.2	0.21	0.23

Est shows values at 0 D_A estimated using a linear extrapolation.
η_a^F is anode efficiency based on the Faraday probe data, $\eta_a^F = \eta_V\eta_b\eta_q\eta_m\eta_d$.
η_a^T is anode efficiency derived from thrust stand data, $\eta_a^T = T^2/(\dot{m}P_d)$.
η_q was assumed 0.99.

Anode efficiencies determined by probe data matches well with those calculated directly from thrust stand results. Even though the peak current density decreases and the plume becomes more diffuse, plume divergence efficiency increases with axial distance of the probe because the integration area arising from Eq. (4.4) increases linearly from the thruster center to the radial axis limit. E×B probe measurements are not available; however, we can infer that mass fraction of multiply charged ions are large for some operating conditions because estimated beam currents exceed the theoretical limit for a beam composed exclusively of singly charged ions.

Efficiency components for 0 D_A were estimated through extrapolation of the ion current densities measured at 4 and 8 D_A. This was done because such estimation at the thruster exit corrects errors related to charge exchange collisions and the integration limit in Eq. (4.4). It may be thought that linear extrapolation with two points is subject to great uncertainty, but extrapolation with three points yielded only 1.3% difference in the

estimated beam current for 250 V 1.43 mg/s operating condition. So linearity assumption can be made. Note that there is still error arising from ionization of the background neutrals.

Figure 4.15 shows estimated anode efficiency components at the thruster exit ($0xD_A$). Standard high power Hall thrusters can achieve mass, plume divergence and discharge current utilization efficiencies of 80-90%, 70-90%, and 70-80% respectively at their optimum operating conditions.[22, 23] Current utilization efficiency is the dominant factor that limits the thrust efficiency and the efficiency loss can get severe for low power Hall thrusters. The XPT achieves relatively moderate mass utilization efficiency, and plume divergence efficiency, while its estimated current utilization efficiency varies between 80-100%. This result is significant considering that neutrals and magnetized plasma discharge are not confined to an annular or cylindrical cavity. Besides, it demonstrates that external discharge approach is effective in improving current utilization efficiency as power deposition on the discharge channel walls is mostly eliminated.

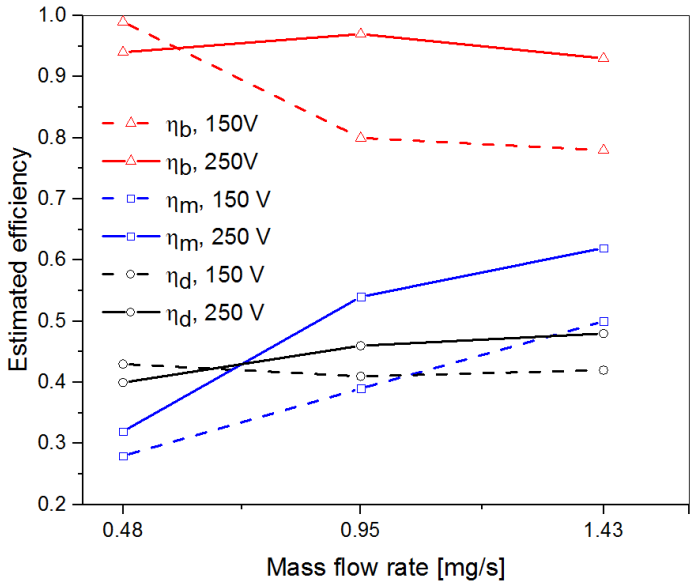

Figure 4.15 Anode efficiency components of the XPT estimated at the thruster exit ($0xD_A$) using experimental data. *η_b, η_m and η_d shows efficiencies related to current utilization, mass utilization and plume divergence respectively*

4.2.4 Plasma properties

Langmuir probe measurements were repeated three times at each point, and the results were averaged to plot polar contour graphs. Plasma properties were not time-resolved so the results should be considered time-averaged. Figure 4.16 compares 2D electron density maps, and distribution of electron temperature in the azimuthal direction along the anode centerline at an axial distance of 10 mm for the two cathode positions.

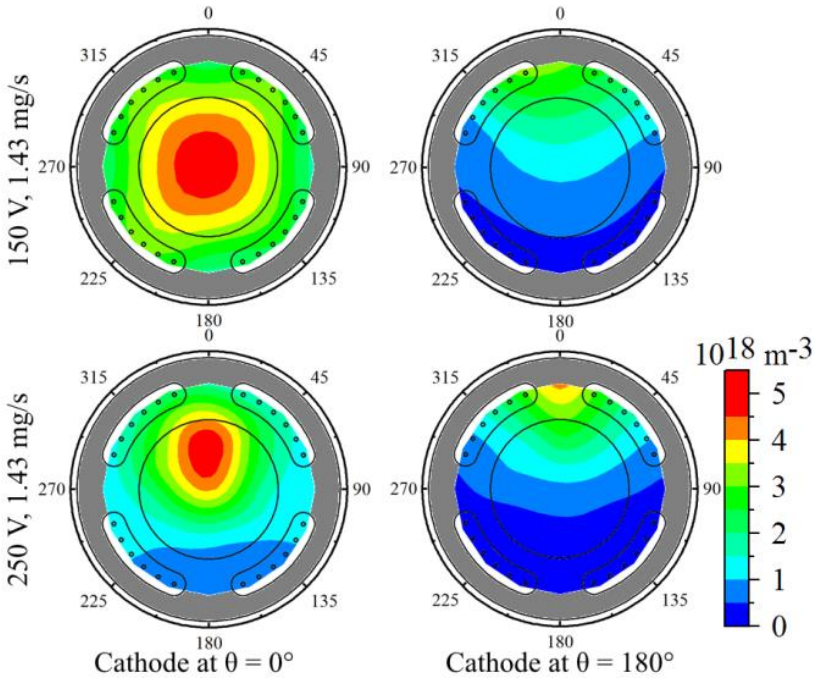

Figure 4.16 2D electron density maps of the XPT. *Experimentally measured for 150 V - and 250 V - 1.43 mg/s at z = 10 mm.*

Plasma density increases with mass flow rate up to $5x10^{18}$ m^{-3} and decreases with increasing axial distance down to $2x10^{17}$ m^{-3}. Average electron densities for 1.43 mg/s, 0.95 mg/s, and 0.48 mg/s mass flow rates at 250 V anode potential in the azimuthal direction along the anode centerline at 10 mm axial distance from the anode (z = 10 mm) were calculated to be $1.2x10^{18}$ m^{-3}, $0.9x10^{18}$ m^{-3}, and $0.4x10^{18}$ m^{-3} respectively. The plume plasma diffuses within the vacuum chamber, and becomes more uniform with increasing axial distances.

The thruster has four slots on the anode to inject propellant gas as plotted in Fig. 4.6, and this injection scheme leads to bright and dark regions in the plume. The bright regions are formed along the anode slots, and the light intensity is stronger at the slot center, while the dark regions are formed between the slots. The 2D electron density maps reveal a non-uniform feature of the plume plasma that the darks regions can have as much plasma density as the bright regions.

Variance (s^2) of the electron densities measured along the anode centerline was calculated for different operating conditions and cathode positions to measure uniformity of the plasma density (Not given here). Increasing the discharge voltage from 150 V to 200 V disturbs the uniformity, but increasing the voltage further to 250 V improves the uniformity. 200 V appears to be a critical threshold voltage for mode transition. Interestingly, the

oscillation amplitude is lower at 200 V than of 150 V. Increasing the discharge voltage from 150 V to 200 V results in reduced electron density along the anode centerline, but the electron density becomes denser at the thruster center. At the discharge voltage of 250 V, electron density at the thruster center decreases, and focuses in the upper part of the thruster between θ = 45° and θ = 315°. It follows that cathode position remarkably influences azimuthal uniformity as the variances associated with the cathode position of θ = 180° were significantly larger. The effect of the cathode position is also visible in the 2D maps. Electron density focuses in the upper part of the thruster for almost all operating conditions.

Figure 4.17 shows average electron density, and electron temperature profiles in the axial direction. Electron temperature distributions generally follow the same trend with the electron density. It is larger at the thruster center compared to average value of the anode centerline, and decreases in value and becomes more uniform with increasing axial distance. Electron temperature can be as high as 15 eV and as low as 2.5 eV at an axial distance of 10 mm.

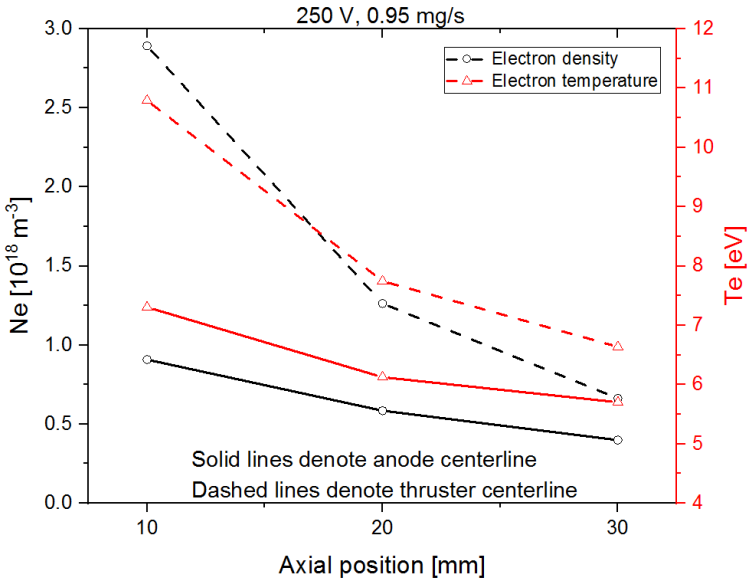

Figure 4.17 Electron density and electron temperature profiles of the XPT. *Experimentally measured in the axial direction for 250 V - 0.95 mg/s. Anode centerline means the line passing through the midpoints between the inner and outer edges of the anode disc.*

Figure 4.18-20 shows electron temperature and radial magnetic field profile in the azimuthal direction along the anode centerline at an axial distance of 10 mm for 150 V-, 200 V- and 250 V-1.43 mg/s. Azimuthal uniformity of electron temperatures is also influenced by the cathode position in a similar way to the electron density. The region in the upper part of the thruster between θ = 45° and θ = 315° has electrons with higher

temperatures. Measurement of radial magnetic field strength along the anode centerline in the azimuthal direction showed that its distribution is non-uniform.

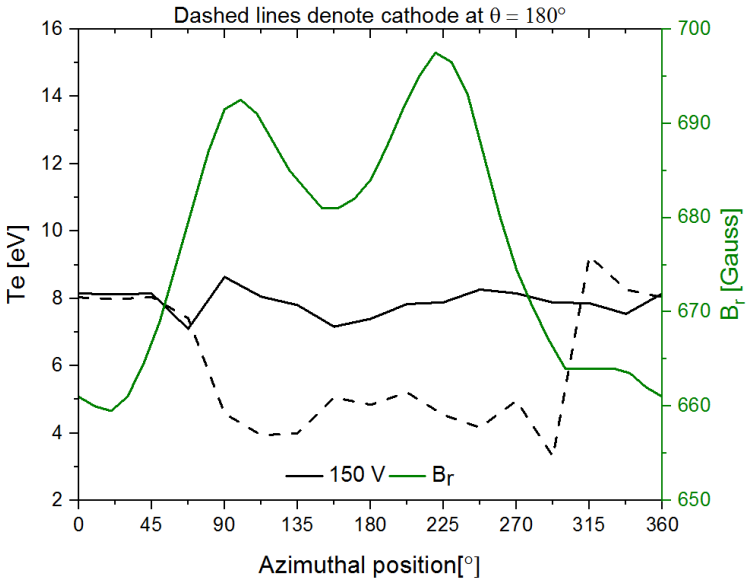

Figure 4.18 Electron temperature distribution of the XPT for 150 V - 1.43 mg/s.
Experimentally measured in the azimuthal direction along the anode centerline.

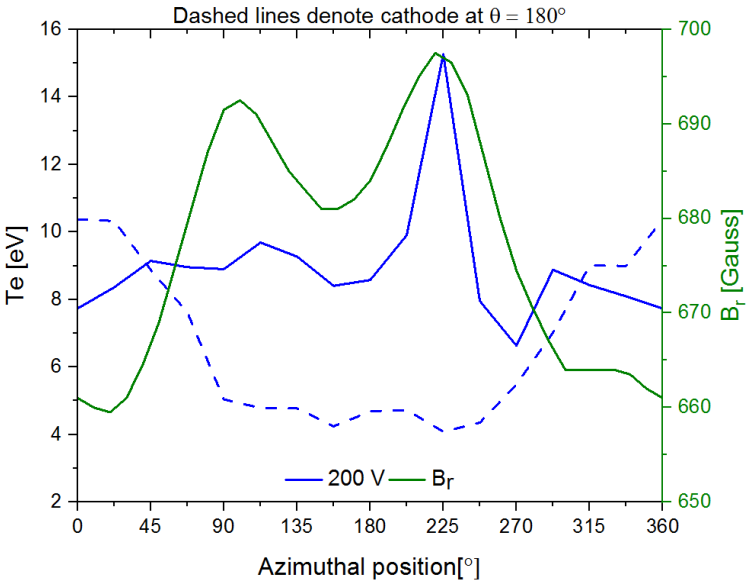

Figure 4.19 Electron temperature distribution of the XPT for 200 V - 1.43 mg/s.
Experimentally measured in the azimuthal direction along the anode centerline.

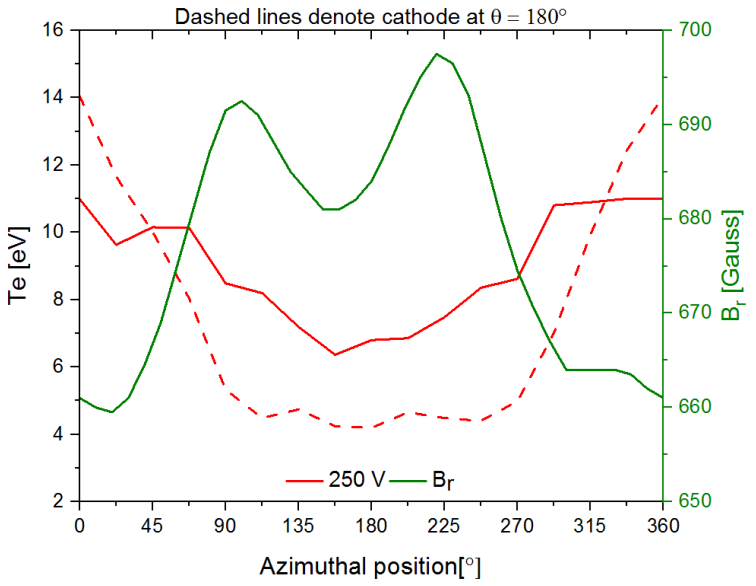

Figure 4.20 Figure 4.19 Electron temperature distribution of the XPT for 250 V - 1.43 mg/s. *Experimentally measured in the azimuthal direction along the anode centerline.*

Electron density and temperature may be expected to be higher in a region where radial magnetic field strength is the lowest, because electrons can diffuse, and accelerate more easily to the anode downstream where the neutral density and ionization probability is greater. Plasma density, and Br profile seems to be correlated. It is thus important to note that the non-uniformity of the azimuthal radial magnetic field have substantial influence on plasma density distribution even though its range is solely ~3% of the maximum Br value.

4.2.5 Infrared sensor

Thermal simulations are commonly performed to estimate anode temperature but anode temperature should be known accurately for meaningful comparisons between experiments and simulations because discharge current is a strong function of anode temperature especially in case of the XPT. For instance, we observed about 7% decrease (from 1.01A to 0.94 A at 250 V - 0.95 mg/s) in discharge current from beginning of the thruster firing until the anode reached the thermal equilibrium. Anode surface temperatures for different operating conditions are given in Fig. 4.21. It turns out that the XPT has the same level of anode temperature as in high power Hall thrusters. This can be attributed to its small anode thickness (1mm) and poor thermal conductivity due to ceramic front wall.

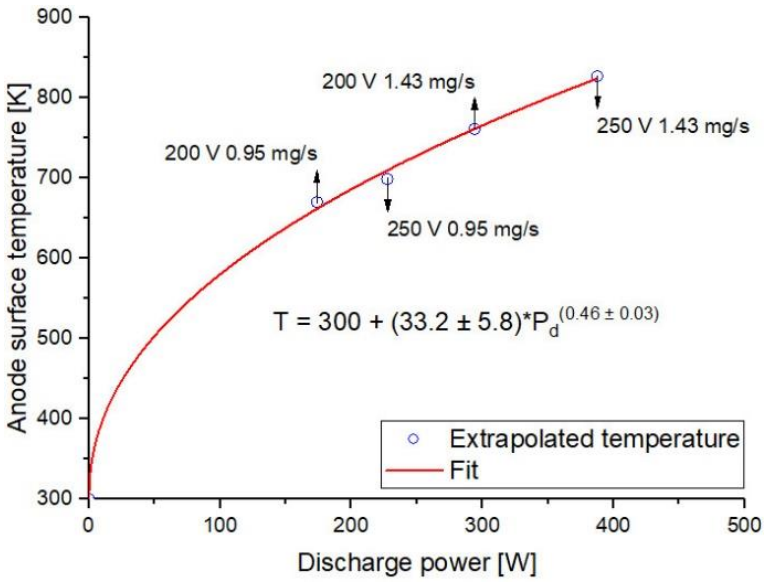

Figure 4.21 Experimentally measured anode surface temperatures of the XPT against discharge power.

A previous work[12] using infrared imaging showed that there is a relation between discharge channel wall temperature and discharge power and it can be expressed according to the following formula: $T = a + b \times P_d{}^n$ where a is wall temperature before thruster firing, b and n are parameters depending on wall geometry and/or material. We found that the same power law can be used to express the relation between anode surface temperature and discharge power. Anode surface temperatures rises with discharge power according to the following equation: $T = 300 + (33.2 \pm 5.8) \times P_d{}^{(0.46 \pm 0.03)}$, which fits the data with an R^2 value of 0.9988. This equation was used as a reference for the numerical investigation of the XPT in the previous chapter.

4.2.6 Visual observations

4.2.6.1 Plume focusing

The lower part of Fig. 4.22 shows plasma discharge from side view at two different applied anode potentials, while the upper part shows the front wall during thruster operation with a hollow cathode placed parallel to the anode. There were four distinct regions in the visible plasma discharge near anode because of the neutral injection scheme. In addition, a close look at the side view of the plasma discharge reveals that there is a dark space located between the anode and the bright plasma.

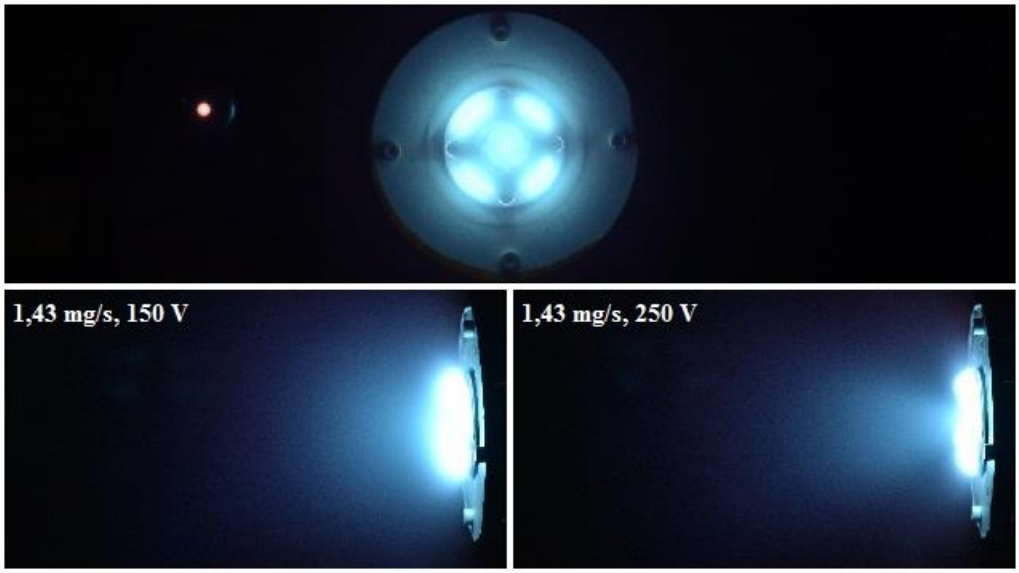

Figure 4.22 The XPT discharge front view (top) and side view (bottom) photos taken during experiments.

As the discharge voltage is increased from 150 V to 250 V, the plume loses its diffuse appearance, and a bright region called a "spike" on the thruster centerline starts to appear, which is observed at conventional Hall thrusters as well. Presence of the central spike[24], a larger concentration of ions in the plume, may be explained with neutrals flowing towards the centerline due to axis of symmetry and getting ionized through collisions with the electrons trapped on the thruster centerline.

4.2.6.2 Material deposition

Figure 4.23 shows that some material deposited on both the front wall and the anode. Dashed circle marks the region behind a ceramic bolt for color comparison. The deposited material was electrically conductive and the deposition on the front wall was much denser near the inner and outer edges of the anode.

The deposited material on the anode was analyzed by scanning electron microscopy (SEM) with energy dispersive X-ray spectroscopy. The contamination was found to contain aluminum, tungsten, carbon, iron, chrome, molybdenum and nickel. A double Langmuir probe, which has two electrodes made of tungsten, was inserted into the plasma to characterize electron flow properties. The deposited tungsten comes from the eroded probe tips. Aluminum and the rest of the deposited materials may originate from the beam damper and stainless steel vacuum chamber walls.

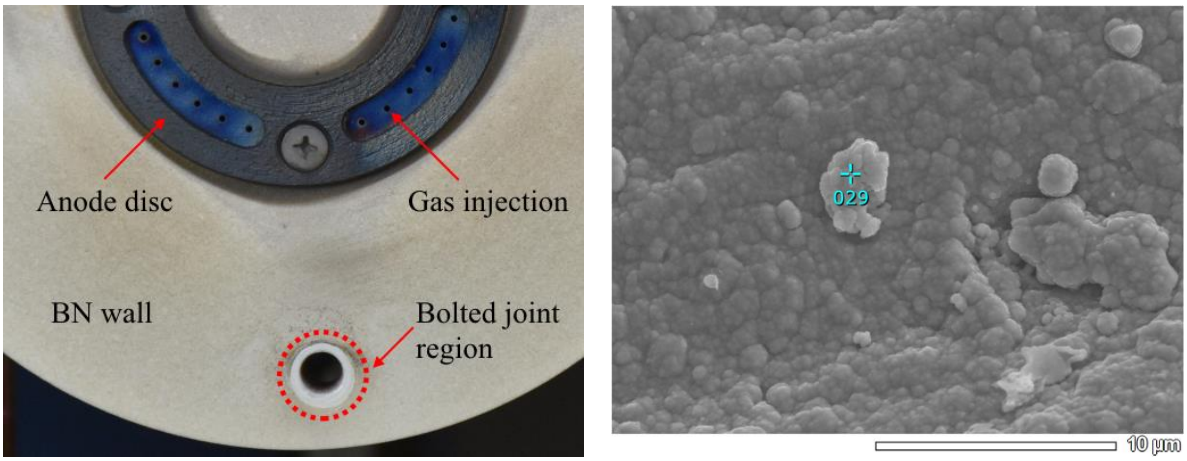

Figure 4.23 The front wall photo of the XPT (left) and a SEM image of the anode (right).

4.2.6.3 Anode dark space

Figure 4.24 (left) shows an intriguing phenomenon "anode dark space". The bright plasma was not formed inside the anode slots where neutral density and radial magnetic field strength are the highest. It was located downstream of the anode front surface by approximately 1-3 mm, depending on the location.

The fully kinetic code predicts that the number of excitation collisions takes place mostly inside the anode slots as shown in Fig. 4.24 (right). One possible explanation for this finding is that electron temperature inside the slots may be substantially lower than 8.7 eV, which is the minimum required electron temperature for electron-xenon excitation collisions.

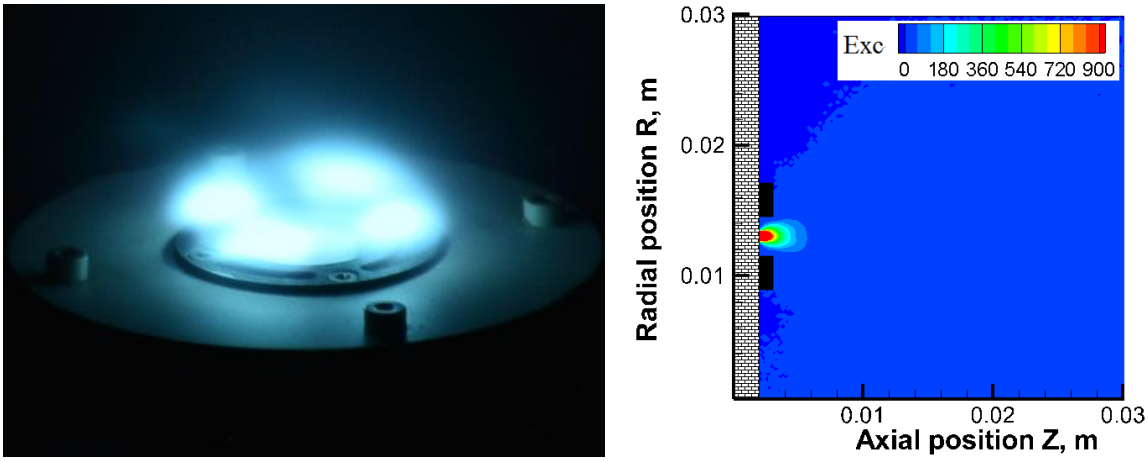

Figure 4.24 Anode dark space photo taken during experiments (left) and simulated excitation collisions (right) for the XPT.

4.3 Summary

We experimentally investigated the external discharge plasma thruster (XPT). Thrust performance was measured through a hanging pendulum thrust stand, and discharge current oscillations were characterized by a high frequency current probe. Thrust performance of the XPT was comparable to standard Hall thrusters at the same power level (~11 mN at 250W with 25% anode efficiency without any optimization), and discharge current had SPT-level stability ($\Delta<0.2$). A nude Faraday probe was used to measure ion current density profiles, and to gain insight into anode efficiency components. Ion beam profiles were Gaussian and symmetric with respect to the thruster centerline despite the azimuthally non-uniform plasma. Mass utilization efficiencies, beam utilization efficiencies, and plume divergence efficiencies varied from 28 to 62%, 78 to 99 %, and 40 to 48% respectively. Anode surface temperatures were measured by an infrared sensor, and it was discussed that excessive anode temperature may be responsible for the observed low mass utilization efficiencies. A double Langmuir probe was used to derive plasma properties in the azimuthal and axial directions. Electron temperatures as high as 15 eV and as low as 2.5 eV were observed at 10 mm axial distance from the anode, while electron densities ranged from 0.2 to $5x10^{18}$ m^{-3}. It was understood that even very small non-uniformity of the radial magnetic field strength in the azimuthal direction plays an important role in distributing plasma density.

References

[1] Nagao N., Yokota S., Komurasaki K., and Arakawa Y., "Development of a Two-dimensional Dual Pendulum Thrust Stand for Hall Thrusters," *Review of Scientific Instruments*, Vol. 7, 115108, 2007.

[2] Yamamoto, N., Komurasaki, K. and Arakawa, Y., "Discharge Current Oscillation in Hall Thrusters," *Journal of Propulsion and Power*, Vol. 21, No.5, 2005, pp. 870-876.

[3] Huang, W., Kamhawi, H., and Shastry, R. "Farfield Ion Current Density Measurements before and after the NASA HiVHAc EDU2 Vibration Test," *48th AIAA/ASME/SAE/ASEE Joint Propulsion Conference & Exhibit*, Atlanta, Georgia, 2012, AIAA 2012-4195.

[4] Brown, D. L., Walker, M. L. R., Szabo, J., Huang, W., and Foster, J. E., "Recommended Practice for Use of Faraday Probes in Electric Propulsion Testing," Journal of Propulsion and Power, Vol. 33, No. 3, 2017, pp. 582-613.

[5] Brown, D. L., Larson, C. W., Beal, B. E., and Gallimore, A. D., "Methodology and Historical Perspective of a Hall Thruster Efficiency Analysis," *Journal of Propulsion and Power*, Vol. 25, No. 6, 2009, pp. 1163-1177.

[6] Azziz, Y., "Experimental and Theoretical Characterization of a Hall Thruster Plume," PhD Thesis, Massachusetts Institute of Technology, Boston, 2007.

[7] Chung, P. M., Talbot, L., and Touryan, K. J., "Electric Probes in Stationary and Flowing Plasmas," Springer, New York, 1975.

[8] Hutchinson, I. H., "Principles of Plasma Diagnostics," Second Ed., Cambridge University Press, Cambridge, 2002.

[9] Dote, T., "A New Method for Determination of Plasma Electron Temperature in the Floating Double Probe," *Japan. J. Appl. Phys.* 7, (1968) 946-945.

[10] Oshio, Y., Ueno, K., and Funaki, I., "Plume Characterization of a Quasi-Steady Magnetoplasmadynamic Arcjet," *IEEE Transactions on Plasma Science*, Volume: 40, Issue: 12, 2012, pp. 3520 – 3527.

[11] Lobbia, R. B., and Beal, B. E., "Recommended Practice for Use of Langmuir Probes in Electric Propulsion Testing," *Journal of Propulsion and Power*, Vol. 33, No. 3, 2017, pp. 566-581.

[12] Mazouffre, S., Echegut, P., and Dudeck, A., "A calibrated infrared imaging study on the steady state thermal behaviour of hall effect thrusters," *Plasma Sources Science and Technology*, Vol. 16, No. 1, 2007, pp. 13-22.

[13] Spektor, R., Beiting, E. J., et al., "Infrared Thermographic Diagnostic for Imaging Hall Thrusters," *33rd International Electric Propulsion Conference*, Washington, 2013, IEPC-2013-452.

[14] S. Barral, N. Gascon, K. Makowski, Z. Peradzyński and M. Dudeck, Numerical study of the current-voltage characteristic of Hall thrusters, in Proc. 27th International Electric Propulsion Conference, Paper No. 2001-27, Pasadena, CA (USA), 2001.

[15] Jacobson, T. and Jankovsky, R., "Test Results of a 200W Class Hall Thruster," *34th*

AIAA Joint Propulsion Conference, Cleveland, OH, July, 1998, AIAA-98-3792.

[16] Polzin, K. A., Markusic, T. E., Stanojev, B. J., Dehoyos, A., Raitses, Y., Smirnov, A., and Fisch, N., J., "Performance of a Low-Power Cylindrical Hall Thruster," *Journal of Propulsion and Power*, Vol. 23, No. 4 (2007), pp. 886-888.

[17] Conversano, R. W., Goebel, D. M., Mikellides, I. G., Hofer, R. R., Matlock, T. S., and Wirz, R. E., "Magnetically Shielded Miniature Hall Thruster: Performance Assesstment and Status Update," *50th AIAA/ASME/SAE/ASEE Joint Propulsion Conference, Cleveland, OH, July 28-30, 2014.*

[18] Barral, S., and Ahedo, E., "Low-frequency model of breathing oscillations in Hall discharges," *Phys. Rev. E.*, 79, 046401 (2009).

[19] Boeuf J. P., and Garrigues L., "Low frequency oscillations in a stationary plasma thruster," *J. Appl. Phys.*, 84, 3541, 1998.

[20] Hara, K., Sekerak, M. J., Boyd, I. D., and Gallimore, A. D.,"Perturbation Analysis of Ionization Oscillations in Hall Effect Thrusters," *Physics of Plasmas*, Vol. 21, No. 12, 2014, Paper 122103.

[21] Sekerak, M. J., Plasma Oscillations and Operational Modes in Hall Effect Thrusters, Ph.D. thesis, University of Michigan, 2014.

[22] Hofer, R. R., and Gallimore, A. D., "Efficiency Analysis of a High-Specific Impulse Hall Thruster," *40th AIAA/ASME/SAE/ASEE Joint Propulsion Conference & Exhibit*, Ft. Lauderdale, Florida, 2004, AIAA-2004-3602.

[23] J. L. Ross, "Probe studies of a Hall thruster at low voltages," Ph.D. Dissertation, Michigan Technological University, Houghton, 2011.

[24] Bechu, S., Lasgorceix, P., Gascon, N., Roche, S., Prioul, M., Albarede, L., and Dudeck, M., "Comparison between two kinds of Hall thrusters - SPT100 and ATON," AIAA 2000-3524, *36th AIAA/ASME/SAE/ASEE Joint Propulsion Conference*, Huntsville, AL, July 2000.

[25] Sasoh, A., and Arakawa, Y., "A high-resolution thrust stand for ground tests of low-thrust space propulsion devices," *Rev. Sci. Instrum.* 64, 719 (1993).

[26] Xu, K., and Walker, M., "High-Power, null-type, inverted pendulum thrust stand," *Rev. Sci. Instrum.* Vol. 80, 2009.

[27] Koizumi, H., Komurasaki, K., and Arakawa, Y., "Development of thrust stand for low impulse measurement from microthrusters," *Rev. Sci. Instrum.* 75, 3185 (2004).

[28] Polk, J., Pancotti, A., Walker, M., Haag, T., Blakely, and John Ziemer, J., "Recommended Practices in Thrust Measurements," *33rd International Electric Propulsion Conference*, Washington, DC, 2013, IEPC-2013-440.

[29] Gessini, P., Gabriel, S. B., and Fearn, D. G., "Thrust Characterization of a T6 Hollow Cathode," *29th International Electric Propulsion Conference*, Princeton, 2005, IEPC-2005-257.

[30] Takahiro, S., Tsukizaki, R., Kuninaka, H., and Yamagaki, Y., "Development thrust measuring device using a CFRP as a measure of thermal drift," *Space Transportation Symposium FY2015*, Kanagawa, Japan, 2015, STEP -2015-0020.

[31] Cesare, S., et al., "Nanobalance: the European balance for micro-propulsion," *31st International Electric Propulsion Conference*, Ann Arbor, 2009, IEPC-2009-182.

Chapter 4 Appendix

A. 1 Electron density plots

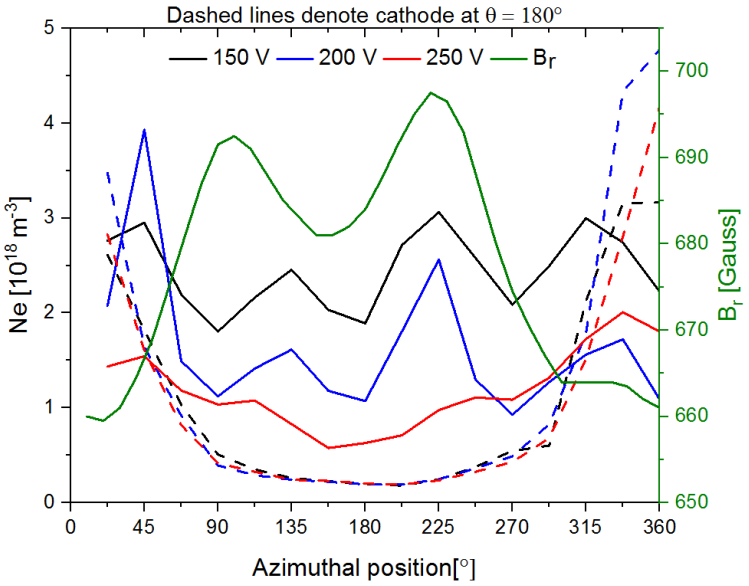

a) 1.43 mg/s mass flow rate

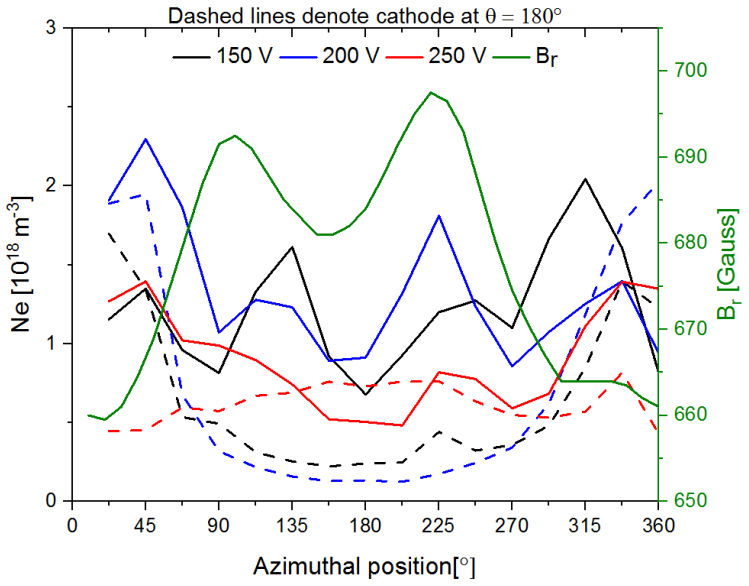

b) 0.95 mg/s mass flow rate

Figure 4.A.1.1 Azimuthal electron density distribution of the XPT along the anode centerline at z = 10 mm.

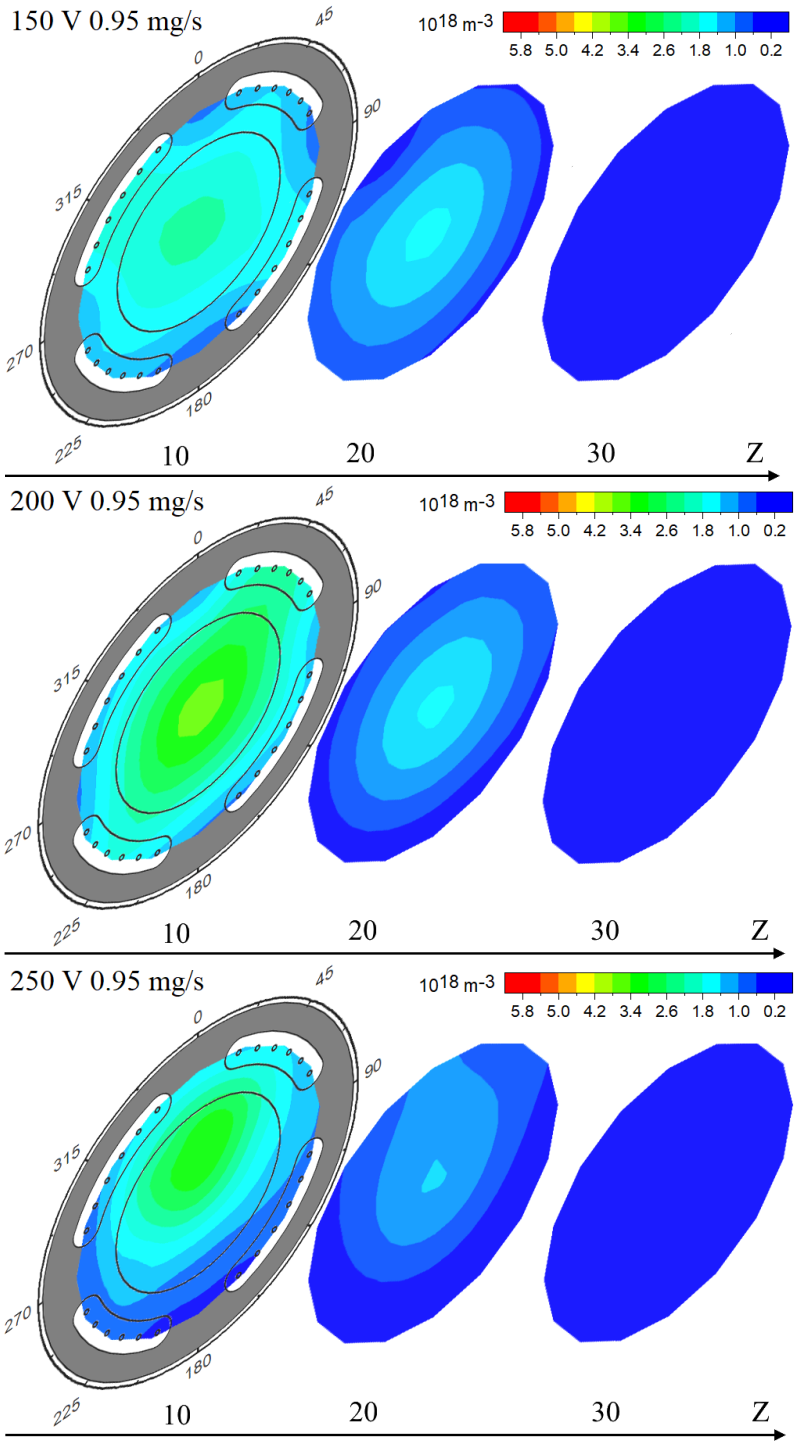

Figure 4.A.1.2 Electron density distributions of the XPT at different axial distances for cathode position of θ = 0°.

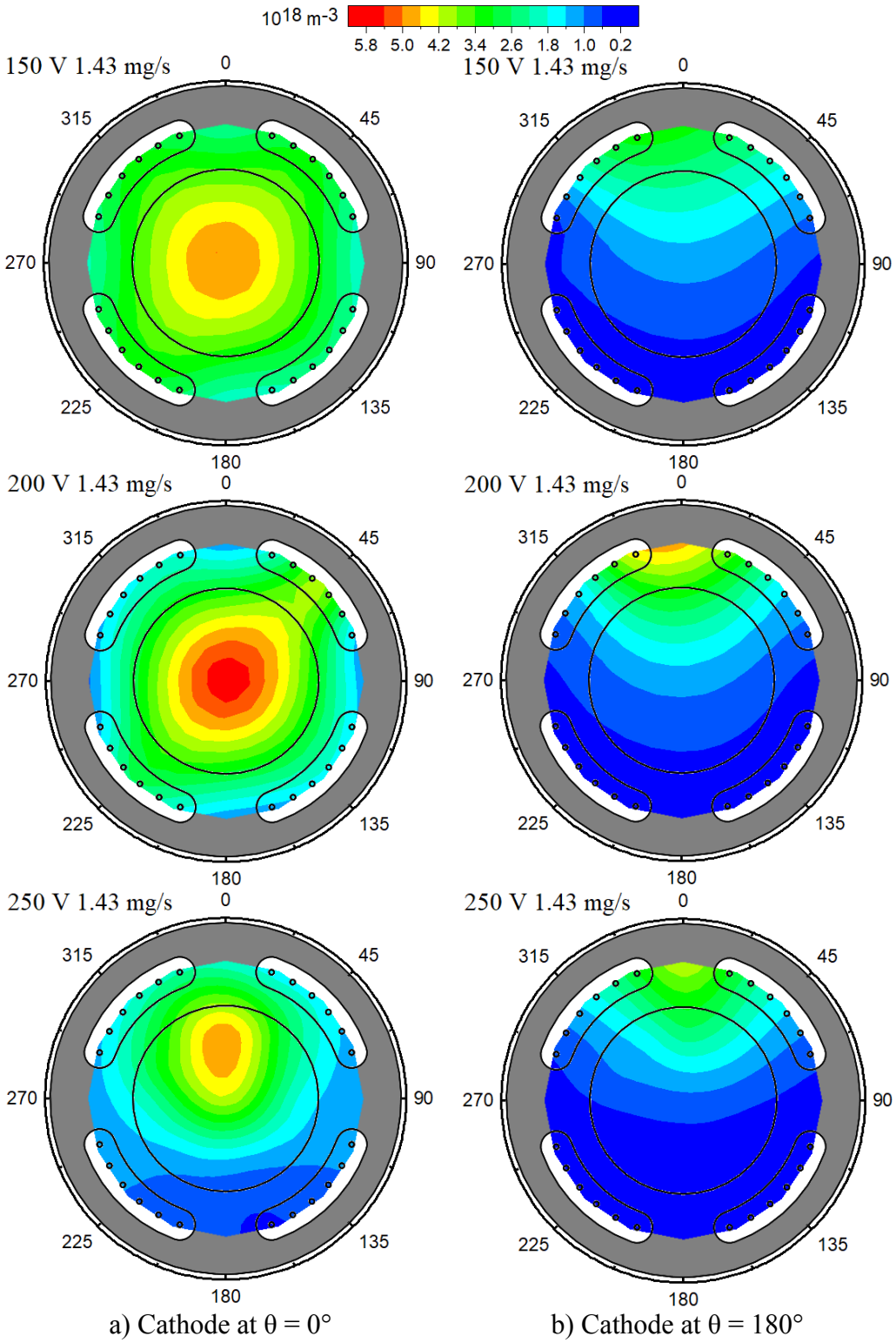

Figure 4.A.1.3 Electron density distributions of the XPT for 1.43 mg/s.

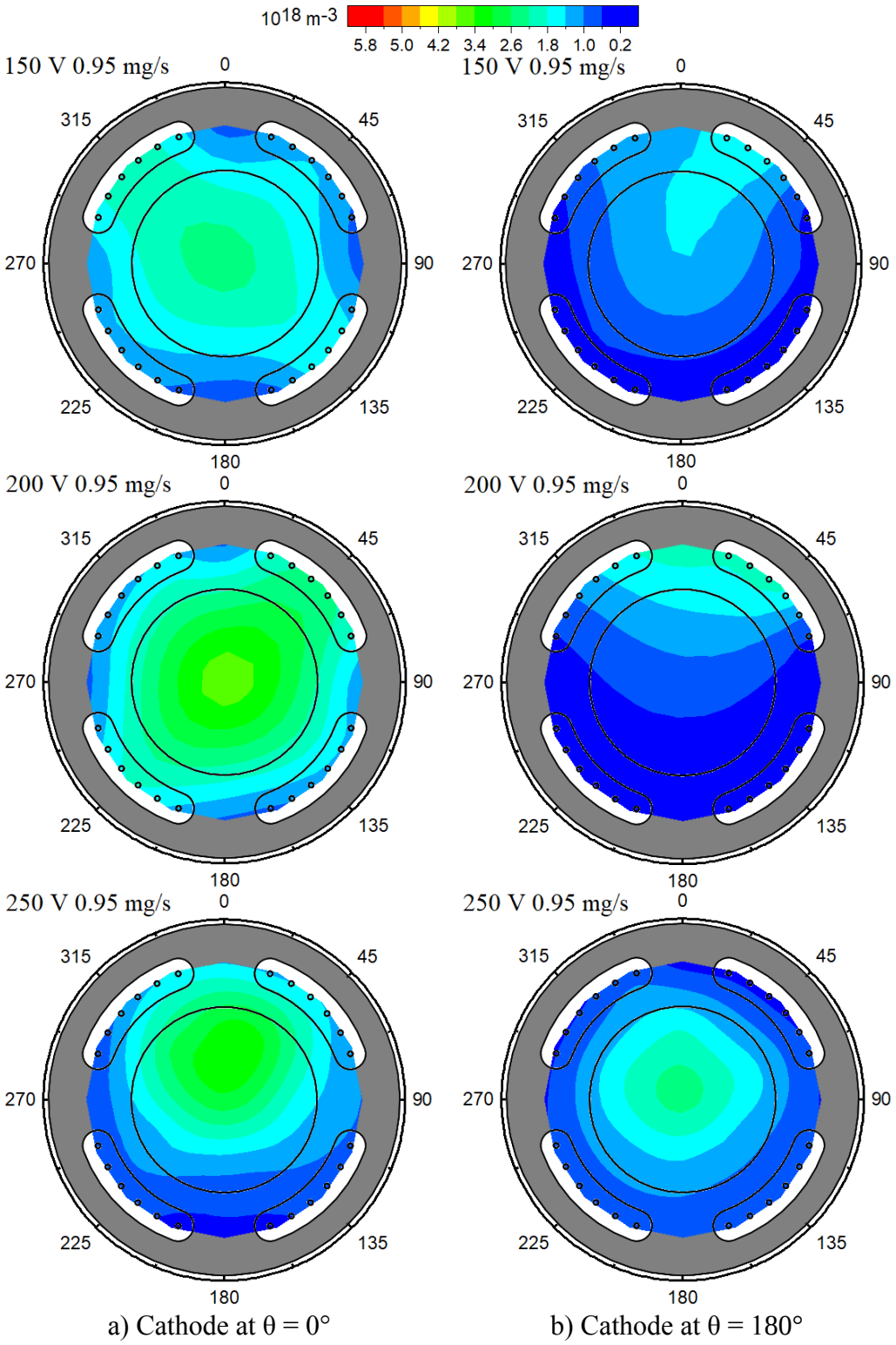

Figure 4.A.1.4 Electron density distributions of the XPT for 0.95 mg/s.

A. 2 Electron temperature plots

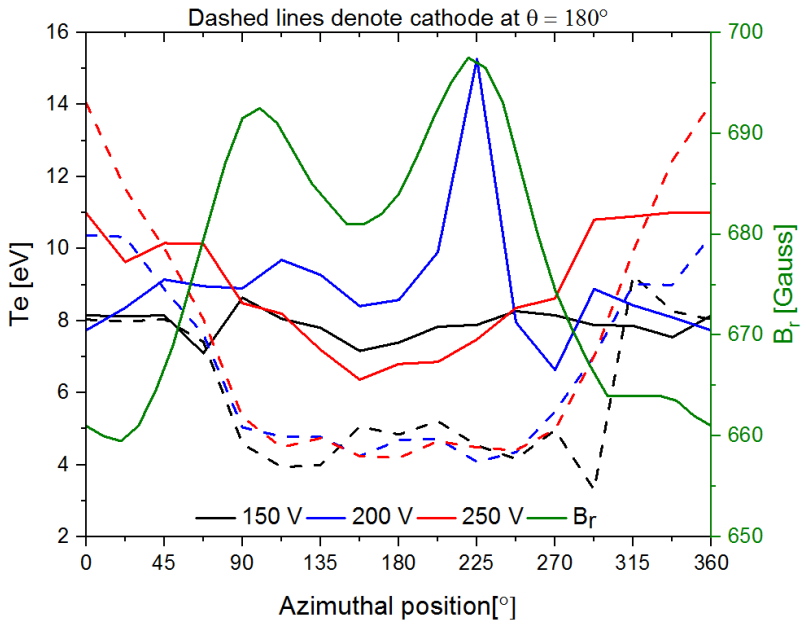

a) 1.43 mg/s mass flow rate

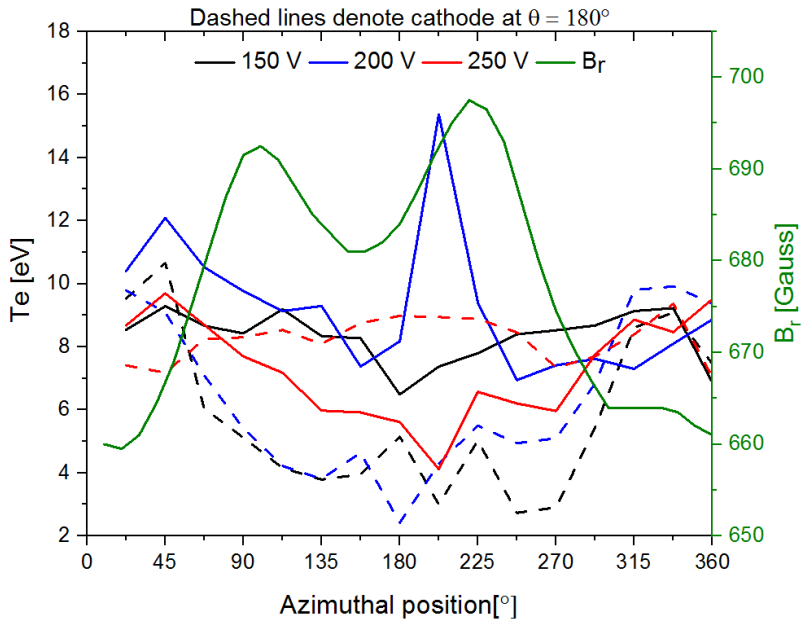

b) 0.95 mg/s mass flow rate

Figure 4.A.2.1 Azimuthal electron temperature distribution of the XPT along the anode centerline at z = 10 mm.

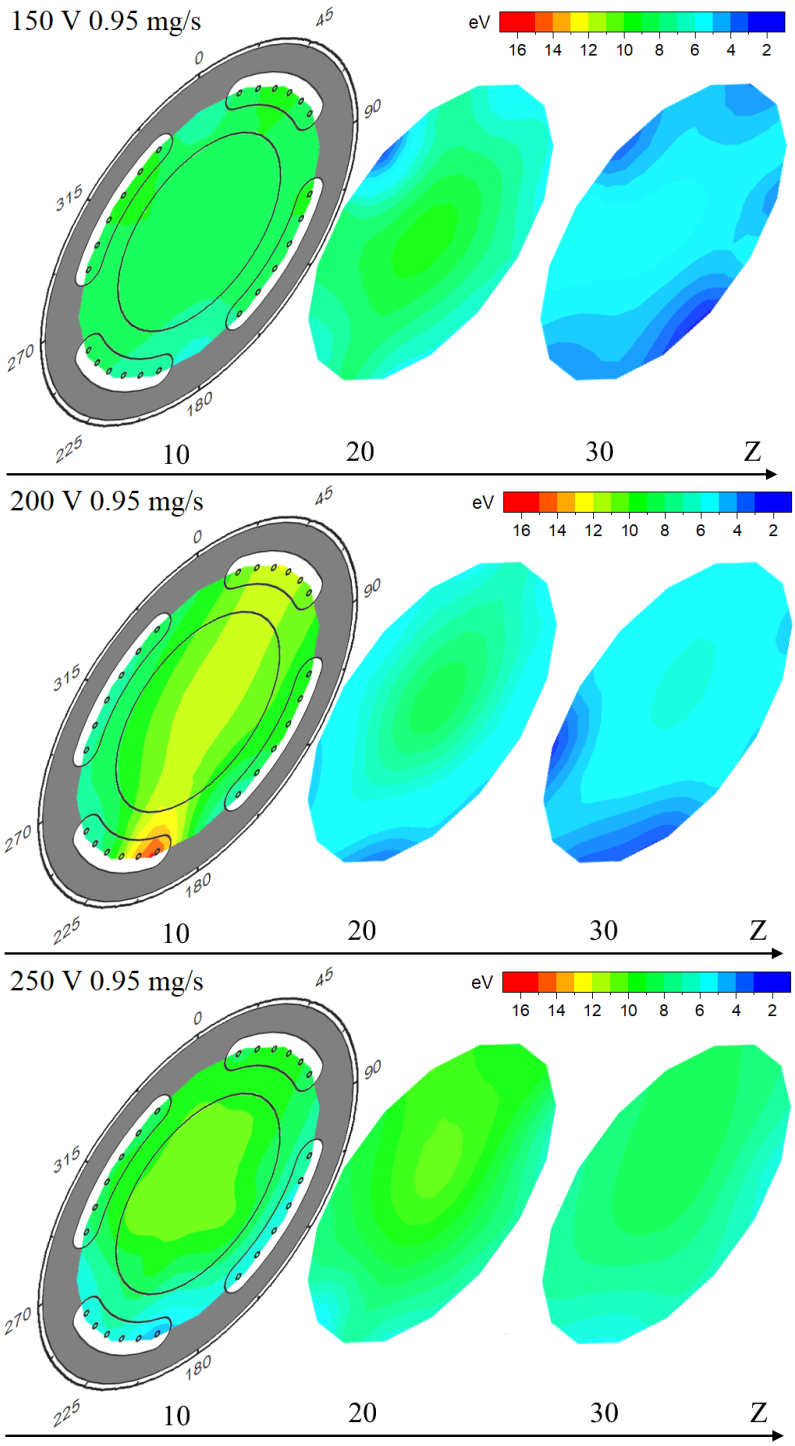

Figure 4.A.2.2 Electron temperature distributions of the XPT at different axial distances for cathode position of θ = 0°.

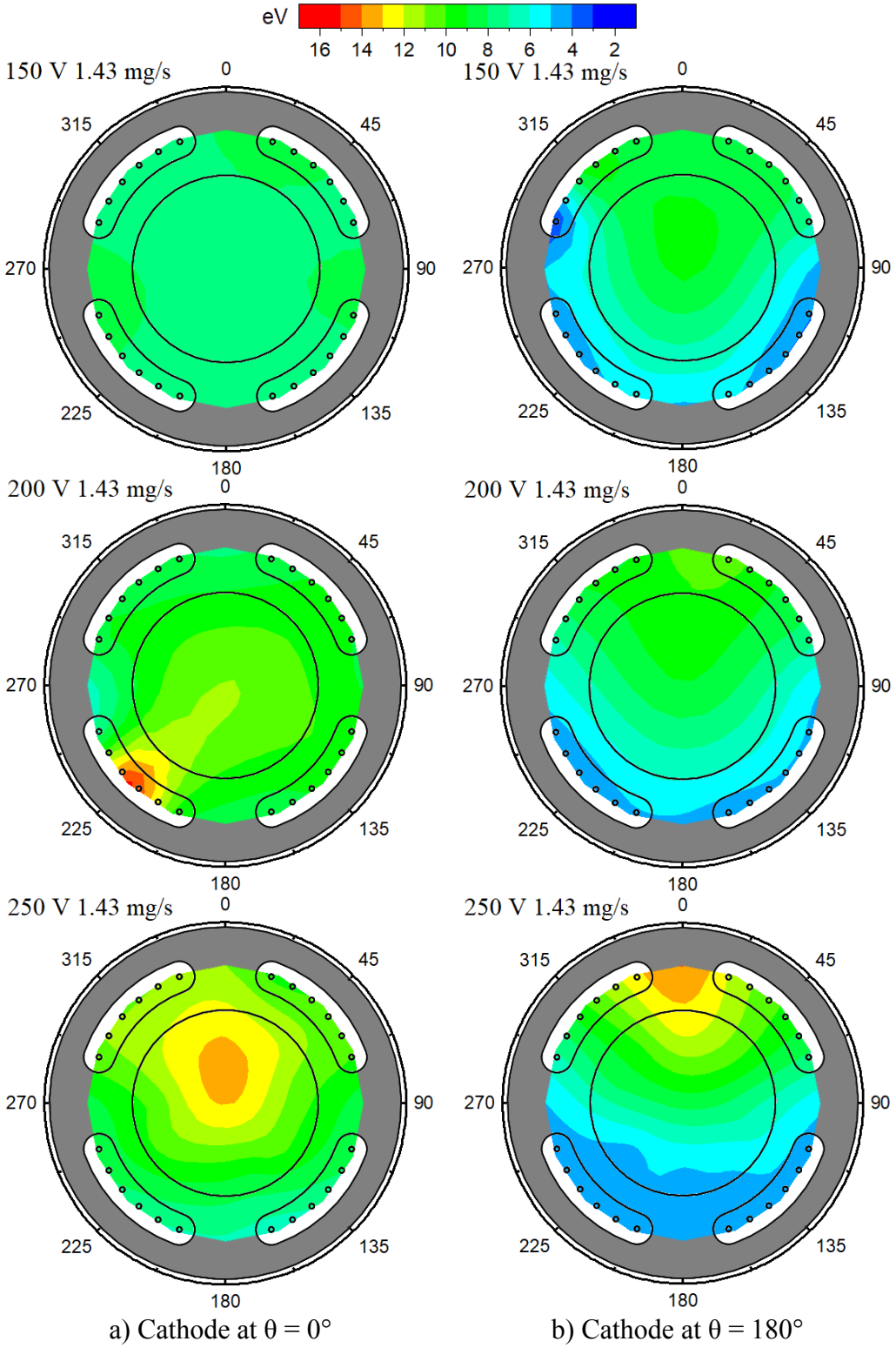

Figure 4.A.2.3 Electron temperature distributions of the XPT for 1.43 mg/s.

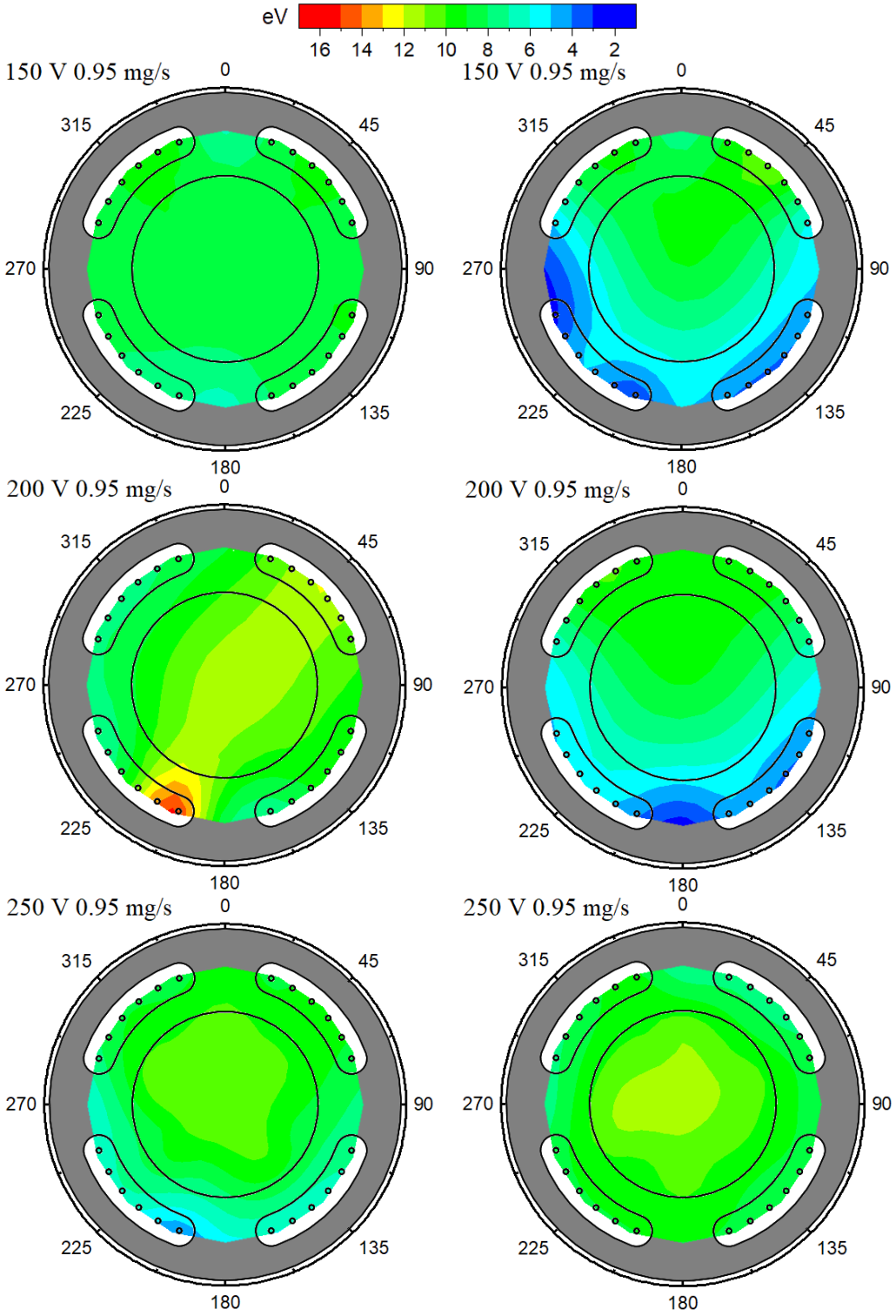

a) Cathode at θ = 0° b) Cathode at θ = 180°

Figure 4.A.2.4 Electron temperature distributions of the XPT for 0.95 mg/s.

A. 3 Precision Balance for Micro-Newton Resolution Direct Thrust Measurement

Accurate thrust performance characterization is critical, yet difficult for the development of electric thrusters because of low thrust levels. Common approaches to direct thrust measurement (hanging pendulum[25], inverted pendulum[26], and torsional balance[27]) are all based on measuring linear displacement of stand structures like vertical arm and horizontal beam. Hanging pendulum has great stability and a relatively simple structure but its sensitivity is a function of the pendulum arm. Inverted pendulum has a higher sensitivity compared to hanging pendulum but its stability is strongly dependent on stiffness of supporting flexures. Regarding torsional balance, it can achieve even higher sensitivity as its rotational axis is parallel to the gravity vector making it more appropriate for measuring low level thrust; however, thrust resolution depends on beam length limiting the vacuum chamber size. A detailed description of these thrust stands can be found elsewhere.[28] Thermal expansion of thrust stand structural parts, stiffness of supporting flexures and thruster mechanical connections (e.g., propellant feed tubes and electrical wires), and calibration method give rise to erroneous results in these conventional thrust stands. One possible way to limit the source of errors is to separate the thruster assembly from the displacement measuring apparatus as in target-based indirect thrust balances[29], in which thrust is estimated from cantilever beam target deflection due to plume impingement. Yet these balances are less accurate than the direct thrust balances due to uncertainties in the momentum transfer. Recently, a kind of hanging pendulum thrust stand incorporating a precision balance and a pulley-weight mechanism was studied for high power electric propulsion applications.[30] It was concluded that errors related to calibration process and thermal drift can be reduced.

In this chapter, we show that a precision balance can be used standalone for very accurate direct thrust measurement of Hall thrusters, and electric thrusters with continuous thrust in general. Precision balances have traditionally been preferred for calibration of the thrust stand actuators because weight of a Hall thruster with the mounting interface could well exceed the maximum load capacity. However, state-of-the-art precision balances can support heavy loads with satisfactory thrust resolutions (e.g., 1 mg resolution up to 5 kg). In this method, thruster is put directly on a precision balance pan, and operated with its thrust axis is parallel to the gravity, and vertical to the balance pan and vacuum chamber ground. Radiation from thin copper sheets on thruster mounting interface and a thick ceramic plate above balance pan helps keeping the pan temperature low. There are not any moving secondary structural parts or damping mechanisms eliminating major error sources related to thermal drift, stiffness, and friction. Thrusters with different thrust-to-weight ratio do not require special adjustments to the thrust stand. What is more, a precision balance in general has built-in internal calibration weights enabling manual or automatic self-calibration.

Internal calibration is more accurate compared to external calibration providing reliable results.

In advanced thrust balances like the Nanobalance[31], the error sources can be quantified through sophisticated techniques. However, these balances are able to resolve micro-Newton thrust levels only for very low power applications such as FEEP or cold gas thrusters because thermal effects are significant for low-to-high power thrusters making micro-newton resolution very difficult to realize. Besides, careful attention must be exercised in stand setup, calibration, operation, and post-processing of the raw thrust data making overall process time-consuming and laborious. The drawbacks of the current methods can be overcome by measuring thrust on a precision balance, thus the principal advantage is in terms of error reduction. Another important advantage is that precision balance is easy to use, calibrate, and setup. For example, it does not require any post-processing shortening the overall experiment duration significantly. Therefore, we believe this method will aid electric propulsion researchers seeking for high thrust resolution, and small electric propulsion labs that do not have access to complicated and expensive thrust stands. Nevertheless, vertical operation of the thruster can pose limitation to horizontal vacuum chamber size, and an active cooling system would be necessary for high power operating conditions or long duration thruster operations.

A. 3.1 Experimental setup

The Hall thruster used in this study was a configuration of the external discharge plasma thruster (XPT). Performance of Hall thrusters are usually measured using variation of hanging pendulum stands, and reported thrust measurement uncertainties are around %5 corresponding to 1 mN for a 20mN-class thruster. A 1-mN discrepancy can be acceptable from engineering point of view but it is a significant figure from the standpoint of plasma physics. Measuring thrust on a precision balance provides a striking improvement in the thrust accuracy enabling measurements with a micro-Newton level uncertainty, which can hardly be done by the conventional methods. Figure 4.A.3.1-2 shows the experimental setup, and the electrical diagram.

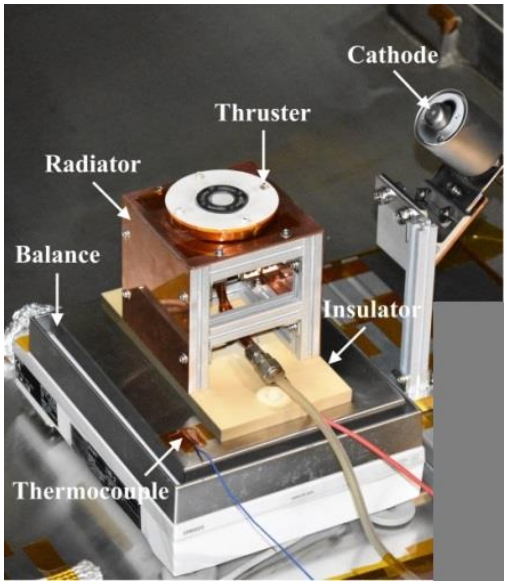

Figure 4.A.3.1 Precision balance experimental setup.

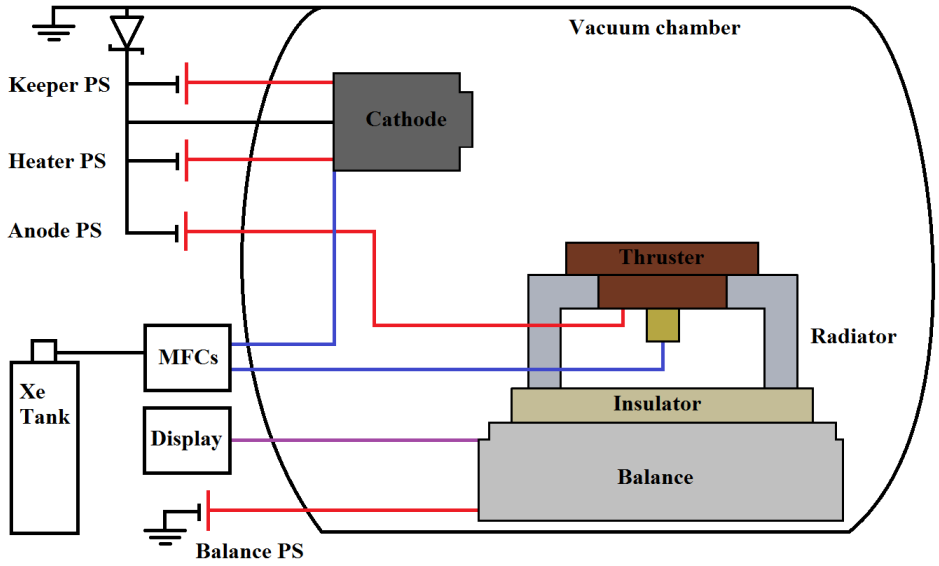

Figure 4.A.3.2 Electrical diagram of the experimental setup.

A. 3.2 Precision balance

A Mettler Toledo XP6002S precision balance, which was kindly provided by Mettler-Toledo K.K., was used. It has a readability of 10 mg corresponding to a display resolution of about 0.1 mN. The balance was placed on a large flat metal plate, and leveled with built-in level sensor. It was self-calibrated manually with internal weights before each measurement to compensate for temperature drift. Thrust data were read from the balance display, and also sampled at a rate of 10 samples per second using RS232C interface. Unlike the hanging pendulum case, the cathode was separated from the thruster interface due to thermal considerations. The balance pan temperature was taken using a thermocouple to ensure that it will not surpass the maximum allowed temperature of 40°C. The balance pan temperature stayed below 30°C although no any active cooler was employed. Table 4.A.3.1 summarizes the features of the balance.

Table 4.A.3.1 Precision balance specifications.

Maximum capacity	6.1 kg
Readability	10 mg
Repeatability	30 mg
Linearity	±20 mg
Temperature drift	0.0003 %/°C
Adjustment	Internal

Figure 4.A.3.3 Precision balance offset check.

A.3.3 Uncertainty analysis of the precision balance measurement

There are several sources for possible errors:

1) Thermal drift,

2) Vibrational noises from the vacuum chamber,

3) Electrical noises due to plasma, and

4) Magnetic field disturbance due to the magnetic field generated by the thruster magnetic circuit, or current-carrying anode wire.

Thermal drift coefficient (0.0003 %/°C) due to the pan temperature rise is trivial between 15-30 °*C*. The balance display did not show any reaction to vibrations from the vacuum chamber or to electrical noise emitted by the plasma. Besides, the thruster was turned off and on multiple times to check the zero and weight reading offsets. No difference was found between the consecutive measurements as shown in Fig. 4.A.3.3. Regarding the magnetic field disturbance, the magnetic force exerted on the balance pan by the thruster is zero because of the large gap between the thruster and the magnetic circuit (>10 cm). The magnetic force of the anode wire at a distance of >1 cm (ceramic plate thickness) should also be insignificant owing to low discharge current (<1 A) and low magnetic permeability of the balance pan made of stainless steel. Hence, measurements should represent the true thrust value with an uncertainty corresponding to the balance display resolution (also called readability).

A.3.4 Results

Figure 4.A.3.4 compares the results from the precision balance and the hanging pendulum thrust stand. It was found that the precision balance results compare very well with the hanging pendulum. Thrust data from the precision balance fall within the standard error of the hanging pendulum. It should be noted that any thrust contribution from the cathode was absent because the cathode was not included to the measurement in case of the precision balance. What is more, measured the discharge current between the hanging pendulum and the precision balance operations were varied 1-3% and 4-6% respectively for 0.95 mg/s and for 0.48 mg/s mass flow conditions. Although its percentage is small it also contributes to the discrepancy as the discharge current and thrust is related.

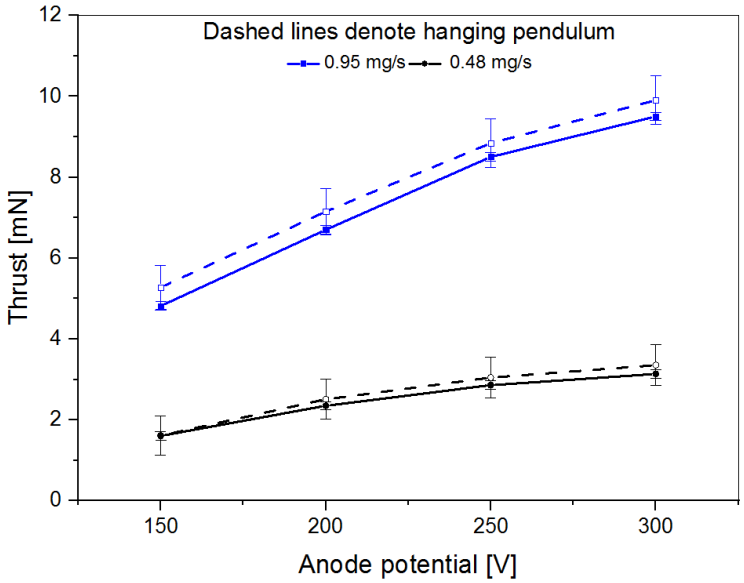

Figure 4.A.3.4 Comparison of the measured thrusts. *Error bars correspond to total measurement error.*

CHAPTER 5

Discussion

Contents

"No matter what you look at, if you look at it closely enough, you are involved in the entire universe."

Micheal Faraday

5.1 Propellant Utilization Analysis

In the classical approaches, an annular discharge channel (e.g., SPT and TAL) or a cylindrical discharge channel (e.g., end-Hall/CHT) provides long enough neutral particle residence time ensuring that ionization collisions will occur. The XPT lacks any kind of discharge channel letting propellant gas to expand into vacuum right after leaving the anode exit. Therefore, it has been argued that such a "cavity-less plasma thruster" would have very low ion beam current, propellant utilization efficiency, and plume divergence since neutral particles are not constrained in radial direction by a cavity or sidewalls, and they are free to diffuse to the vacuum in both axial and radial directions. The presented results demonstrate that a physical ionization chamber (a non-anodic cavity) is not prerequisite for efficient electron impact ionization of propellant gas. The successful operation of the thruster can be explained by the following propellant utilization analysis.

Propellant utilization efficiency (η_m) is equal to ionization probability of a neutral atom or molecule traversing a plasma region of a characteristic length L_c if ion loss to the front wall is insignificant.[1]

$$\eta_m = 1 - \exp\left(\frac{L_c}{\lambda_i}\right) \tag{5.1}$$

where λ_i is ionization mean free path, which is a function of neutral velocity (v_n), electron density (n_e), and ionization reaction rate ($< \sigma_i v_e >$) as follows $\lambda_i = v_n / (n_e < \sigma_i v_e >)$. The characteristic length, also called ionization length, depends on the length of large magnetic field region, and it can be approximated as the discharge channel height ($L_c \approx h$) in a conventional Hall thruster.[2] In the case of the XPT, the length of high neutral density region is much shorter than of large magnetic field region since the neutral density decreases exponentially with increasing axial distance. The characteristic length can be determined from the neutral density gradient ($n_n dz/dn_n$) at the center of the anode front surface where ionization is assumed to start. It was estimated to be 2.2 mm using the neutral density distribution plot shown in Fig. 2.7.

The XPT has two distinctive features that make contact measurements extremely problematic. First, when the probe tip inserted into the near the anode front surface, it interrupts Hall current flow, and severely disturb discharge current or arcs with the anode. Second, anisotropy of the electron energy distribution function (EEDF) can be expected to be large due to the strong radial magnetic field strength, and curvature of the field lines. Nevertheless, ionization mean free paths (λ_i) can still be estimated by assuming an average electron temperature and electron density (n_e) near the anode front surface (z < 2 mm). The assumption will be valid provided that the propellant utilization efficiencies to be calculated from Eq. (5.1) will match those estimated from the measured thrust using Eq. (4.6). The average electron temperature was assumed to be 15 eV at 250 V anode potential and constant for all the mass flow rate conditions by taking the results of the Langmuir probe measurements into account (see Fig. 4.17). Then the curve-fitted ionization reaction rate ($< \sigma_i v_e >$) is equal to $7.1\text{x}10^{-14} m^3/s$ from Ref. 3. The neutral velocity is a function of the anode temperature, and the front wall temperature due to rapid thermal accommodation of neutrals at the anode and the front wall as follows:$v_n = \sqrt{8k_B T_{anode}/m\pi}$). The neutral velocities were calculated for each mass flow rate at 250 V operating condition according to results of the infrared sensor measurements, which revealed that the anode surface temperature rises with discharge power according to the following equation: $T = 300 + (33.2 \pm 5.8) \times P_d^{(0.46 \pm 0.03)}$ fitting the data with an R^2 value of 0.9988.

As a result, the electron densities are found to be approximately $2.3\text{x}10^{18}\ m^{-3}$, $1.7\text{x}10^{18}\ m^{-3}$ and $0.8\text{x}10^{18}\ m^{-3}$ in average for 1.43 mg/s, 0.95 mg/s and 0.48 mg/s mass flow rates respectively at 250 V anode potential. The actual electron densities near the anode surface are expected to be higher than these values because the estimated value of 2.2 mm represents an upper bound to the characteristic length (L_c), which will become

shorter once the ionization collisions start to deplete the neutrals. The corresponding ionization mean free paths were 2.3 mm, 2.9 mm and 5.6 mm increasing with decreasing mass flow rate. For the same reason, the actual ionization mean free paths should be shorter than these values.

Electron density inside the discharge channel of a SPT[4] ($n_e \approx 1x10^{18}\ m^{-3}$) is substantially lower than of the XPT and the ionization length ($L_c \approx 5 - 10$ mm) is longer. This explains why the XPT is as efficient as a SPT even without a physical ionization chamber. Measurement of the plasma properties near the anode surface is reserved for future work.

5.2 Ionization and Acceleration Regions

The propellant utilization analysis suggested that the thruster strongly confines electrons, and provides high neutral density near the anode surface, which, as a result, starts cascade ionization in a narrow region ($L_c \approx 2$ mm). However, a similar agreement to the agreement of the propellant utilization efficiencies estimated from Eq. (4.6) and (5.1) could be obtained if ionization length and electron density near the anode surface were assumed to be longer and lower respectively. Also, it can be argued that ionization length should be long as the peak magnetic field does not appear inside the anode slots or in front of the anode. 2D distribution of ionization collision events simulated by the fully kinetic code shown in Fig. 5.1 supports our assumption that ionizations collisions occurs in a narrow region.

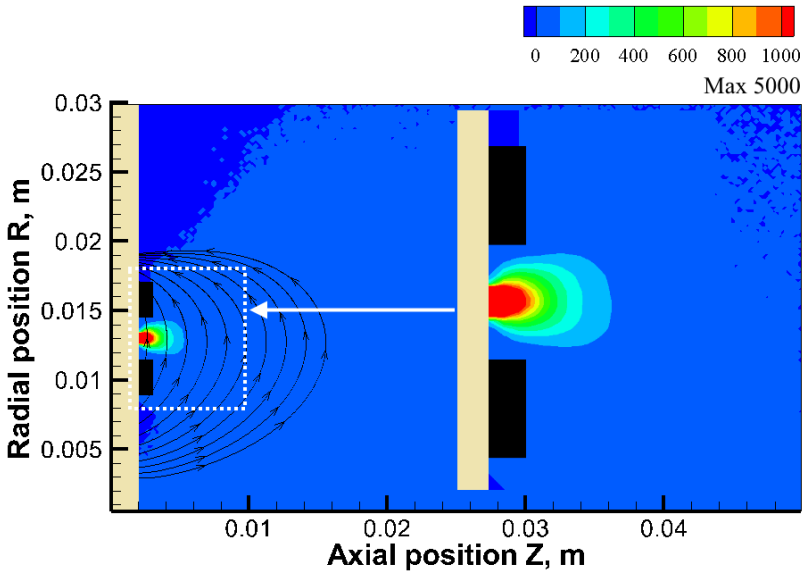

Figure 5.1 Simulated 2D distribution of ionization collision events for the XPT.

Figure 5.2 shows number of ionization collisions and plasma potential profile at the anode centerline. As seen in the figure, most of the ionization collisions (about 90 %) occur in a region of 2 mm long where the neutral density and the radial magnetic field are the highest. Sputtering of the annular anode walls is not expected to be a concern because ions formed inside the anode slot see very little axial acceleration.

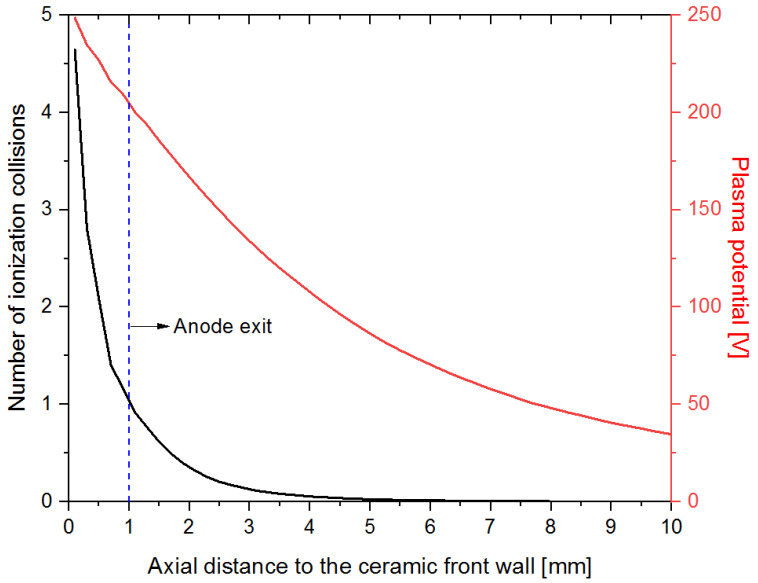

Figure 5.2 Simulated number of ionization collisions/plasma potential profile at the anode centerline for the XPT.

Figure 5.3 shows the simulated axial electric field distribution of the XPT for 250 V-0.95 mg/s. Acceleration region seems to be located further downstream compared to the ionization region extending up to 5-10 mm in the axial direction. Nevertheless, ions are accelerated immediately after their creation, so the characteristic length of the acceleration region should be similar to the ionization region length, which is ~ 2 mm. The electric field vector, shown by the arrow lines, point out the acceleration direction of the ions. The thrust loss due to the beam divergence seems to be lower for those ions generated inside the anode slots. In fact, this is expected because the radial magnetic field provides a more uniform structure there. The red regions, which shaped like a divergent nozzle, show the largest axial electric field in Fig. 5.3. Ion number densities inside these regions are a few orders of magnitude lower than the maximum ion number density. As for the electron number density, it is a few orders of magnitude larger than the ion number density implying that the quasi-neutrality does not hold any more. This finding reinforces the magnetic mirror confinement of electrons discussion given in Chapter 2.

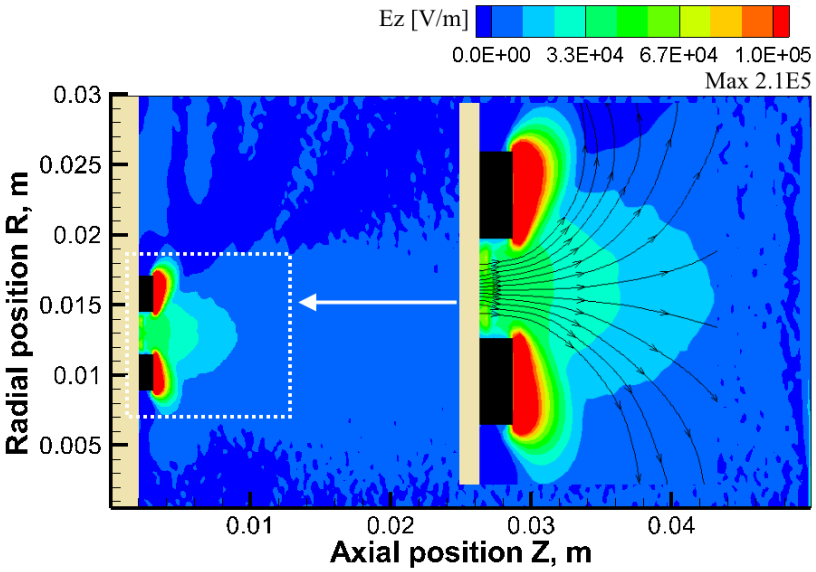

Figure 5.3 Simulated axial electric field distribution of the XPT for 250 V - 0.95 mg/s.
Lines with arrows represent the electric field vector.

5.3 Discharge Current Stability

The stability criterion[5] for a one-dimensional fully ionized flux in a SPT with respect to linear perturbations can be satisfied only if:

$$\frac{\partial}{\partial z}\left(\frac{B_0}{n_0}\right) > 0 \tag{5.1}$$

where B_0 is magnetic field , n_0 is neutral number density and z is the axial distance. The neutral number density in a SPT is approximately constant across the ionization region, so the Eq. (5.1) takes the form of $\partial B_0/\partial z > 0$, which implies that a decrease in the magnetic field toward the discharge channel exit, leads to the instability.

The radial magnetic field profile of the XPT has a negative-only gradient ($\partial B_0/\partial z < 0$). Thus, one can argue that the discharge of the XPT should be unstable. Nonetheless, Eq. (5.1) states that the stability criterion can also be satisfied if the neutral number density decreases faster than the radial magnetic field strength. Fig. 5.4 plots the calculated $\partial(B_0/n_0)/\partial z$ for the 250 V - 0.95 mg/s operating condition. The partial derivative has a positive value at z = 0 mm increasing sharply to reach its peak value at z = 3 mm, and then it starts to decline and finally becomes negative after z = 6 mm.

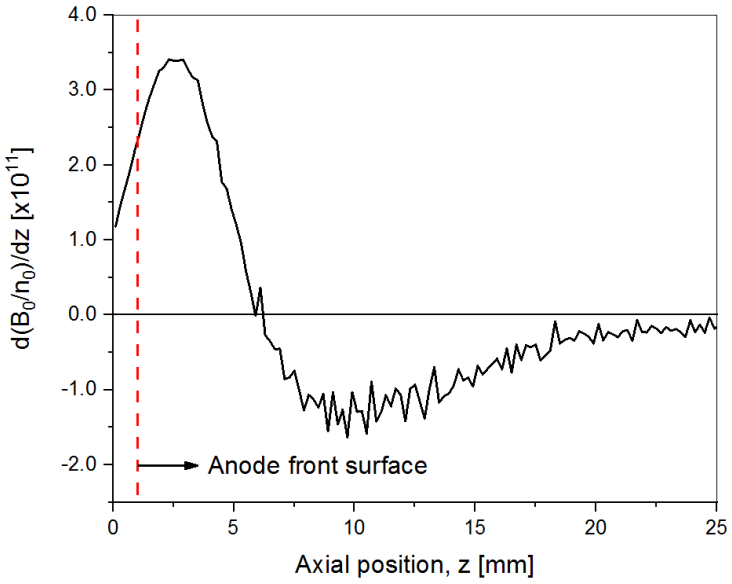

Figure 5.4 $\partial(B_0/n_0)/\partial z$ for the XPT calculated at 250 V - 0.95 mg/s.

The neutral number density in the XPT decreases sharply as the neutral atoms expand into a vacuum instead of a fixed volume chamber, so the stability criterion is fulfilled. An important conclusion to be drawn from equation Eq. (5.1) is that any improvement in the mass utilization efficiency should enhance the stability of discharge as well. This conclusion is in good agreement with the experimental results. The mass utilization efficiencies (see Table 4.3) increases, whereas the oscillation amplitudes (see Fig. 4.13) decreases for 0.95 mg/s and 1.43 mg/s cases when the discharge voltage altered from 150 V to 250 V.

5.4 Front Wall Material Deposition

Magnetic shielding has been proven to reduce discharge channel wall erosion, but it has also yielded to increased pole piece erosion, which may pose a risk for deep space missions. The current understanding as to the reason of the pole piece erosion observed in magnetically shielded Hall thruster that it may be due to acceleration of low energy ions born very close the pole piece surfaces by local electric fields.[6] The same argument may also apply to standard or wall-less Hall thruster configurations.

The conductive material deposition observed on both the front wall and the anode shown in Fig. 4.23 prove obviously that deposition rate is higher than the erosion rate. This can be explained by strictly reduced plasma loss at magnetic cusps due to large magnetic fields (0.15-0.25 Tesla). The loss probability for an electron or ion at the cusp area on the front wall can be expressed as an exponential function of the ratio between total cusp area (A_c) and hybrid Larmor radius ($r_h = \sqrt{r_e r_i}$) as follows: $p = \exp(-A_c/{r_h}^2)$.[7] If we assume an average electron temperature of 15 eV, and an average ion energy of 250 eV for an operating condition at 250 V anode potential, then the loss probability distribution for varying values of the cusp magnetic field strength can be plotted as shown in Fig. 5.5. The loss probability p goes to zero as the magnetic field strength B goes to 0.1 Tesla.

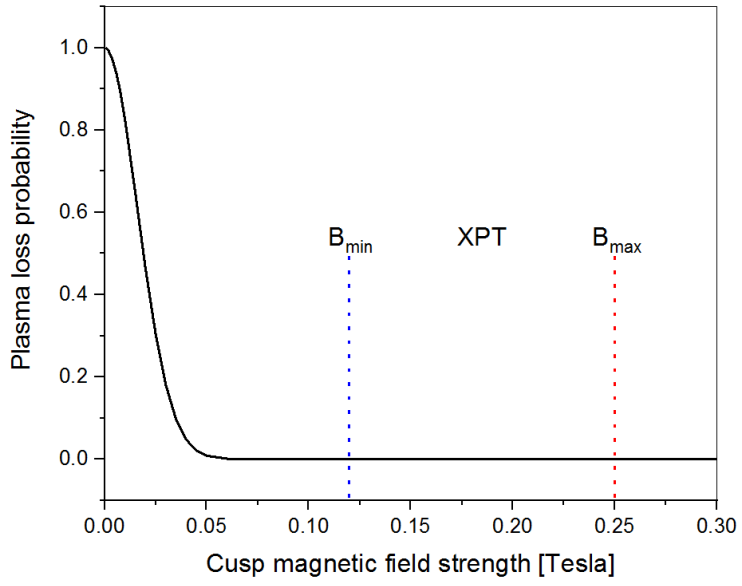

Figure 5.5 Estimated plasma loss probabilities against cusp magnetic field strength for the XPT. *B_{min}, B_{max} shows minimum and maximum magnetic field strength on the front wall surface.*

In addition, local electric fields or electrostatic attraction on the low energy ions due to the accumulated charge on the front wall may be small to cause any significant sputtering because the front wall located behind ionization, and acceleration regions. The distance (d_w) that the low energy ions must move from the edge of an expanding plasma plume to the front wall starts from 1 mm (thickness of the anode), and approaches infinity, while it starts out at about zero for the other Hall thrusters. Figure 5.6 shows a schematic of expanding plasma plume (left) and a side view of a thruster firing (right).

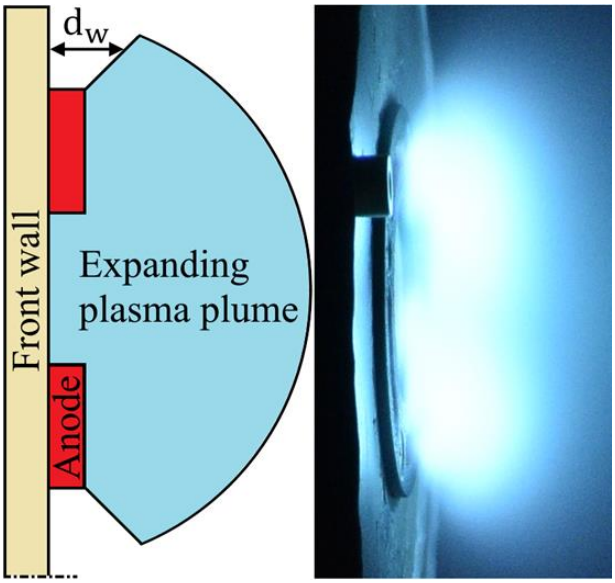

Figure 5.6 A schematic of expanding plasma plume of the XPT (left) and a side view photo of a thruster firing taken during experiments (right). *d_w shows the distance between the front wall and the edge of the expanding plasma plume.*

5.5 Background Pressure Effect

Xenon gas was injected into the vacuum chamber using an additional flow line located about 4 m away from the thruster assembly to elevate the background pressure. The background pressure increases the discharge current as seen in Fig. 5.7. Discharge currents at perfect vacuum were estimated to be 8%, 11% and 12% lower than the measured ones at the lowest achievable pressures for 0.48 mg/s, 0.95 mg/s and 1.43 mg/s respectively. Ionization region can be assumed to be a cylinder of radius r, and height h, where the radius and the height of the cylinder correspond to outer radius of the anode disc, and the ionization layer thickness equal to ~2 mm from our analysis in subsection A. Xenon mass flow rate ingestion into the ionization region as a result of the random flux of background gas atoms is then predicted to be maximum 0.8% of the anode mass flow rates according to the thermal model ($mn_bA_{exit}v_{th}/4$, where $A_{exit} = \pi r^2 + 2\pi rh$) from Ref. 8. The ingested background neutrals seem to make only trivial contribution to the propellant utilization efficiency. Yet, their effect on the discharge current is notable. This may be a result of complex interactions such as shift in the ionization zone since the observed discrepancy is too large to be accounted for only by the background gas entrainment.[9]

Thrust should also be measured at different background pressures to evaluate in-space performance of the thruster. The back pressure effect is still an open question for Hall thrusters, and should be investigated for the XPT also in the future.

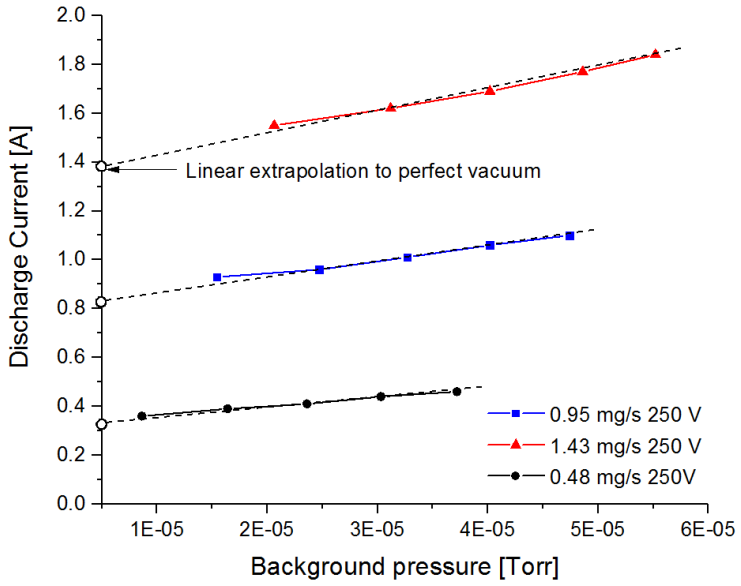

Figure 5.7 Experiment of background pressure effect for the XPT. *Background pressure was increased by injecting xenon through an additional flow line.*

5.6 Comparison of Simulation and Experimental results

One should bear in mind that the fully kinetic code computes plasma properties for axisymmetric geometries, whereas the anode cavity of the XPT is not symmetric about the z-axis. So neutral and plasma densities are not uniform along the azimuthal direction. Thus, seeking a qualitative agreement might be more suitable rather than making a direct quantitative comparison with the experimental results. Table 5.1 lists calculated and measured thrust performances, and Fig. 5.8 compares plasma properties calculated and measured at the anode centerline.

Table 5.1 Calculated and measured thrust performances for the XPT.

	0.95 mg/s, 250 V Xenon		1.43 mg/s, 250 V Xenon	
	Simulation	**Experiment**	**Simulation**	**Experiment**
F[mN]*	8.7	10.7	16.5	17.4
I_d[A]	0.48	0.99	0.93	1.64
Δ	0.33	0.04	0.17	0.03
η_t[%]**	33.6	24.0	40.3	25.6

* Thrust measurement uncertainty is ± 0.7 mN for 0.95 mg/s case and ± 1 mN for 1.43 mg/s case,

** Uncertainty of experimental thrust efficiency is ± %3.3 for 0.95 mg/s case and ± %2.7 for 1.43 mg/s case.

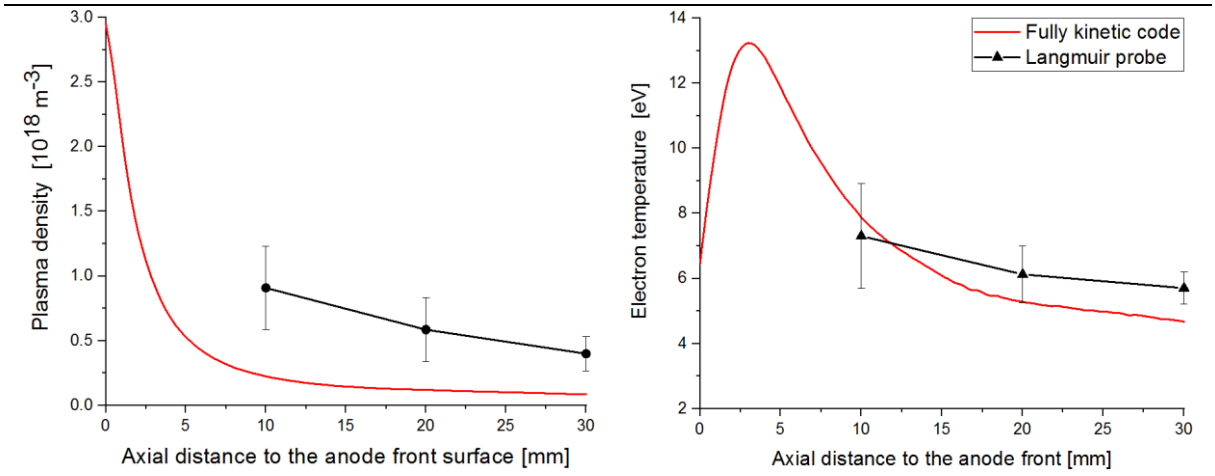

Figure 5.8 Simulated (nominal case) and measured plasma properties of the XPT for 250 V – 0.95 mg/s at the anode centerline. *Plasma densities measured at the azimuthal direction were averaged to compare to the simulation results. Error bars shows the standard deviation.*

Plasma density and electron temperature increases with decreasing axial distance to the anode surface, and discharge current oscillation amplitude decreases when the mass flow rate increased from 0.95 mg/s to 1.43 mg/s. The simulation successfully captures these trends, and satisfactorily reproduces the measured thrust, electron density, and electron temperature considering the fact that uncertainty is large especially in electron density measurement. Nonetheless, the measured discharge current is significantly underestimated. This can be explained by the fact that azimuthal oscillations cannot be captured by the fully kinetic code due to its r-z simulation geometry. It is known that both azimuthal and non-azimuthal oscillations contribute to the anomalous electron transport in Hall thrusters.[10-12] Tang et al.[13] simulated a cylindrical anode layer Hall thruster and concluded that the rotating spokes get stronger for higher magnetic fields. It can thus be suggested that azimuthal oscillations such as rotating spokes may have important role on the anomalous electron mobility in the XPT considering its very high radial magnetic field. Besides, propellant injection scheme, the non-homogeneous radial magnetic field, poorly assumed background pressure or anode temperature may be other possible causes for the discrepancy. Azimuthally nonuniform propellant flow can increase discharge current as much as 1.8 times.[14] Background pressure near the thruster head in the vacuum chamber may be higher than assumed maximum background pressure of 5×10^{-5} Torr. The non-homogeneous radial magnetic field can give rise to non-uniform electron distribution along the azimuthal $E \times B$ direction increasing the axial electron drift.

References

[1] Kim, V., "Main Physical Features and Processes Determining the Performance of Stationary Plasma Thrusters," *Journal of Propulsion and Power*, Vol. 14, No. 5, 1998, pp. 736–743.

[2] Shagayda, A. A., "On Scaling of Hall Effect Thrusters," *33th International Electric Propulsion Conference*, The George Washington University, Washington, D.C., 2013, IEPC-2013-056.

[3] Goebel D. M., and Katz, I., *Fundamentals of Electric Propulsion: Ion and Hall Thrusters* (Wiley, New York, 2008), p.476.

[4] Boeuf, J-P., "Tutorial: Physics and modeling of Hall thrusters," J. Appl. Phys. 121 011101.

[5] Morozov, A. I., and Savelyev, V. V., "Fundamentals of Stationary Plasma Thruster Theory," *Reviews of Plasma Physics*, Vol. 21, 2000, pp. 203-391.

[6] Jorns, A. J., Dodson, C., Anderson, J., Goebel, D. M., Hofer, R. R., Sekerak, M. J., Lopez-Ortega, A., and Mikellides, I. G., "*52nd AIAA/SAE/ASEE Joint Propulsion Conference*, Salt Lake City, Utah, 2016, AIAA 2016-4839.

[7] Sengupta, A.,"Magnetic confinement in a ring-cusp ion thruster discharge plasma," J. Appl. Phys., 105(2009), 093303.

[8] Randolph, T., Kim, V., Kaufman, H. R., Kozubsky, K., Zhurin, V. V., and Day, M., "Facility Effects on Stationary Plasma Thruster Testing," *23rd International Electric Propulsion Conference*, Fairview Park, OH, IEPC-1993-093.

[9] Walker, M. L. R., "Effects of Facility Backpressure on the Performance and Plume of a Hall Thruster," Ph.D.
Dissertation, Aerospace Engineering, University of Michigan, Ann Arbor, MI, 2005.

[10] Hirakawa, M. "Electron Transport Mechanism in a Hall Thruster," *25th International electric Propulsion Conference*, Cleveland, 1997, IEPC-97-021.

[11] Adam, J. C., Heron, A., and Laval, G., "Study of stationary plasma thrusters using two-dimensional fully kinetic simulations," *Phys. Plasmas*, 11, 295 (2004).

[12] Choueiri, E. Y., "Plasma oscillations in Hall thrusters," Phys. Plasmas, 8, 1411 (2001).

[13] Tang, D. L., Geng, S. F., Qiu, X. M., and Chu, P. K., "Three-dimensional numerical investigation of electron transport with rotating spoke in a cylindrical anode layer Hall plasma accelerator," Phys. Plasmas, 19, 073519 (2012).

[14] Yasuhiro F., Yokota S., Komurasaki, K., and Arakawa, Y., "Oscillation Reduction of an Anode-Layer-Type Hall Thruster by Azimuthal Propellant Nonuniformity," 44th AIAA/ASME/SAE/ASEE Joint Propulsion Conference & Exhibit, Hartford, Connecticut, 2008, AIAA 2008-5187.

CHAPTER 6

Conclusion and Recommendations for Future Work

"As you start to walk on the way, the way appears."

Jalaluddin Rumi

6.1 Conclusion

i) The external discharge plasma thruster (XPT), a prototype of alternative low power Hall thruster, which produces and sustains a plasma discharge completely outside of a non-anodic cavity, was proposed in order to address efficient scaling down and lifetime problems of low power Hall thrusters. The XPT produces, and sustains a plasma discharge completely in the open space outside of the thruster structure through a magnetic mirror configuration. It eliminates the very fundamental component of Hall thrusters, discharge channel side walls, and its magnetic circuit consists solely of a pair of hollow cylindrical permanent magnets. The XPT is the first Hall thruster that operates without any annular or cylindrical discharge channel walls. The volume to surface area ratio of the discharge channel goes to infinity. Therefore, it is expected to operate particularly in very low power regime where conventional Hall thrusters cannot prevent high ion/electron losses to the channel walls. Design details and key physics of this novel Hall thruster were described, and action items for improving thrust performance are presented.

Experiment results showed that the XPT has similar discharge characteristics with SPT. The thrust and the anode specific impulse ranged from 1.6 to 17.9 mN, and from 352 to 1276 sec respectively at anode potentials of 150-200-250 V with anode mass flow rates of 0.48-0.95-1.43 mg/s. The anode efficiency ranged from 6.7 to 26.8 % at discharge powers from 43 to 418 W. Performance of the XPT is comparable to SPT at the same power level. Significantly, stable operation ($\Delta<0.2$) was possible over wide range of operational conditions. The XPT does not possess an annular discharge channel or a cylindrical one and the propellant gas is allowed to expand into vacuum right after leaving anode. It might be considered that such a "cavity-less plasma thruster" would have very low plume divergence efficiency and mass utilization efficiency since neutral particles migrate away from the anode surface in all directions when sidewalls are absent. Therefore, farfield ion current density measurements were taken to find out plume divergence through sweeping a nude

Faraday probe in the radial direction at fixed axial distances. Ion current density profiles revealed that ion beams are collimated and plumes have Gaussian distributions. The charged-weighted divergence angles were essentially similar to those of typical Hall thrusters and varied from 34 to 51 degrees. Mass utilization efficiencies ranged from 28 to 62%.

The XPT has four slots on the anode to inject neutrals and this non-uniform injection scheme leads to bright and dark regions in the plume. The bright regions are formed along the anode slots and the light intensity is stronger at the slot center. Thus, one can expect that plasma density in the dark regions where there are flat head screws will be significantly lower than of the bright regions due to higher neutral density. To examine this phenomenon, the near field plume of the XPT was mapped using double Langmuir probe method. Plasma density and electron temperature were measured in the radial, axial and azimuthal directions at anode potentials of 150, 200, and 250 V and mass flow rates of 0.95 and 1.43 mg/s. Plasma densities and electron temperatures were found to reach $6x10^{18}$ m^{-3} and 15 eV respectively. These values are substantially higher than conventional Hall thrusters, which explain why our thruster is as efficient as conventional ones even without a physical ionization chamber. The 2D maps of ion number density revealed an interesting result that the darks regions can have as much plasma density as the bright regions. The effect of the cathode position was also examined, and it was understood that plasma density, and Br profile are correlated, and that even very small non-uniformity of the radial magnetic field strength in the azimuthal direction has significant influence on plasma density distribution Overall results question the necessity of discharge channel walls or guard rings, and provide a successful proof of concept experiment of the XPT. Proof-of-concept study was completed, but further study is required to enhance thrust performance of the XPT.

ii) A fully kinetic particle code was used to investigate the importance of uncertainties associated to physical parameters through a sensitivity analysis. A 500W-class laboratory model magnetic-layer Hall thruster was used as the testbed. The sensitivities of the physical parameters, including thermal accommodation coefficient, anode/wall temperature, Bohm diffusion coefficient, electron injection current, cathode coupling voltage, and background pressure, were quantified one-by-one on a conservative possible range. The results suggest the wall erosion prediction is more sensitive to the physical parameters than the thrust or the discharge current. Among the physical parameters, sensitivity to the Bohm diffusion coefficient and parameters related to the neutral flow (i.e., thermal accommodation coefficient and anode/wall temperatures) were dominant. It was hence found that uncertainties in the physical parameters related to the neutral flow had comparable influence on the Bohm diffusion coefficient despite the low attention they attracted.

iii) The XPT was simulated by the fully kinetic particle code, and the sensitivity analysis methodology was applied to determine upper and lower bounds for estimated thrust performance. A satisfactory agreement was found between the experimental and simulated performance parameters. Numerical results suggested that the XPT can be as much efficient as conventional Hall thrusters of the same power range. 2D distribution of ionization collision events simulated by the fully kinetic code supported our propellant utilization analysis that most of the ionization collisions occur in a region of 2 mm long where the neutral density and the radial magnetic field are the highest. The thruster provides high neutral density near the anode surface, and its magnetic field strongly confines electrons, which results in cascade ionization in a narrow region.

iv) A highly simplified plasma device was successfully developed. The XPT can be used a standard test bed for benchmarking accuracy of various plasma codes. It is very suitable for optical emission spectroscopy as plasma discharge between the anode and the cathode is fully observable. It is now possible to design new experiments that will improve our understanding on interaction between plasma and magnetic field.

6.2 Recommendations for Future Work

Experiment results point out that sputtering of thruster parts may not be a lifetime limiting factor for an electric thruster having fully external discharge, and that it can achieve similar thrust performance compared to conventional, cylindrical, and magnetically shielded Hall thrusters at the same power levels. Nevertheless, the design of the XPT needs to be improved to match with the performance of high power hall thrusters. The following items are recommended for further work:

a. Material deposition observed on both the anode and the front wall implies that long lifetime may be possible, but the back-sputtering deposition rate on thruster surfaces due to erosion of the vacuum chamber walls should be quantified. A lifetime test is also required to provide conclusive evidence.

b. Excessive anode temperature may be responsible for the moderate mass utilization efficiency as it decreases residence time of neutrals, and enable them to escape without getting ionized. This can be attributed to small anode thickness (1mm) of the XPT, and poor thermal conductivity due to ceramic front wall. Anode temperature can be decreased by modifying the anode design (e.g. extending its rear surface inside the thruster body to increase the thickness), and heat conduction path.

c. The current magnetic circuit design of the XPT provides poor radial magnetic field homogeneity. A better plume divergence efficiency can be achieved by optimizing the magnetic field topography.

d. Width of slots on the anode is related to the neutral velocity, and density in front of the anode. Therefore, anode thickness and slot width/number should be considered important geometrical design parameters in addition to the magnetic circuit geometry.

e. Electron density plots given in Fig. 4.16 and Appendix 4.A.1 suggest that plasma flow adjust itself such that it will be uniform in the azimuthal direction as the axial distance increases even though the propellant injection scheme is highly non-uniform. Therefore, a non-uniform neutral injection scheme, by increasing the local neutral density, may be a key approach to be able to successfully operate Hall thrusters at ultra-low mass flow rates for the applications of precise attitude control, which requires micro-Newton level thrust. Nonetheless, a uniform propellant injection scheme would favorable at relatively high mass flow rates because it is known that the azimuthal non-uniformity or heterogeneity of propellant flow rate considerably influences electron conductivity.[1, 2]

External discharge approach opens up a plethora of new applications. For instance, a very thin (< 10 mm) lightweight low power Hall thruster can be designed for cube/nano/micro satellite applications. Efficient operation with light fuels such as air might be possible because electron temperatures are expected to be high in the ionization regions. Therefore, another application can be atmosphere-breathing electric propulsion in very low Earth orbits (100-250 km) for drag-free flight. What is more, applying the magnetic shielding method to nested-channel Hall thrusters would require a very bulky thruster head with numerous coils to feed. Therefore, external discharge approach may be more suitable for very high power applications (> 50 kW, e.g., cargo missions to Mars) as it can reduce the thruster head mass up to one order of magnitude, and also pole piece erosion does not seem to be a concern unlike what occurs in SPTs with magnetic shielding.

References

[1] Yasuhiro F., Yokota S., Komurasaki, K., and Arakawa, Y., “Oscillation Reduction of an Anode-Layer-Type Hall Thruster by Azimuthal Propellant Nonuniformity,” 44th AIAA/ASME/SAE/ASEE Joint Propulsion Conference & Exhibit, Hartford, Connecticut, 2008, AIAA 2008-5187.

[2] Baranov, V., Nazarenko, Y., and Petrosov, V.," Azimuthal Non-uniformities in Accelerators with Closed Electron Drift," 27th International Propulsion Conference, Pasadena, California, IEPC-01-18.

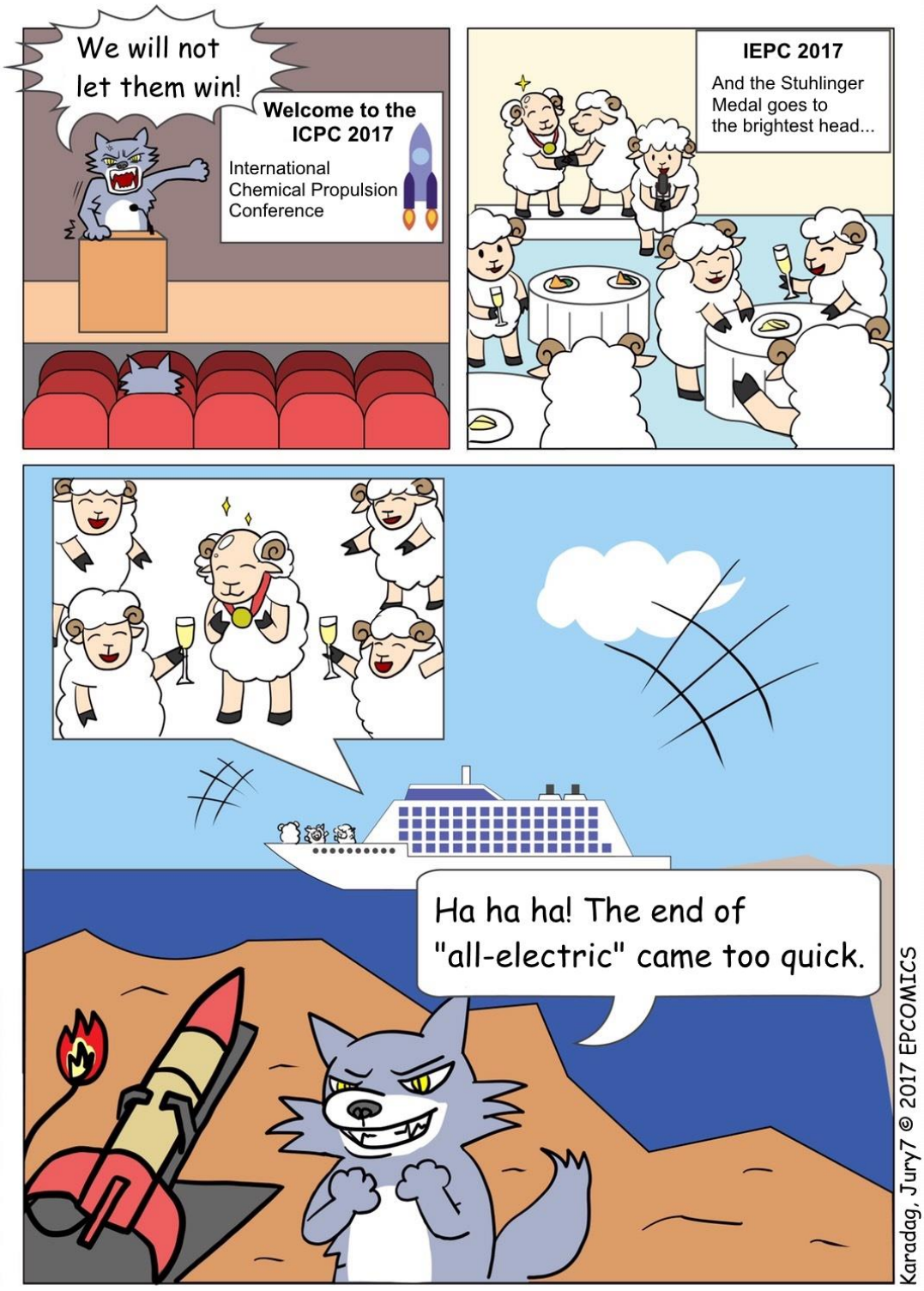
We will not let them win!
Welcome to the ICPC 2017
International Chemical Propulsion Conference
IEPC 2017
And the Stuhlinger Medal goes to the brightest head...
Ha ha ha! The end of "all-electric" came too quick.
Karadag, Jury7 © 2017 EPCOMICS